UNIVERSITY OF COPENHAGEN
FACULTY OF SCIENCE

Center for Quantum Devices
Niels Bohr Institute

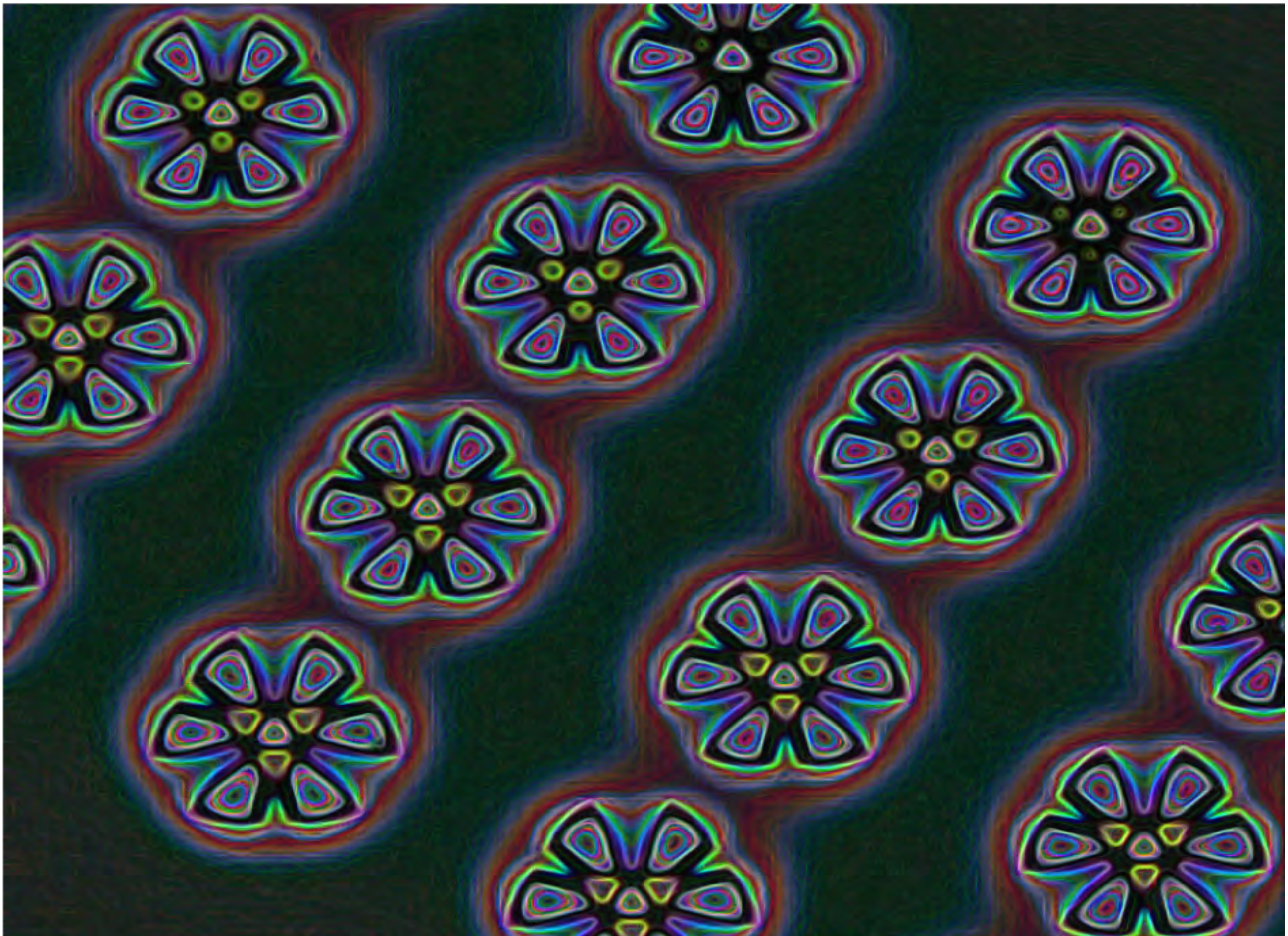

PhD thesis

Martin Bjergfelt

In-situ patterned superconductor/semiconductor nanowires for quantum devices

Supervisor: Professor Jesper Nygård

Co-supervisors: Associate Professor Thomas Sand Jespersen & Elisabetta Maria Fiordaliso

This thesis has been submitted to the PhD School of The Faculty of Science, University of Copenhagen on December 20, 2019

Abstract

The quality of interfaces and surfaces is crucial for the performance of nanoscale devices. A pertinent example is the close tie between current progress in gate-tunable and topological superconductivity using superconductor/semiconductor electronic devices and the hard proximity-induced superconducting gap obtained from epitaxial aluminium/indium arsenide heterostructures. Fabrication of devices requires selectively etching superconductor segments from the semiconductor; this is currently only possible with Al/InAs, curbing the functional use of other superconductor/semiconductor material combinations. This thesis presents a new crystal growth platform based on three-dimensional structuring of growth substrates which is independent of the choice of semiconductor and superconductor, and enables the synthesis of semiconductor nanowires with *in-situ* patterned superconductor shells. This wafer-scale technique enables realisation of all the most frequently used architectures in superconducting hybrid devices. Characterisation using electron transport at cryogenic temperatures revealed an increased device yield, electrostatic stability, along with evidence of ballistic superconductivity compared to etch-processed devices. In addition to aluminium, indium arsenide nanowires with patterned indium, vanadium, tantalum and niobium shells are presented.

Structural characterisation of the hybrid nanowires by transmission electron microscopy was used to correlate the crystallinity of the superconductor shells to the superconducting transport properties. A range of crystallinity was observed, from epitaxial crystals in aluminium and indium to amorphous or nanocrystalline films of vanadium, tantalum and niobium. The occurrence of these morphologies can be understood through consideration of the relationship between nucleation probability, surface energies and interfacial strain. Using a wide range of materials increases understanding of superconducting properties of materials at the nanoscale, as well as the conditions for obtaining hard-gap proximity-induced superconductivity in hybrid devices. Overall, this thesis shows that long-range epitaxy between a superconductor and a semiconductor is not a prerequisite for proximity-inducing a hard superconducting gap in all superconductors. Impurity-free, uniform interfaces may be sufficient if the thin film itself supports well-defined superconductivity. The presented platform opens for future work on advanced device architectures, new combinations of hybrid nanomaterials and *in-situ* protection of surfaces.

Cover image: “Bloom”

False-coloured optical microscope image of top-down processed shadow masks etched into an InAs substrate for nanowire growth and *in-situ* patterning of superconductor segments on the nanowire in full-shell geometries. Spin-coated electron beam resist polymer covers the surface non-uniformly and the light is reflected in different colours from the etched structures and polymer thickness gradients.

Dansk resumé

Ydeevnen i nanoelektroniske devices afhænger i høj grad af nanomaterialernes renhed og kvalitet i aktive grænseflader. Et relevant eksempel findes i hybride heterostrukturer bestående af halvledere og superledere, hvor epitaksi mellem superledende aluminium og halvledende indium arsenid nanotråde har muliggjort fremtræden progression i udviklingen af elektrostatisk kontrollérbar topologisk kvanteelektronik. Denne hybrids success består i udtrakt grad i evnen til at inducere et hårdt, tilstandsfrit, superledende energigap i halvlederen, en vigtig forudsætning for studier af topologiske kvantetilstande. Fabrikation af devices til denne type nanoelektronik kræver imidlertidigt at superlederen selektivt kan fjernes, eksempelvis ved kemisk ætsning, hvilket indtil videre kun er muligt i Al/InAs hybrider. Denne begrænsning hindrer udforskningen af andre, potentielt bedre, materialekombinationer. Med denne afhandling præsenterer jeg en ny dyrkningsplatform til syntese af hybride heterostrukturer med valgfrie kombinationer af halvlederende og superledende materialer. Superlederne deponeres på halvledende nanotråde igennem en skyggemaske indbygget i dyrkningsubtratet uden at bryde højt vakuum, hvilket sikrer høj kvalitet og renlighed i grænsefladerne. Denne skalérbare teknik er brugt til at realisere de mest anvendte device-arkitekturer for halvledende/superledende hybrider. Karakterisering af elektrontransport i hybriderne ved kryogenske temperature viste et forhøjet udbytte i funktionelle devices og højere elektrostatisk stabilitet sammenlignet med ætsede devices. Udover fremstilling af Al/InAs hybrider til at sammenligne med devices fabrikeret med ætsning, blev skyggemaskeplatformen brugt til at producere InAs nanotråde med strukturer af superledende indium, vanadium, tantal og niobium.

Transmission elektronmikroskopi blev benyttet til at karakterisere hybridernes krystallinitet og korrelere denne med deres superledende egenskaber i form af elektron transport ved kryogeniske temperaturer. Forskellige grader af krystallinitet blev observeret i superlederne, fra epitaksielle krystaller i aluminium og indium til amorfe eller nanokrystallinske tyndfilm af tantal, vanadium og niobium. Årsagen til disse morfologiers tilblivelse i tyndfilm kan findes i sammenspillet mellem nukleationssandsynligheden, overfladeenergier og spænding i grænsefladerne. Udforskningen af forskellige hybride materialer øger vores forståelse af superledende egenskaber i nanomaterialer, heriblandt forudsætningerne for at inducere hårde superledende gap i hybride materialer. Overordnet set viser resultaterne af denne afhandling at epitaksi ikke er en forudsætning for at inducere hårde superledende gap i alle superledere. Det er derimod muligt at jævne, rene grænseflader er tilstrækkeligt, såfremt at tyndfilmen har veldefinerede superledende egenskaber. Tilblivelsen af dyrkningsplatformen åbner adskillige muligheder for nye avancerede devices, nye materialekombinationer og *in-situ* passivering af aktive overflader.

Acknowledgements

This work is the result of intense teamwork between the Quantum Materials group members of Professor Jesper Nygård. Jesper is the kind of leader that takes care of you, pushing you gently towards the goals that he sets without prohibiting you from pursuing your own ideas and approaches. This kind of freedom comes with responsibility, but facilitates creative solutions to scientific challenges. I would like to thank you Jesper for giving me an opportunity to show and improve my capabilities within nanotechnology and learn a whole lot more about nanomaterials and quantum devices than I did before embarking on this journey. I have truly enjoyed my time in the group, and look forward to our continued collaborations within QDev in my new position at the institute.

A very special thanks goes to my closest colleague, Damon Carrad. You have been a true inspiration of performing scientific work. Showing me the ways of the cryostat and nanowire device fabrication and scientific writing was always enjoyable, since it also meant spending time with your fantastic humour. I hope we can continue to share memorable times together also involving our common interest in music. I would also like to thank Thomas Sand Jespersen for being a source of genius ideas, always asking the right questions and for sharing his wonderful intuition of quantum transport amongst many other things.

The vast majority of my working hours spent in this project went into the fabrication process development of the shadow mask platform. A journey that started by building walls, but poetically enough ended in building bridges. I would like to thank Shivendra Upadhyay and Filip Krizek for invaluable input during this development. Another major part of this work involved transmission electron microscopy in which Elisabetta Fiordaliso and Erik Johnson have been a great support in helping me studying our materials in the microscopes at DTU. I am delighted that you took the time to assist me by the TEMs and share your great knowledge with me. Successful InAs nanowire growths were instrumental to this project and so I would like to applaud Thomas Kanne and Martin Aagesen for realising these.

For my change of scientific environment I visited the groups of Lucia Sorba and Francesco Giazotto at NEST in the lovely Tuscan city of Pisa. I would like use this opportunity to thank you both again, along with researchers Valentina Zannier, Elia Strambini and Nadia Ligato for helping me perform the experiments and for taking very good care of me during my stay.

Finally I would like to thank Innovation Fund Denmark - Quantum Innovation Center (Qubiz) and the Niels Bohr Institute for financial support of the project.

List of publications

These publications are referred to in the text as Pub. A, B, etc.

Peer-reviewed journal articles

A **Superconducting vanadium/indium-arsenide hybrid nanowires**
M. Bjergfelt, D. J. Carrad, T. Kanne, M. Aagesen, E. M. Fiordaliso, E. Johnson, B. Borzoyeh, C. J. Palmstrøm, P. Krogstrup, T. S. Jespersen, J. Nygård.
Nanotechnology **30, 294005** (2019).

Contributions: MB and DJC processed substrates/devices and performed transport measurements. TK, MA, BB, CJP and PK grew the hybrid nanowires. MB, EMF and EJ performed transmission electron microscopy. MB prepared the manuscript with input from all authors.

B **Shadow lithography for in-situ growth of generic semiconductor/superconductor devices**
D. J. Carrad*, M. Bjergfelt*, T. Kanne, M. Aagesen, F. Krizek, E. M. Fiordaliso, E. Johnson, J. Nygård, T. S. Jespersen
Pre-print: arXiv:1911.00460. Submitted November 1st, 2019.

Contributions: *Contributed equally. DJC, MB, FK, JN, TSJ developed the shadow lithography platform. MB and DJC processed substrates/devices and performed transport measurements. TK and MA grew the hybrid nanowires. MB, EMF and EJ performed transmission electron microscopy. DJC, TSJ, MB and JN prepared the manuscript with input from all authors.

Patents

This work has this led to the following patent applications:

A **Method and substrate for patterned growth on nanoscale structures**
M. Bjergfelt, D. J. Carrad, T. S. Jespersen, J. Nygård.
European Patent application number: **EP18163624.2** (Filed March 2018).

B **Method for manufacture of nanostructure electrical devices**
M. Bjergfelt, D. J. Carrad, T. S. Jespersen, J. Nygård.
European Patent application number: **EP18182199.2** (Filed July 2018).

These patents are referred to in the text as Patent A, B.

List of abbreviations

ABS Andreev bound states

ALD Atomic layer deposition

BCC Body-centred cubic

BHF Buffered hydroflouric acid

EBL Electron beam lithography

FCC Face-centred cubic

FWHM Full width at half maximum

JJ Josephson junction

MBE Molecular beam epitaxy

MBS Majorana bound states

NBI Niels Bohr Institute

NW Nanowire

SAD Selected area diffraction

SE Semiconductor

SEM Scanning electron micrograph

SU Superconductor

TEM Transmission electron micrograph

UHV Ultra-high vacuum

vdW van der Waals

VLS vapour-liquid-solid growth

WZ Wurtzite

Qdev Center for Quantum Devices

ZB Zinc-blende

Contents

1 Semiconductor-superconductor hybrid nanowires **15**

2 Characterisation techniques **19**
2.1 **Structural characterisation by Electron Microscopy** 19
2.1.1 Electron Microscopes 19
2.1.2 Applied techniques of the transmission electron microscope 20
2.2 **Low temperature electron transport** 26
2.2.1 Setup 26
2.2.2 Device schemes 26
2.2.3 Device fabrication 29

3 Results **31**
3.1 **Shadow masks for *in-situ* hybrid nanowire growth** 32
3.1.1 Platform concept and features 32
3.1.2 Double-angle evaporation schemes 34
3.1.3 Double-sided shadow masks 35
3.1.4 Full-shell shadow masks 36
3.1.5 Geometrical considerations 37
3.1.6 Platform fabrication 38
3.1.7 Nanowire growth schemes 41
3.1.8 Chemical Beam Epitaxy integration 43
3.1.9 Conclusions and outlook 44
3.2 **Al/InAs hybrid nanowires** 45
3.2.1 Sample descriptions 45
3.2.2 Structural characterisation 45
3.2.3 Electrical characterisation 47
3.2.4 Conclusions and outlook 52
3.3 **In/InAs hybrid nanowires** 53
3.3.1 Sample descriptions 53
3.3.2 Structural characterisation 55
3.3.3 Electrical characterisation 60
3.3.4 Conclusions and outlook 61
3.4 **V/InAs hybrid nanowires** 62

3.4.1 Sample descriptions 62
3.4.2 Structural characterisation 64
3.4.3 Electrical characterisation 67
3.4.4 Conclusions and outlook 68
3.5 **Ta/InAs hybrid nanowires** 70
3.5.1 Sample descriptions 70
3.5.2 Structural characterisation 70
3.5.3 Electrical characterisation 72
3.5.4 Conclusions and outlook 75
3.6 **Nb/InAs hybrid nanowires** 76
3.6.1 Sample descriptions 76
3.6.2 Structural characterisation 76
3.6.3 Electrical characterisation 76
3.6.4 Conclusions and outlook 78

4 Conclusions and outlook **81**

5 Appendix **95**
5.1 Shadow mask fabrication recipe 95
5.2 Supplementary structural data: Indium 98

Chapter 1

Semiconductor-superconductor hybrid nanowires

Superconductors (SUs) and semiconductors (SEs) are two classes of materials that have been subjects of intensive research since their discoveries more than a century ago, in part due to their technological relevance [1, 2], but also the possibilities they offer to give insight into fundamental physics [3, 4]. Superconductors are distinguished by dissipationless transport [5], the Meissner effect of magnetic field expulsion [6], and being excellent electromagnets [7]. Since these properties are only available at cryogenic temperatures [6], a vast amount of research is going into realising superconductivity closer to room temperatures to broaden the scope of applications [8]. Semiconductors on the other hand, are distinguished by carrier density variability and field-effect tunability applied in transistors [9]. Transistors form the basis of the digital age by being used for classical computation and electrical amplification [1]. The field-effect tunability is also the underlying effect used to define mesoscopic and nanoscale quantum devices where low temperature properties of semiconductors such as the g-factor and spin-orbit coupling can be explored and utilised [3]. Individually, these two material classes are already sources of fascinating science and technology. In combination they are arguably even more so.

When a SU is placed in good electrical contact to a normal conductor, the normal conductor can take on superconducting-like properties, such as the ability to transmit a dissipationless supercurrent and having a gap in the density of states around the Fermi energy. This effect, known as the superconducting proximity effect [10, 11], offers numerous possibilities when applied to SEs. Aside from the ability to tune the magnitude of the dissipationless supercurrent using electric fields [12], certain SU/SE hybrids attract considerable interest due to their importance in the now-pervasive field of topology of condensed matter. The interest originates from proposals stating that coupling SUs to topological insulators [13, 14, 15] or materials with high g-factor and spin-orbit coupling [16, 17, 18, 19, 20] can lead to exotic phases of superconductivity. A pertinent example is the topological Majorana fermion, first observed in InAs and InSb SU/SE hybrid nanowire systems [21, 22], which was suggested to find application in topologically protected quantum information processors [23, 24, 25, 26, 27, 28, 29, 30].

One of the initial challenges towards Majorana fermion compatible SU/SE nanowires was the 'softness' of the proximitised superconductivity i.e. the presence of a continuum of conductance states in the superconducting gap ultimately impairing the topological protection [31, 32]. The sub-gap states were induced from interface disorder due to surface oxides formed during *ex-situ* transfer between vacuum systems for nanowire (NW)

growth and deposition of SU [33]. Improvements were made by removing the NW surface oxide and chemically passivating with sulfur removed under vacuum before SU deposition [34], but the superconducting gap in the hybrids nanowires remained mostly soft [33].

To ensure effective proximitation of superconductiviy in the hybrid NWs, methods for growing disorder-free 'hard-gap' SU/SE epitaxial hybrids were developed (Fig. 1.1)[35, 36, 37]. These materials utilise bottom-up vapour-liquid-solid (VLS) [38] molecular beam epitaxy (MBE) crystal growth of wurtzite InAs nanowires with uniform epitaxial aluminium coatings (Fig.1.1**a-c**) [35]. Comparing epitaxially MBE-grown Al/InAs to Al evaporated onto InAs *ex-situ* (Fig. 1.1**d-g**) showed that the epitaxial Al suppressed the subgap condutance by two orders of magnitude, indicating a significant reduction in the density of interface impurity states compared to the evaporated counterpart [36]. The epitaxial Al/InAs approach has been extended to high mobility two-dimensional systems [39, 40] and selective area grown networks [41, 42]. The success of epitaxial Al/InAs hybrids lies in the dual benefits of having a disorder-free, pristine interface, as well as the the ability to realise important device classes such as normal metal spectroscopic devices [36, 39, 40, 43], Josephson junctions [44, 45, 46, 47] for gate-controlled transmon qubits [48, 49], and superconducting Majorana islands [50, 51, 52], using top-down processing to selectively remove the aluminium. A limitation of this method is that relying on post-process etching inherently limits materials choice. For instance, despite strong incentives to utilize technologically important superconductors such as Nb [53] and NbTiN [33] – which exhibit higher transition temperatures, critical magnetic fields and superconducting energy gaps – selectively removing Nb from InAs remains an unsolved problem. Similarly, InSb is an attractive semiconductor due to its high mobility [54, 55, 56] and strong spin-orbit coupling [57]. Yet, selectively removing even aluminium from InSb remains similarly unsolved. Using SUs with higher critical temperatures and critical field compared to Al would encourage the development of topological quantum computers operating at liquid helium, or even liquid nitrogen temperatures if high-T_c cuprate superconductors could be employed. An attractive approach to eliminate etching and study NW hybrids based on other SUs is to employ an *in-situ* 'shadow approach' to mask sites from superconductor growth. Initial progress was demonstrated in Refs. [58, 59] where deterministically positioned nanowires were shadowed by adjacent nanowires. This approach, however, requires accurate control of relative NW positions and growth directions. Further, the range of the possible device geometries is limited since only narrow shadow gaps of length equal to nanowire diameter are possible.

In this thesis, a flexible shadow mask platform for growing device-ready SU/SE NWs hybrids in numerous geometries is demonstrated. The platform features a combination of pre-growth fabrication of shadow structures directly on NW growth substrates with precise positioning of NW growth sites and full *in-situ* control of the orientation of superconductor flux. The platform is independent of materials choice (SU,SE) and so simultaneous wafer-scale growth of the most important hybrid architectures using aluminium, indium, vanadium, tantalum and niobium is demonstrated. Structural characterisation and low temperature electron transport measurements of all the hybrid NWs are presented to correlate the crystallinity of the SU films to their superconducting properties. Overall it is shown that the platform produces high quality materials towards deployment in topological quantum computation schemes. Additionally, the free materials choice enables deeper understanding of the structure and electrical behaviour of nanoscale superconductors and hybrid devices.

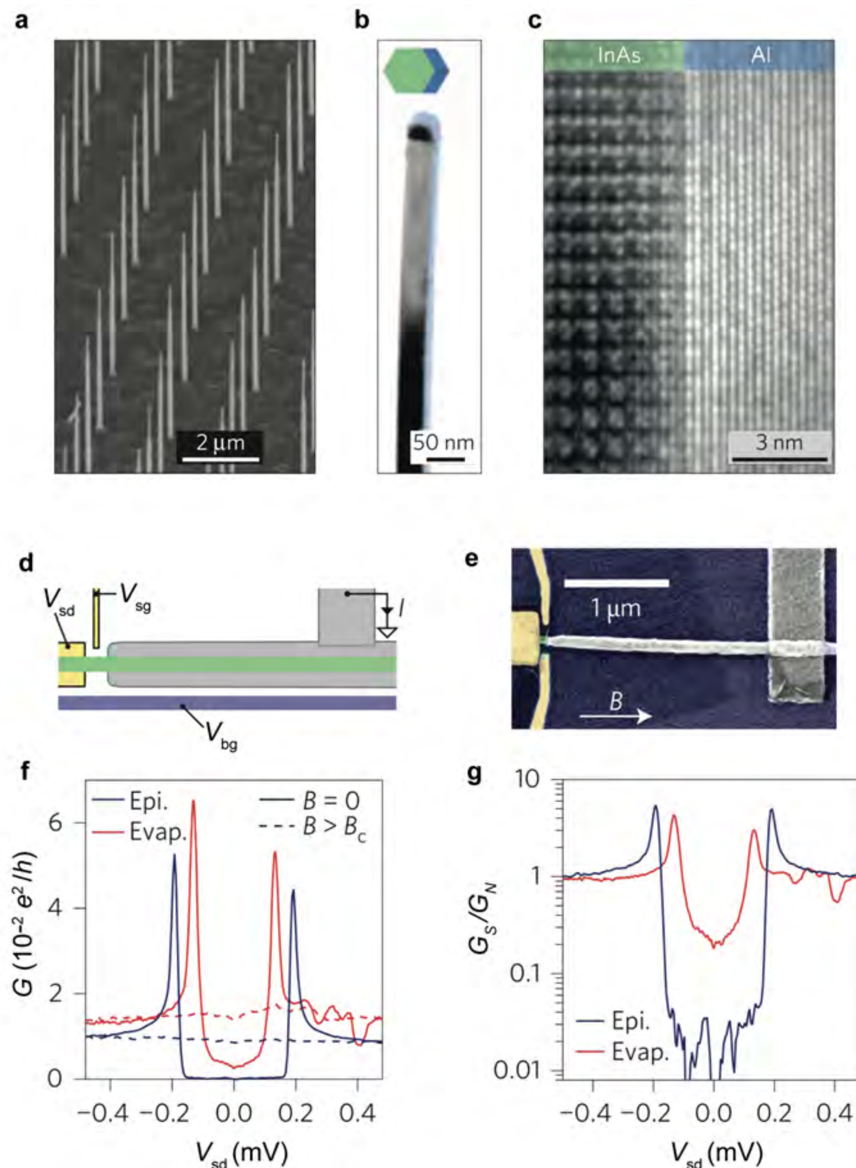

Figure 1.1: **Hard proximitiy-induced superconducting gap in epitaxial Al/InAs nanowires a** Scanning electron micrograph of an array of as-grown Al/InAs from Au catalysts deterministically positioned using electron beam lithography. **b** Transmission electron micrograph of an InAs nanowire with two of six facets coated by aluminium (false-colored blue - schematically shown in insert). The dark contrast at tip of the NW is the Au catalyst from which the NW was grown. **c** High-resolution transmission electron micrograph showing the impurity-free, epitaxial interface between an InAs NW facet and aluminium. **d** Device schematic for tunnel spectroscopy used to measure the proximity-induced superconducting gap. The schematic features Ti/Au leads for source-drain bias $V_{\rm sd}$ and electrostatic side gate $V_{\rm sg}$ (yellow), InAs nanowire (green), Al shell (grey), and an oxide coated Si substrate for applying a back gate potential $V_{\rm bg}$ (purple). **e** False-colored scanning electron micrograph the device. **f** Differential conductance G as a function of source–drain voltage $V_{\rm sd}$ of an epitaxial full-shell device (blue) and an evaporated control device (red) at $B = 0$ (solid line) and above the critical field $B > B_c$ (dashed line). **g** Normalized differential conductance. Epitaxial full-shell nanowires exhibit subgap conductance suppression by a factor of $\sim$ 50-100 while the hybrid exposed to oxygen prior to Al evaporation had a 'soft' gap only with a conductance suppression of $\sim$ 5. Figures were adapted from Refs. [35, 36]

.

Chapter 2

Characterisation techniques

This chapter presents the applied techniques enabling characterisation of structural and electronic transport properties of hybrid nanowires. Processed substrates for hybrid nanowire growth, as-grown nanowire substrates and finished devices were characterised using scanning electron beam microscopy, providing feedback on fabrication processing and overall hybrid nanowire morphology. Being $\sim$100-200 nm in diameter, the hybrid nanowires were electron beam transparent at the acceleration voltages of a transmission electron microscope, commonly operated in the 200-300 kV range[60]. This transparency made the nanowires an ideal platform for structural characterisation using techniques in transmission electron microscopy such as electron beam diffraction from selected areas of $\sim 1\ \mu\text{m}^2$ and high resolution imaging of the hybrid interfaces at the atomic scale. Electron transport measurements were conducted at cryogenic temperatures to study superconductivity and quantum electron transport in the hybrids.

2.1 Structural characterisation by Electron Microscopy

The aim of the structural characterisation using electron microscopy was to characterize the morphology/crystallinity of the superconductor thin film nanowire shells. In case of single- or polycrystalline films, the aim was furthermore to characterize any epitaxial relation between the semiconductor nanowire and superconducting thin film. Finally, electron microscopy enabled characterisation of termination abruptness in the junctions made using shadow lithography. The abbreviations 'SEM' and 'TEM' will be reserved to denote micrographs acquired with the respective electron microscopes and not the microscopes themselves.

2.1.1 Electron Microscopes

Scanning electron microscopy was conducting at QDev in a JEOL 7800F, operated at acceleration voltages 5-20 kV. Three different transmission electron microscopes were used in the study. For low resolution imaging and most electron diffraction, a 200 kV Phillips CM20 situated at NBI, was used. For high resolution imaging, two microscopes were used; a 300 kV JEOL 3000F at the Technical University of Denmark (DTU) Risø campus and a probe-corrected and monochromated 300 kV FEI Titan Analytical 80-300ST at DTU Center for Nanoscopy (DTU CEN) in Lyngby Campus.

Sample preparation

Individual nanowires were transferred from the growth substrate to carbon membrane covered copper grids using a micro-manipulator with needles of tip diameter 100-250 nm. The transfer proceeded by placing the needle and sample under an optical microscope and use the micro-manipulator to bring the needle close to a single NW grown in the processed substrates. Bending the NWs with the needle until breaking off the substrate resulted in the NW adhering to the needle tip by van der Waals (vdW) forces. Subsequently moving the needle to the surface of a carbon membrane grid, the NW was carefully brought into contact with the carbon membrane surface. Once the membrane contact area to the NW exceeded that between the needle and NW, the NW would stick to the membrane surface as shown in Fig. 2.1.

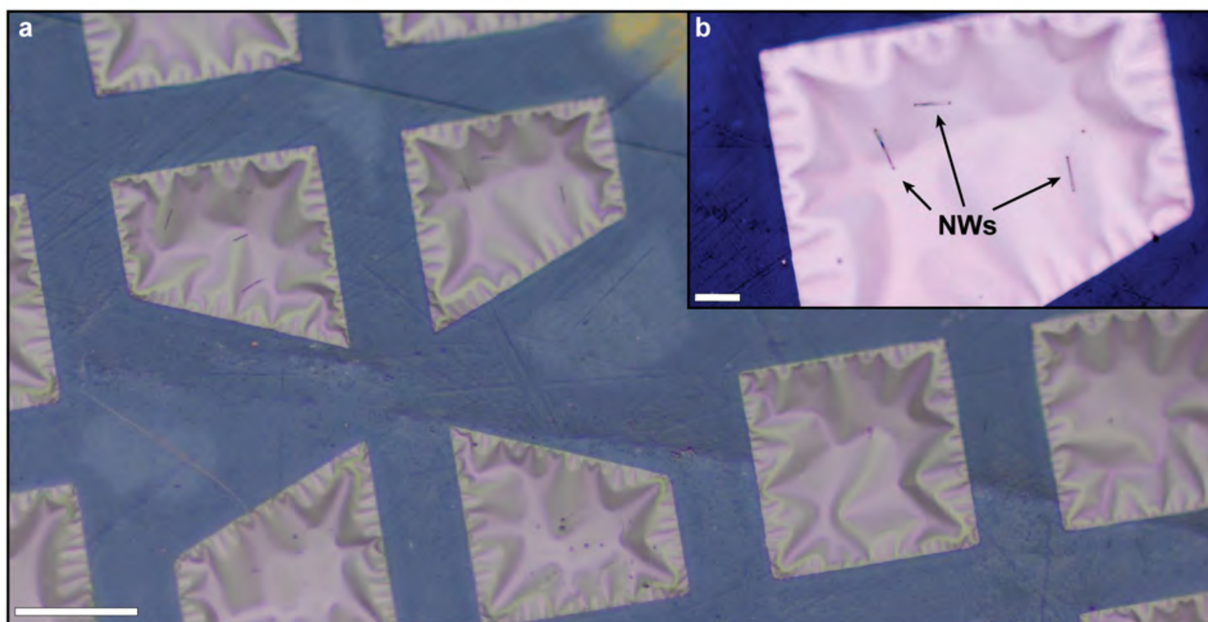

Figure 2.1: **Centre of TEM sample grid with NWs placed on the carbon membranes by a micro-manipulator.** Scale bars: **a**: 20 μm, **b**: 5 μm.

2.1.2 Applied techniques of the transmission electron microscope

Different imaging techniques were applied to acquire transmission electron micrographs (TEMs) and diffraction patterns (DPs). Ray diagrams in Fig. 2.2 illustrate the two basic imaging modes of the transmission electron microscope “diffraction mode” (Fig. 2.2**a**) and “imaging mode” (Fig. 2.2**b**). The ray diagrams are highly simplified as most transmission electron microscopes have many more imaging lenses, which give greater flexibility in terms of magnification and focusing range for both TEMs and DPs.

At the top of the schematics in Fig. 2.2**a**, parallel electron beams enters the sample specimen and is transmitted either directly, or through scattering from sample interactions e.g. diffraction. After passing a condensing objective lens, beams scattered by the same angle pass the same point in the back focal plane (BFP) like the green and red rays in Fig. 2.2**a** where the intersections are marked by a red dots. Up until reaching the intermediate lens, the two imaging modes are identical. The strength of the intermediate lens determines the object of the projector lens, which produces the final image on the screen. For “diffraction mode”, the object is an

intermediate image of the BPF whereas for "imaging mode", the object is an intermediate image of the real space image indicated by blue arrows in Fig. 2.2**b**.

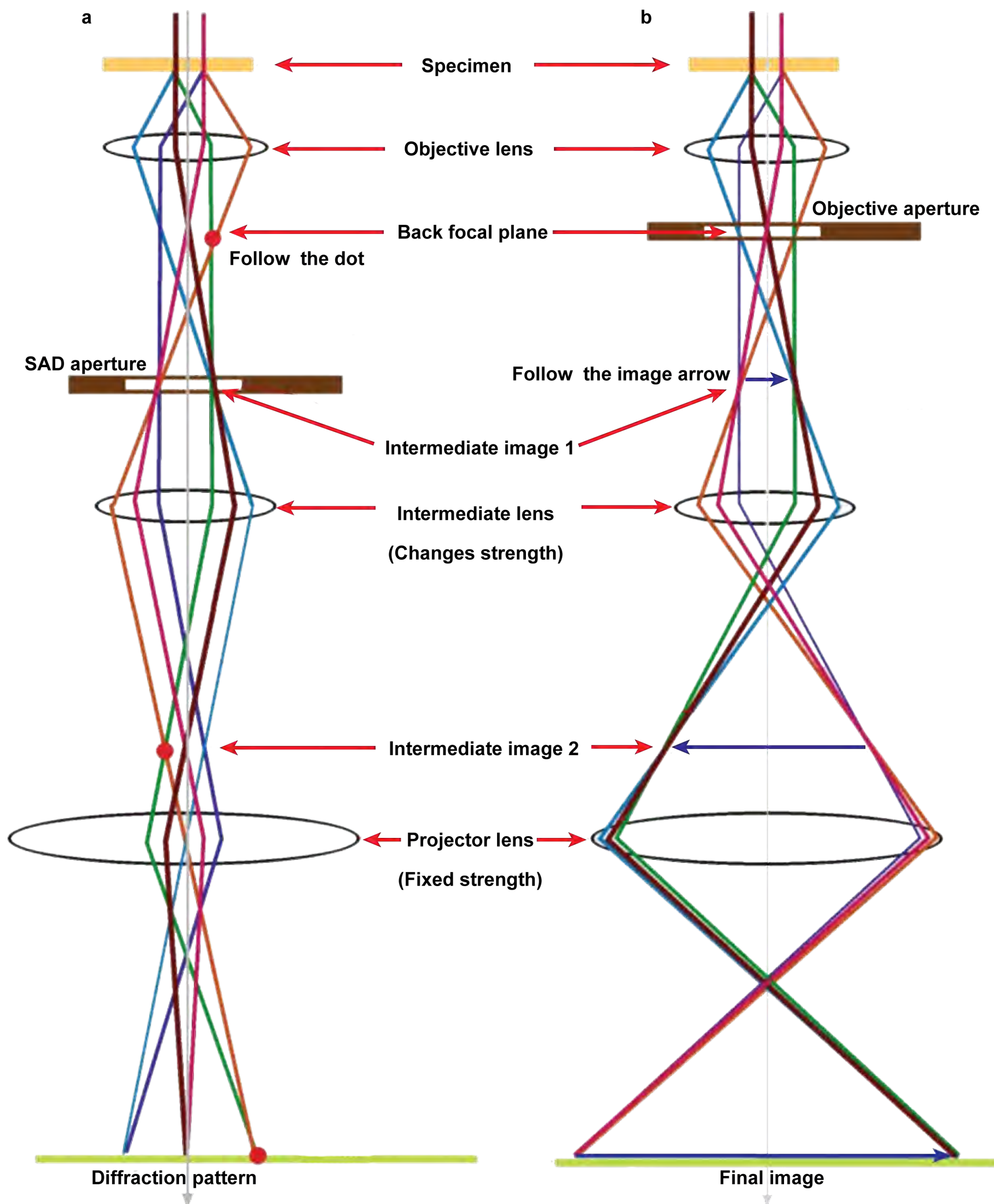

Figure 2.2: **Schematic ray diagrams of TEM operation modes.** The two basic operations of the TEM imaging system involve **a** diffraction mode: projecting the diffraction pattern onto the viewing screen and **b** image mode: projecting the image onto the screen. In each case the intermediate lens sets either the BFP **a** or the image plane **b** of the objective lens as the object for the projector lens. The SAD and objective apertures are appropriately inserted or retracted in both modes for different techniques, as explained in the main text. Schematics are adapted from Ref. [60].

Selected-area diffraction

In “diffraction mode” (Fig.2.2**a**) the DP contains electrons from the whole area of the specimen that is illuminated by the beam. Such a pattern is not always very useful since hybrid nanowires often are bent due to e.g. interfacial strain. A specific area of the specimen can be selected to contribute to the DP by in two ways. One way would is reduce the illuminated area of the specimen contributing to the DP by using lenses above the specimen to converge the beam to a smaller spot on the specimen. In diffraction mode this generates “convergent beam electron diffraction” (CBED) patterns, which will be shown later when introducing nanowire alignment. Converging the beam destroys any parallelism, and spots in the diffraction pattern will not be sharply defined but spread into disks [60]. When we wish to obtain a DP with a parallel beam of electrons, the standard way is to introduce an aperture, called the “selected-area diffraction” (SAD) aperture. The SAD aperture is inserted in a plane conjugate with the specimen, i.e., in one of the intermediate image planes of an imaging lens, which creates a virtual aperture at the plane of the specimen. This operation is called “selected-area diffraction” or SAD, and is schematically shown in Fig. 2.2**a** where a SAD aperture is inserted in intermediate image 1 which is the image plane of the objective lens. No matter what kind of specimen is illuminated, if transmission of electrons occurs, the SAD pattern will contain a bright central spot that contains the direct beam electrons and some scattered electrons (as shown in Fig. 2.3), the distribution of which will depend on the crystallinity of the specimen. Fig 2.3**a** show a SAD signal from crystalline Al where distinct Bragg peaks away from the central spot originate from electron being diffracted from Bragg scattering off crystal planes. Fig. 2.3**b** shows the SAD signal from polycrystalline Au, where Debye-Scherrer rings represent scattering off a crystal planes in a multitude of angles [60, 61]. Fig. 2.3**c** shows a SAD signal from a carbon membrane with diffuse halo-like rings indicating an amorphous morphology.

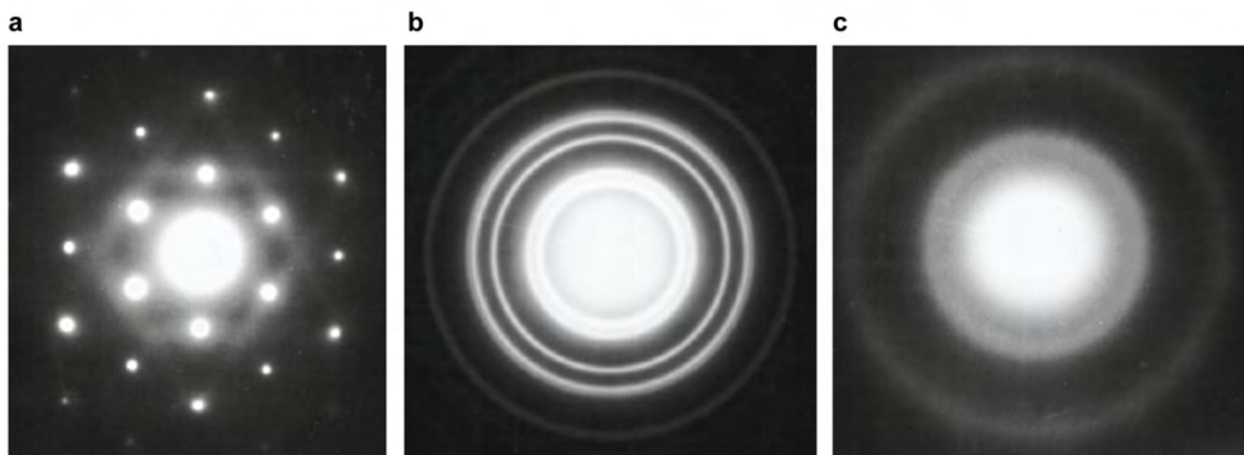

Figure 2.3: **Electron diffraction patterns. a** Crystalline Al. **b** Polycrystalline Au. **c** Amorphous carbon. The direct beam of electrons is responsible for the bright intensity at the centre of the patterns and the scattered beams account for the spots or rings that appear around the direct beam. DPs are adapted from Ref. [60].

Bright Field and Dark Field imaging

With the SAD pattern projected onto the viewing screen, the pattern can be used to perform the two most basic imaging operations in the TEM, bright field (BF) and dark field (DF) imaging. The imaging operations are performed by introducing an aperture, called the “objective aperture”, in the BFP of the objective lens. The

objective aperture is visible on the viewing screen since the BFP is the image object in diffraction mode, and can be centred around either the direct beam spot or a diffracted spot to exclusively generate the image from the direct beam (BF) or a diffracted part of the beam (DF). Since BF is generated from the directly transmitted electrons, any regions with intensity loss will be due to electrons scattering in the specimen. These will be seen as dark features in a bright background. An example is seen BF imaging bend crystalline NWs where dark bending contours appear due to the orientation of the diffracting planes changing as the crystalline NW is bend, i.e., when the diffracting planes tilt relative to the beam, the contrast changes. DF images have a dark background with bright features in the regions from which the selected diffracted electron originated e.g from crystal planes in thin film grains.

Alignment of InAs nanowires

Imaging hybrid nanowire interfaces relies on accurate alignment of the nanowire facets with respect to the electron beam. In order to characterize e.g. crystal epitaxy, ideally the coated nanowire facet is aligned perfectly parallel to the electron beam. One approach to achieve accurate alignment is to take advantage of the high symmetry of the nanowire crystal and use diffraction signatures of the $\{1\bar{1}00\}$ facet planes and $\{0001\}$ axial growth planes. In the $\langle 2\bar{1}\bar{1}0\rangle$ zone-axes the diffraction (Bragg) peaks from both set of planes are simultaneously visible and orthogonal, a nanowire facet is thus aligned parallel the electron beam. If this NW facet is coated by e.g. a superconducting metal, the interface should be visible as an abrupt transition from one material to the other.

Navigating to the high symmetry nanowire zone-axes featuring the facet and growth planes is eased by condensing the electron beam onto the nanowire, enter diffraction mode to generate a CBED pattern, and use emerging Kikuchi lines to navigate the reciprocal space. Kikuchi lines arise from incoherent electron scattering which can be Bragg diffracted from crystal planes as line pairs and and serve as a map to high symmetry orientations [60, 62]. Condensing the beam has the two-fold advantage of effectively increasing the range of incident angles at which the electrons enter the crystal and scatter off crystal planes, as well as localising the origin of the signal to a small area.

Aligning to the high symmetry $\langle 2\bar{1}\bar{1}0\rangle$ zone-axis (ZA) in a InAs NW is illustrated in Fig. 2.4. In Fig. 2.4**a** the NW is put at the centre of the screen and the beam is converged (Fig. 2.4**b**). Entering the diffraction mode (Fig. 2.4**c**) Bragg peaks and Kikuchi lines are visible. Indicated by converging Kikuchi lines (Fig. 2.4**d**) it is possible to navigate towards the high-symmetry zone axes by tilting the sample holder. In Fig. 2.4**e** a position close to a zone axis is shown, while in **f** the sample is perfectly aligned to the $[2\bar{1}\bar{1}0]$ zone axis. If the SAD aperture is inserted and the beam spread out, a SAD pattern can be obtained as seen in Fig. 2.4**g** exhibiting orthogonal $\{1\bar{1}00\}$ and $\{0001\}$ planes. In Fig. 2.4**h** BF TEM of the aligned InAs NW is shown. Fig. 2.4**i** shows a High-resolution TEM with lattice fringes from the (0002) and $(1\bar{1}00)$ planes visible in InAs.

High-resolution imaging

High-resolution transmission electron microscopy is an imaging mode that uses a series of imaging lenses to create electron wave interference as a consequence of phase-shifts occurring in the electron wave while it interacts with the specimen during transmission. The phase contrast contained in the interference can be used to project the crystallographic structure of the specimen with atomic resolution. To obtain atomic resolution, the technique relies on amending aberrations in the electron wave induced by the magnetic fields of the beam-forming

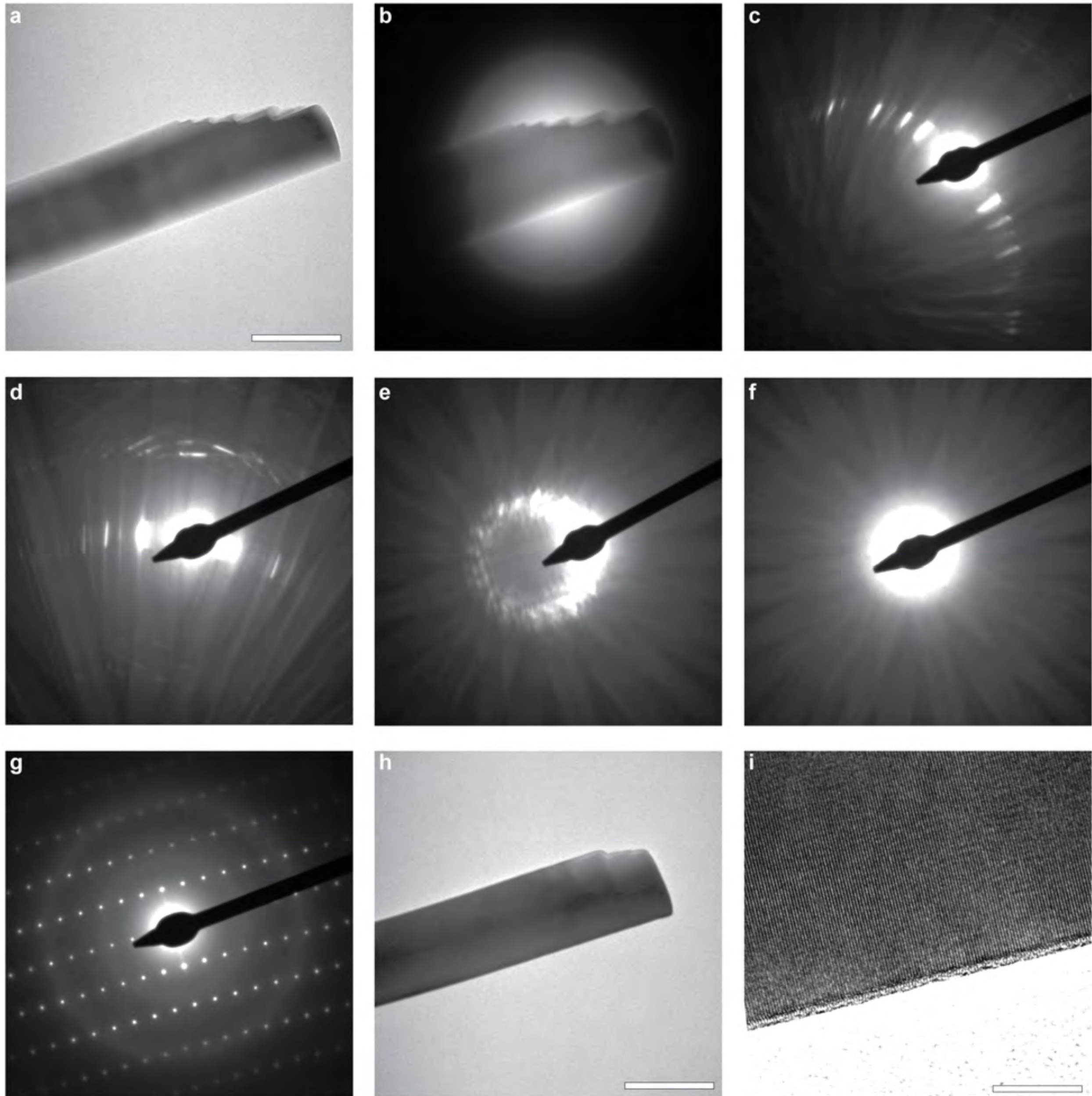

Figure 2.4: **Aligning the nanowire to high-symmetry zone-axes in TEM. a** BF TEM of the bottom part of a nanowire, slightly damaged from breaking with the growth substrate. **b** The electron beam is condensed on the area of interest. **c-e** In diffraction mode, CBED patterns show converging Kikuchi lines which, while tilting the sample, are used to align a the high-symmetry $\langle 2\bar{1}\bar{1}0 \rangle$ zone-axis. **g** SAD pattern of a $\langle 2\bar{1}\bar{1}0 \rangle$ zone-axis. **h** BF TEM of the facet-aligned InAs nanowire. HRTEM of the nanowire facet with visible lattice fringes from the NW crystal. The facet is terminated by a surface oxide. Scale bars: **a,h**: 100 nm, **i**: 10 nm.

and image-forming electromagnetic lenses, as well as aberration from not having monochromatic electrons emitted from the electron beam source [60]. Aligning the specimen to have the electron beam parallel to crystal planes can produce HRTEMs with lattice fringes representing contrast induced from phase-shift as the electron wave passes atomic planes, as demonstrated in Fig. 2.4**i** for a facet-aligned InAs NW. Abrupt interfaces between NW facets and thin films can be resolved this way. If low-index planes in thin film grains also are parallel to the interface, crystallographic relations between the two materials, e.g. epitaxy, can be determined. Measuring interplanar distances in lattices fringes and angles between crossing fringes in the thin film grains, can be used to characterise the crystal structure by comparing it to known crystal phases. Lattice fringes with abnormal periodicity compared to atomic lattice fringes can occur by interference between overlapping crystal grains with translationel or rotational offset between them. These are known as Moiré lattice fringes [63].

2.2 Low temperature electron transport

2.2.1 Setup

Electron transport measurements were performed in an Oxford Triton ^{3}He/^{4}He dilution refrigerator with a base temperature $\sim$ 15 mK. A dilution refrigerator operates on the principle of the formation of a phase boundary between a ^{3}He-rich phase (the concentrated phase) and a ^{3}He-poor phase (the dilute phase) at $\sim T = 0.9$ K. Pumping ^{3}He from the dilute phase results in ^{3}He from the concentrated phase being pulled across the phase boundary – an endothermic process that cools the system [64]. The Triton was equipped with a 'vector magnet' consisting of three independent, perpendicularly oriented coils capable of supplying $B_x = B_y = 1$ T and $B_z = 6$ T . All measurements were done using lock-in amplifiers (Standford Research Systems SR830) at low frequency ($\sim$ 200 Hz) to measure differential conductance $G = dI/dV$. Electrostatic gate potentials were applied using Keithley 2400 or 2614B SourceMeters or National Instruments digital-to-analog converters (NI DACs). Source-drain voltages were supplied by NI DACs. The Keithley allowed monitoring of the gate leakage and ensure that $I_g < 1$ nA throughout the measurements.

2.2.2 Device schemes

Four terminal measurements

In the four terminal device scheme (Fig. 2.5), four electrodes contact the superconductor/semiconductor nanowire. A constant ac current I is sourced along the nanowire, and the voltage drop V between the two inner contacts measured. Measuring the voltage drop using separate terminals eliminates lead and contact resistances from the measurement, as no current passes in or out of the voltage terminals. The properties of the semiconducting NW core is not studied in this configuration since the conductance of the metallic film is much larger than the NW. In two terminal measurements, the contact resistance (usually $\sim$kΩ) dominate and realising the few Ohm change across the superconducting transition is challenging. Four terminal resistance measurements were performed while sweeping a magnetic field B or the temperature T to determine the critical field B_C and critical temperature T_C of the superconductors i.e. transition between a finite and zero-resistance conductance state [6].

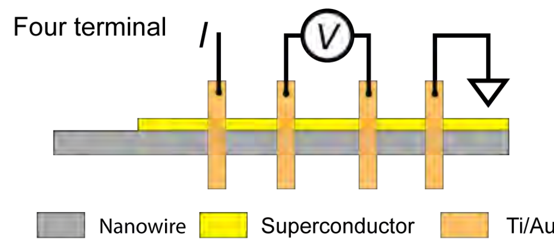

Figure 2.5: **Device schemes four terminal measurement of resistance.**

Tunnel spectroscopy scheme

The tunnel spectroscopy device scheme (Fig. 2.6**a**), involves sourcing a bias between a contact to the superconductor and a contact to an exposed NW segment. In-between the source-drain contacts, an electrostatic side gate potential, V_g, or a back gate potential, V_bg, is used to induce a quantum dot (QD) or quantum point contact (QPC)

tunnel barrier in the NW segment. Lock-in amplification is used to measure the the differential conductance, $G = dI/dV_{\text{sd}}$ through the QD or QPC, which in the tunnelling regime ($G \ll G_0 = 2e^2/h$) is proportional to the density of states [21, 36, 43, 65]. Measuring G while sweeping the source-drain bias, V_{sd}, and stepping the gate voltage, V_{g} to alter the number of conducting modes and/or density of states in the system results in bias spectra and line traces like shown in Fig. 2.6**b**. The data is from a Al/InAs nanowire hybrid reported in Ref. [36]. Two coherence peaks separated by $2\Delta/e \sim 0.36$ mV represent the proximitised induced superconducting energy gap. G vs. V_{sd} trace from the red line at $V_{\text{bg}} = -12$ in Fig. 2.6**b** is shown in Fig. 2.6**c**(red) along with a trace from the high conductance regime at $V_{\text{bg}} = 3.8$ V (blue) where the transmission is stronger and a sub-gap enhancement is observed due to Andreev reflections.

A figure of merit for conductance suppression in proximitised induced superconducting gaps is the gap hardness, $G_{\text{N}}/G_{\text{S}}$, where G_{S} is the zero bias conductance $G_{\text{S}} = G(V_{\text{sd}} = 0\text{ mV})$ and G_{N} is the out-of-gap conductance $G_{\text{N}} = G(V_{\text{sd}} \gg \Delta/e)$. Gap hardness was found to be $\sim 50-100$ for Al/InAs hybrids in Ref. [36]. Values of 50-100 are typically reported as 'hard gap' hybrids, while values <50 are typically indicative of a 'soft gap' due to e.g. interface impurities.

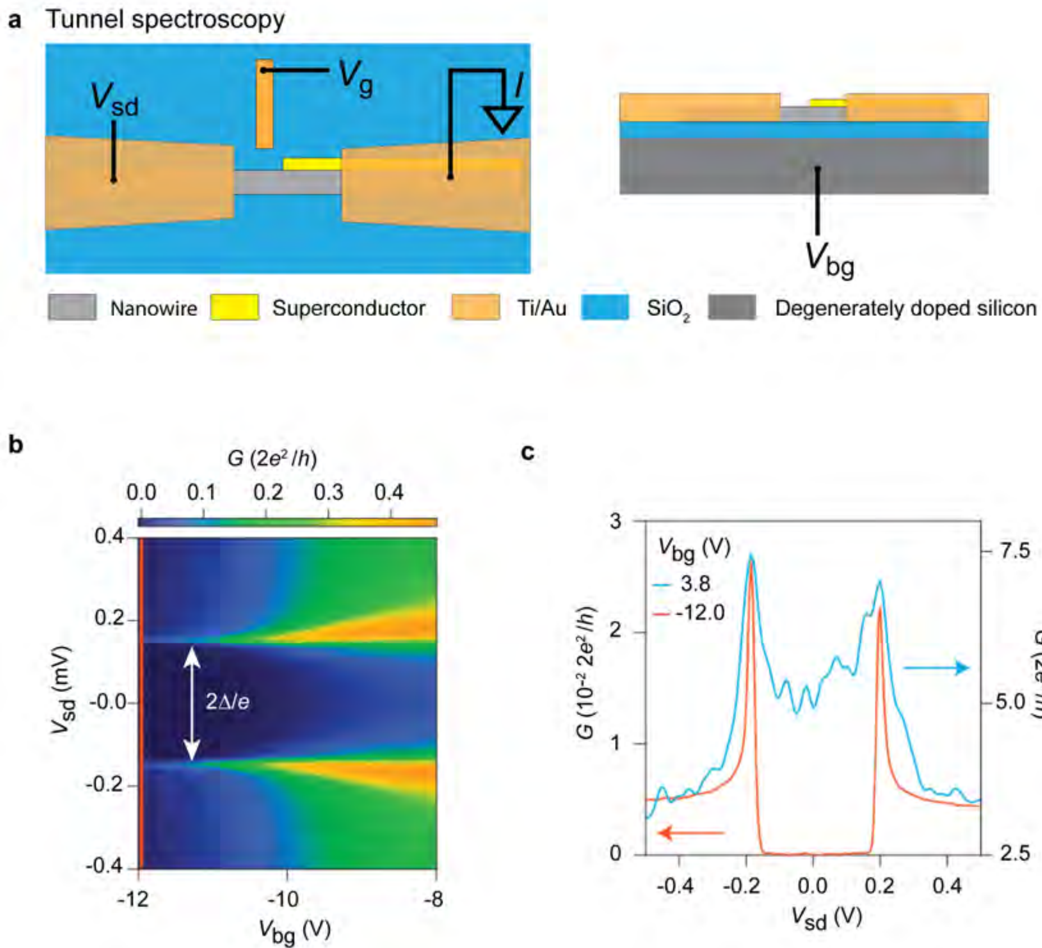

Figure 2.6: **Tunnel spectroscopy. a** Device scheme top-view (left) and side-view (right). **b** Bias spectrum from Al/InAs NW hybrid exhibiting an induced superconducting gap **c** G vs. V_{sd} line traces from the tunnelling regime at $V_{\text{bg}} = -12$ V (red) and the high conductance regime (blue) at $V_{\text{bg}} = 3.8$ V. **b-c** is adopted from Ref. [36].

Superconducting island scheme

While tunnel spectroscopy devices are the essential tool for characterising induced superconductivity, the elemental building block in most topological quantum computing architectures are superconducting 'Majorana islands' [30, 66]. As shown in Fig. 2.7**a**, the device consists of a hybrid island segment confined by three electrostatic gate potentials V_{g} and $V_{\mathrm{sg1,sg2}}$. Side gate voltages, $V_{\mathrm{sg1,sg2}}$, are used to deplete the NW leads, confining electrons (Cooper pairs, if the segment is superconducting) and introduce a charging energy, E_C, associated with the capacitive energy cost of adding charge to the island. The electron confinement is similar to the formation of a QD in the hybrid segment. Middle gate voltage, V_g, is used to tune the chemical potential, i.e. the charge, in the hybrid segment [50, 52, 67, 68].

Figure 2.7**b** (adapted from Ref. [50]) shows bias spectra of G as a function of middle gate voltage, V_{g}, and source–drain bias, V_{sd}, for parallel magnetic fields $B_{\|} = 0, 80, 220$ mT. The zero-field data (Fig. 2.7**b**, top) show a series 'Coulomb diamonds', indicating the region in (V_{g},V_{sd}) when transport is prohibited by charging energy. The diamonds are evenly spaced with the zero-bias V_g period proportional to $2e$ which reflects charge transport via Cooper pairs [50, 67]. At a moderate magnetic field $B_{\|} = 80$ mT (Fig. 2.7**b**, middle), the diamonds shrink and a new ground state appears, resulting in even–odd spacing of Coulomb-blockade zero-bias conductance peaks, as also seen from the green trace of in the bottom panel of Fig. 2.7**c**. At the larger magnetic field, $B_{\|} = 220$ mT (Fig. 2.7**b**, bottom), Coulomb diamonds are again periodic, but have half the spacing of the zero-field diamonds, corresponding to $1e$ periodicity.

The zero-bias conductance traces from the bias spectra of Fig. 2.7**b** outlined in Fig. 2.7**c**(bottom) show the associated Coulomb peaks. The phenomenon can be qualitatively understood in a zero-temperature model [50] in which the energy of the superconducting island hosting N electrons, E_N, is given by a series of shifted parabolas:

$$E_N(N_{\mathrm{g}}) = E_C(N_{\mathrm{g}} - N)^2 + p_N E_0 \tag{2.1}$$

where $N_{\mathrm{g}} = CV_{\mathrm{g}}/e$ is the gate-induced charge (with electron charge e and gate capacitance C) and N is the electron occupancy. E_0 is the energy of the lowest quasiparticle state, which is filled for odd parity ($p_N = 1$, odd N) and empty for even parity ($p_N = 0$, even N). The parabolas are illustrated in Fig. 2.7**c**(top). Transport occurs when the ground state has a charge degeneracy, i.e. when the E_N parabolas intersect (Fig. 2.7**c**(top)). For $E_0 > E_C$, the ground state always has even parity; transport in this regime occurs via tunnelling of Cooper pairs at degeneracies of the even-N parabolas. This is the regime in which the $2e$-periodic Coulomb-blockade peaks are seen at low magnetic fields (top bias spectrum in Fig. 2.7**b** and blue trace in Fig. 2.7**c**). Since the higher energy odd charge state carries spin, its energy can be lowered by the Zeeman effect when a magnetic field is applied [69]. In a sufficiently large magnetic field, such that $E_0 < E_C$, an odd-N ground state emerges. This transition from $2e$ charging to $1e$ charging is seen experimentally as the splitting of the $2e$-periodic Coulomb diamonds into the even–odd double-diamond pattern in Fig. 2.7**b**(middle) and green trace in Fig. 2.7**c**. In this regime, the Coulomb-peak spacing is proportional to E_C + $2E_0$ for even diamonds and $E_C - 2E_0$ for odd diamonds. For the particular case of a zero-energy Majorana state ($E_0 = 0$) in a finite size island, the even/odd peak spacing oscillates as a function of magnetic field due to overlap of the Majorana wavefunctions causing a split around zero energy [50]. Zero-bias peaks which oscillates with increasing magnetic field are, however, not necessarily MBS since trivial Andreev bound states (ABS) coalescing with increasing magnetic field can be

pinned exponentially close to zero energy and this way resemble the topological MBS. The pinning can occur if the chemical potential is tuned to be within the energies of the Zeeman lowered odd charge states close to zero energy and if the spin-orbit length is tuned with respect to the quantum dot length such that a Fabry-Perot-like resonance condition is satisfied [70]. Another trivial effect is a $2e$-$2e$ transition occuring with an even to odd parity change of the ground state [68]. A way to distinguish MBS from pinned ABS is to study the exponential suppression of the energy splitting for islands with varying lengths and the oscillations of the bound state with varying magnetic field [50, 71].

only for an infinitely long island. Finite island length causes overlap of the Majorana wavefunctions, and causes them to split around zero energy.

2.2.3 Device fabrication

Device fabrication proceeded by transferring selected nanowires from the growth substrate using a micro-manipulator (as described in Sec. 2.1.1) to a substrate consisting of degenerately doped Si with a SiO_2 overlayer. Ti/Au contacts were defined by electron beam lithography in an Elionix 100 kV system and deposited by e-beam evaporation in a AJA system. Evaporation was preceded by *in-situ* Ar^+ milling to remove the native oxide and ensure ohmic contact.

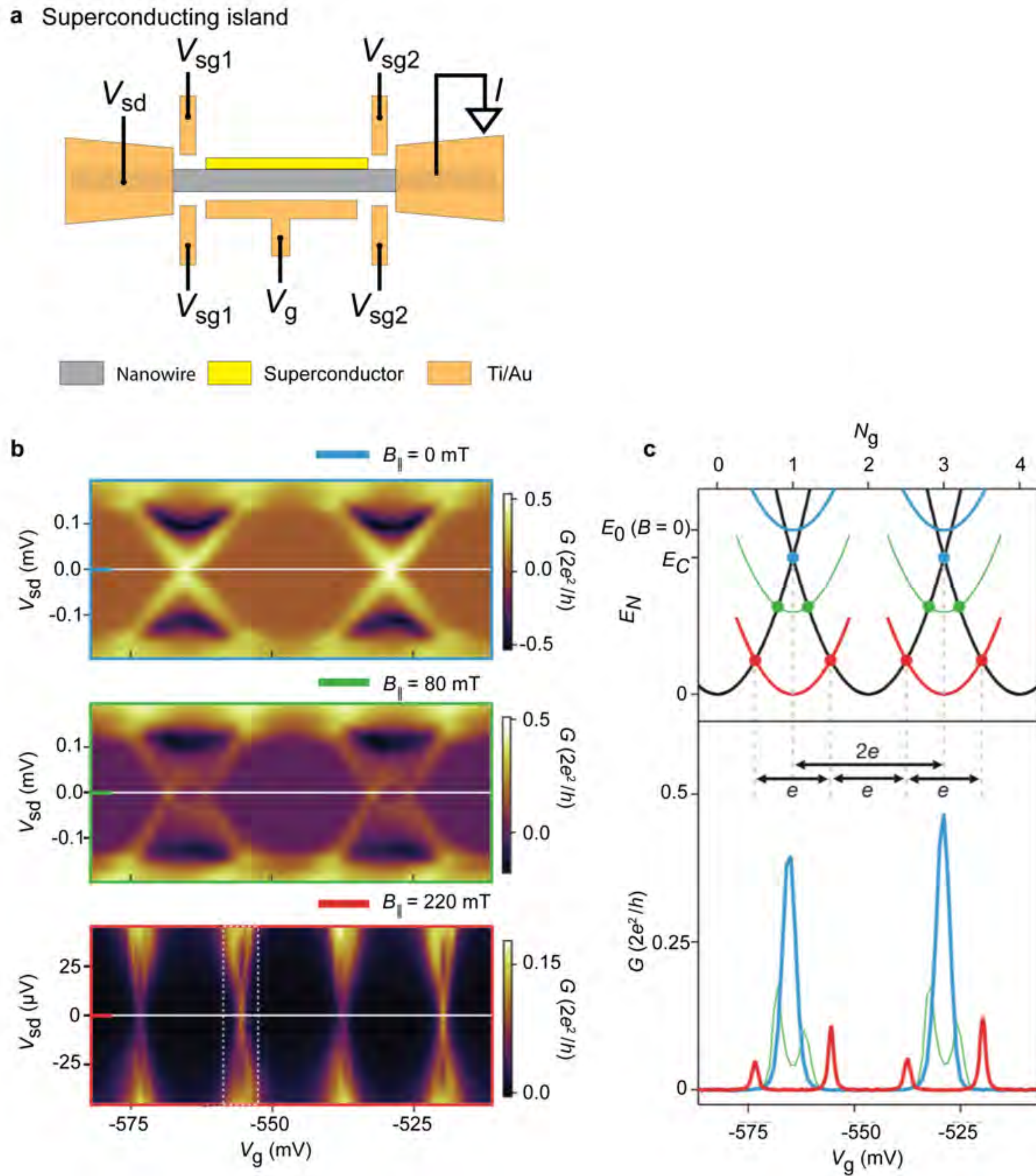

Figure 2.7: **Bias spectroscopy of superconducting island. a** Superconducting island device scheme. **b** Superconducting Al/InAs NW bias spectra at parallel magnetic fields $B_\parallel = 0$ mT (top), $B_\parallel = 80$ mT (middle) and $B_\parallel = 220$ mT showing Coulomb diamonds transitioning from $2e$- to $1e$ transport at $V_{\text{sd}} = 0$. **c** G vs. V_{g} line traces at $V_{\text{sd}} = 0$ at $B_\parallel = 0$ mT (blue), $B_\parallel = 80$ mT (green) and $B_\parallel = 220$ mT (red) **b-c** is adopted from Ref. [50].

Chapter 3

Results

In this chapter I present results of our work based on the development of a shadow mask platform for *in-situ* lithography of thin film segments on MBE grown semiconductor nanowires. The invention (Patent A,B) of the shadow mask platform enabled creation of several new hybrid material combinations for nanowire devices, previously unavailable due to lack of selective removal of thin-film segments, a requirement for obtaining functional device geometries. After introducing the shadow mask platform concept, features and how it was made, structural and electrical characterisation of the realised SU/SE hybrid nanowires are presented. Al/InAs nanowires are presented first due to their technological importance and are used to benchmark against the wide literature on etched epitaxial Al [35, 36, 37, 42, 43, 50, 51, 67, 68, 72] as well as implementation with other superconductors (In, V, Ta, Nb). All presented electrical data throughout the study is presented 'raw', without any corrections for switching events.

3.1 Shadow masks for *in-situ* hybrid nanowire growth

The contents of this section is largely based on the manuscript of Pub. B.

3.1.1 Platform concept and features

Figure 3.1 illustrates the platform overall concept and features. A (111)B-oriented InAs growth substrate is patterned with etched trenches and a series of silicon oxide (SiOx) 'bridges'. Nanowires are grown by MBE from Au catalyst particles, pre-positioned at the trench bottom with the desired lateral distance from the overhanging bridge(s). The bridges act as shadow masks in subsequent *in-situ* deposition of superconductors, normal metals, or dielectrics on the nanowires. The material is deposited from a fixed direction parallel to the trenches and inclined by an angle $\theta = 5^\circ - 45^\circ$ from the substrate surface. The situation is schematically shown in Figs 3.1**b,c**. The bridge design is thereby projected as a pattern in the deposited layer on each nanowire, effectively growing the desired device architecture, with independent choice of NW and coating material. To ensure a pristine interface, the sample remains under ultra-high vacuum ($< 10^{-8}$ Torr) between nanowire growth and superconductor deposition [35, 37, 39, 53, 73]. In the simplest, single deposition case, the superconductor coats 2 or 3 of the 6 nanowire facets (Schematic insert of Fig. 3.1**d** shows the NW cross section for 3 facet deposition) – i.e. a half-shell coating – except for regions shadowed by the bridge(s). This breaks the NW into a sequence of SU segments separated by bare SE. The length and number of segments are controlled by θ and the projected bridge design. The geometrical considerations are described in detail in Sec. 3.1.5; for now I will focus on outlining the broad features and possibilities. Figures 3.1**e-g** show scanning electron micrographs (SEMs) of bridge designs for producing the four most important hybrid device geometries with Al/InAs nanowires. Half-shadowed nanowires (Fig. 3.1**d**) are the design for tunnel spectroscopy characterisation of the (sub)gap properties of hybrids as described in Sec. 2.2.2. They are obtained by shadowing the entire lower section of the NW with a wide bridge. A single, narrow bridge (Fig. 3.1**e**) produces a gate-tunable Josephson junction[12], the component at the heart of gatemon/Andreev qubits[44, 45, 46, 47, 48, 49]. Double and triple bridges (Fig. 3.1**f,g**) produce hybrids with single[50, 67, 68] and double[51] Majorana island geometries, respectively, which, as introduced in Sec. 2.2.2, are the building blocks of topological quantum computation schemes[30, 66].

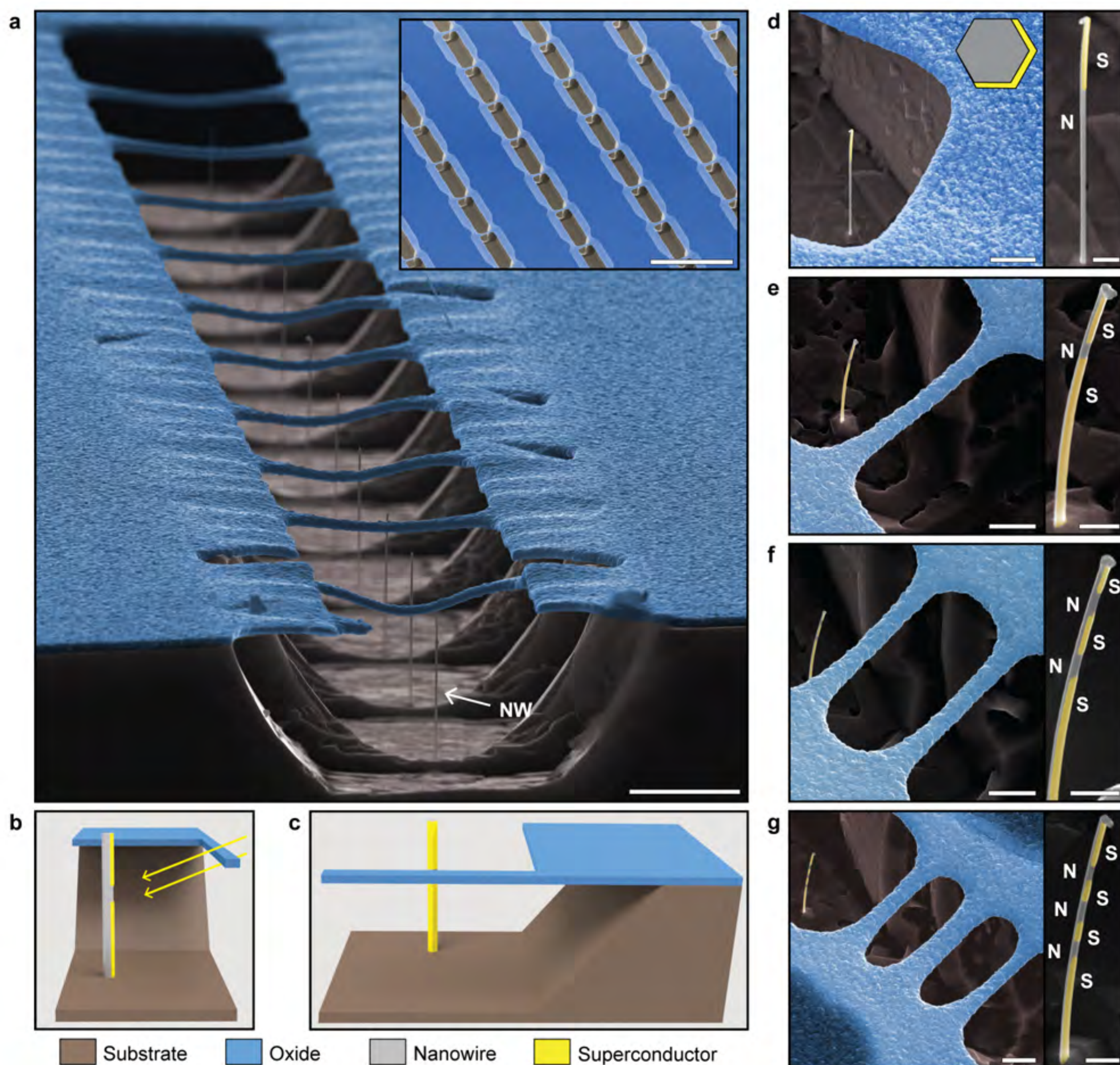

Figure 3.1: **Shadow lithography platform for hybrid nanowire growth. a** False colour scanning electron micrograph (SEM) of SiOx (blue) bridges spanning trenches in an InAs (grey) substrate. InAs nanowires (NW) are grown in proximity to the bridges, which act as a shadow mask. Inset: Overview SEM of bridge substrate before growth **b, c** Schematics viewed from **b** side and **c** the direction of superconductor (yellow) deposition. Direction of superconductor deposition is shown by the arrows in **b**. The bridge geometry is projected onto each nanowire to lithographically define the regions left uncoated during superconductor deposition. **d-h** False colour SEMs of as-grown nanowire hybrids with Al overlayer (yellow) with **d** tunnel probe, **e** Josephson junction, **f** island and **g** double island geometries. Scale bars represent **a** 5 μm (main) and 50 μm (inset) **d-g** 2 μm (left images) and 500 nm (right images)

3.1.2 Double-angle evaporation schemes

Having demonstrated the use of shadow lithography to realize the most important hybrid device geometries, further extensions and the flexibility of the method are introduced. Firstly, Fig. 3.2**a** illustrates how steep angle depositions under rotation enable *in-situ* conformal dielectric coatings protecting sensitive interfaces, contacts, and surfaces during subsequent device processing. Evaporation using θ_1 enables the oxide to mask the deposited material (e.g. a superconductor), while deposition at the steeper θ_2 circumvents the shadow mask. The insert of Fig. 3.2**a** shows a TEM of a half-shadowed Ta/InAs NW, coated by *in-situ* AlO_x.

A second extension, illustrated in Fig. 3.2**b**, employs consecutive shadow depositions from different angles to realize a complete *in-situ* junction with non-identical contact elements. Such structures thus produce both lateral and axial hybrid devices incorporating, e.g., normal metal, superconducting and/or magnetic elements with pristine epitaxial interfaces [74, 75]. Such double-angle deposition also enables JJ devices with arbitrarily short junction length as demonstrated in Fig. 3.2**c** for a vanadium based hybrid made by two depositions from different angles $\theta_1 = 16°$, $\theta_2 = 17°$. Conveniently, the semiconductor segment length l_{SE} depends not only the angles θ_1 and θ_2, but also the separation S between the bridge and nanowire. Increasing S from 9 μm to 17 μm reduced l_{SE} from $\sim$ 400 nm to $\sim$ 40 nm.

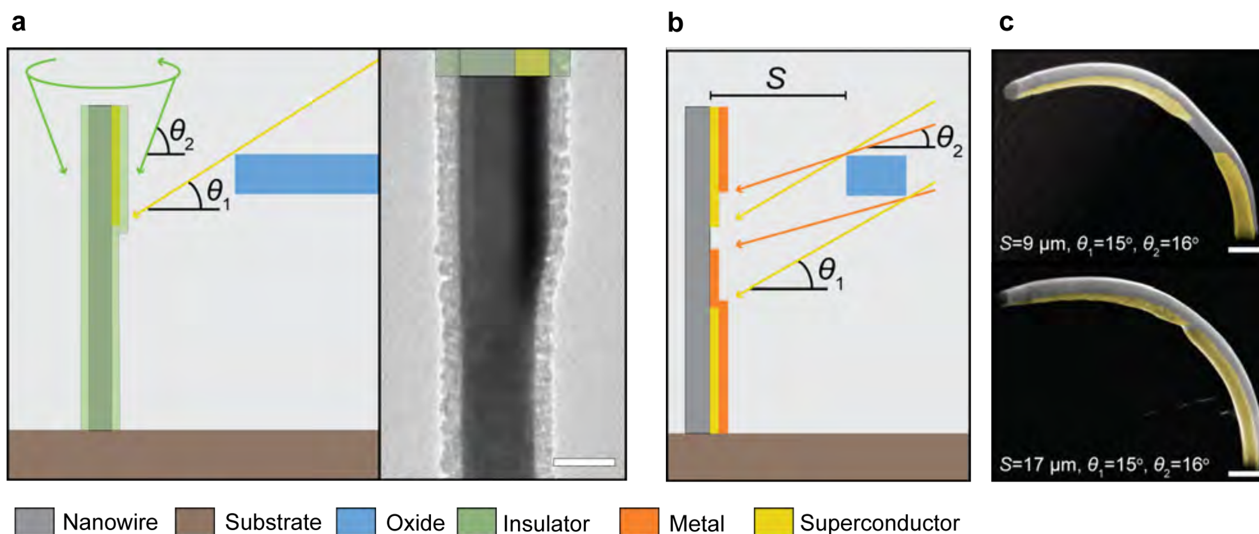

Figure 3.2: **Double angle evaporation schemes. a**, Schematic of two angle procedure for SU-NW junctions protected by an *in-situ* conformal insulator coating. Insert: Ta/InAs hybrid nanowire fully coated by AlO_x **b**, Contacting the nanowire with two different materials is possible using evaporation of the desired materials from two different angles, θ_1 and θ_2. The pictured example constitutes an *in-situ* formed tunnel spectroscopy device. **c**, Example of vanadium Josephson junctions realised by two-angle deposition, where junction length depends on θ_1, θ_2 and the nanowire-bridge separation, S. Scale bars represent **a**: 100 nm, **c**: 200 nm

3.1.3 Double-sided shadow masks

A third extension, demonstrated in Fig. 3.3, employs evaporations from opposite sides of the nanowire through shadow masks on either side. Hybrid nanowires with opposing segments of different materials are realised this way, as shown for Al (yellow) defined as an island, opposite two islands of AlMnOx tunnel junctions (orange) [76]. The bridge design determines in this case the number as well as the alignment of opposing segments. Segment alignment to the same vertical NW position on opposing NW facets between an Al island and an AlMn island is shown in the high magnification SEM in Fig. 3.3**b** and TEM in Fig. 3.3**c**.

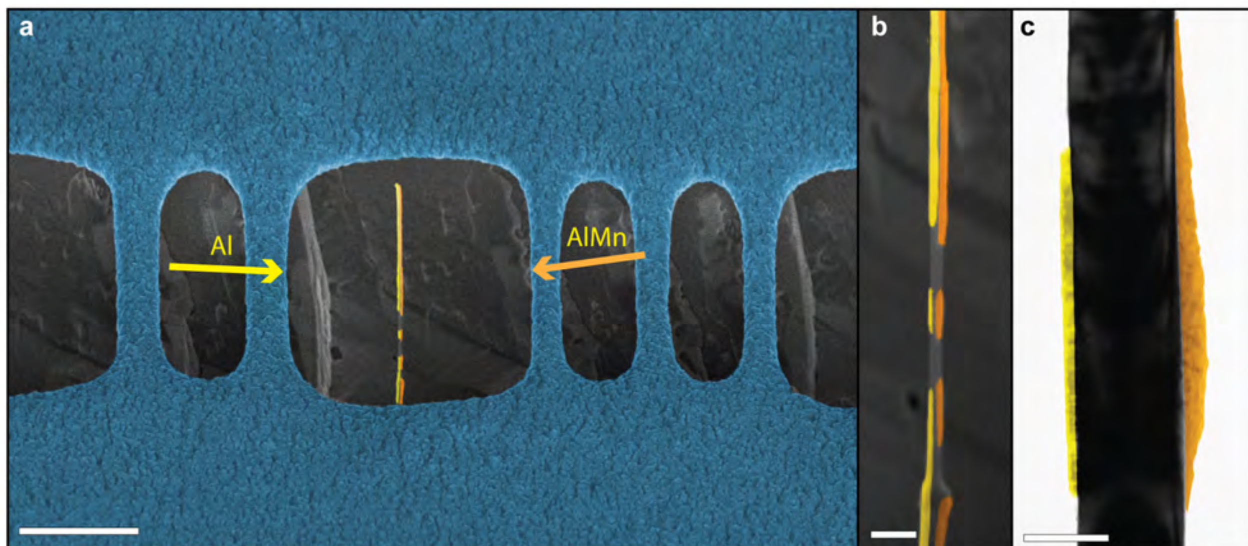

Figure 3.3: **Double-sided shadow mask lithography. a-b** False-color SEMs of a InAs nanowire grown between shadow masks of different designs. A double bridge geometry on the left side shadowed Al deposition (yellow) for a single island geometry, while a triple bridge geometry on the right side shadowed AlMn deposition (orange) for a double island geometry. **c** TEM of an InAs NW with Al (yellow) and AlMn (orange) coating opposing NW facets. Scale bars represent: **a**: 5 μm , **b**: 500 nm, **c**: 100 nm.

3.1.4 Full-shell shadow masks

A fourth feature of the shadow lithography platform is the generalisation to full-shell geometries, achieved by radially copying the bridge design and depositing the coating from corresponding angles around the nanowire. The shadow masks are aligned to face the 6 NW facets. Figure 3.4 shows a demonstration of full-shell Al/InAs geometries; tunnel-spectroscopy (Fig. 3.4**a**), JJ (Fig. 3.4**b**), single island (Fig. 3.4**c**), and double island (Fig. 3.4**d**). Positioning the NW in the centre of the circular mask is important to align the segments and junctions to the same vertical positions. An off-set of the NW from the centre position can thus create skewed junctions as seen in Fig 3.4**d**. Full-shell geometries have not been demonstrated by other shadow techniques using e.g. other nanowires [59]. Recent demonstrations of MBS[71] and anomalous metallic phases[77] in full-shell Al islands on InAs NWs motivates further development of shadow lithography in full-shell geometries. Like for the double-sided extension, deposition of different materials from the various directions and and using double-angle schemes further increases the possible functionality.

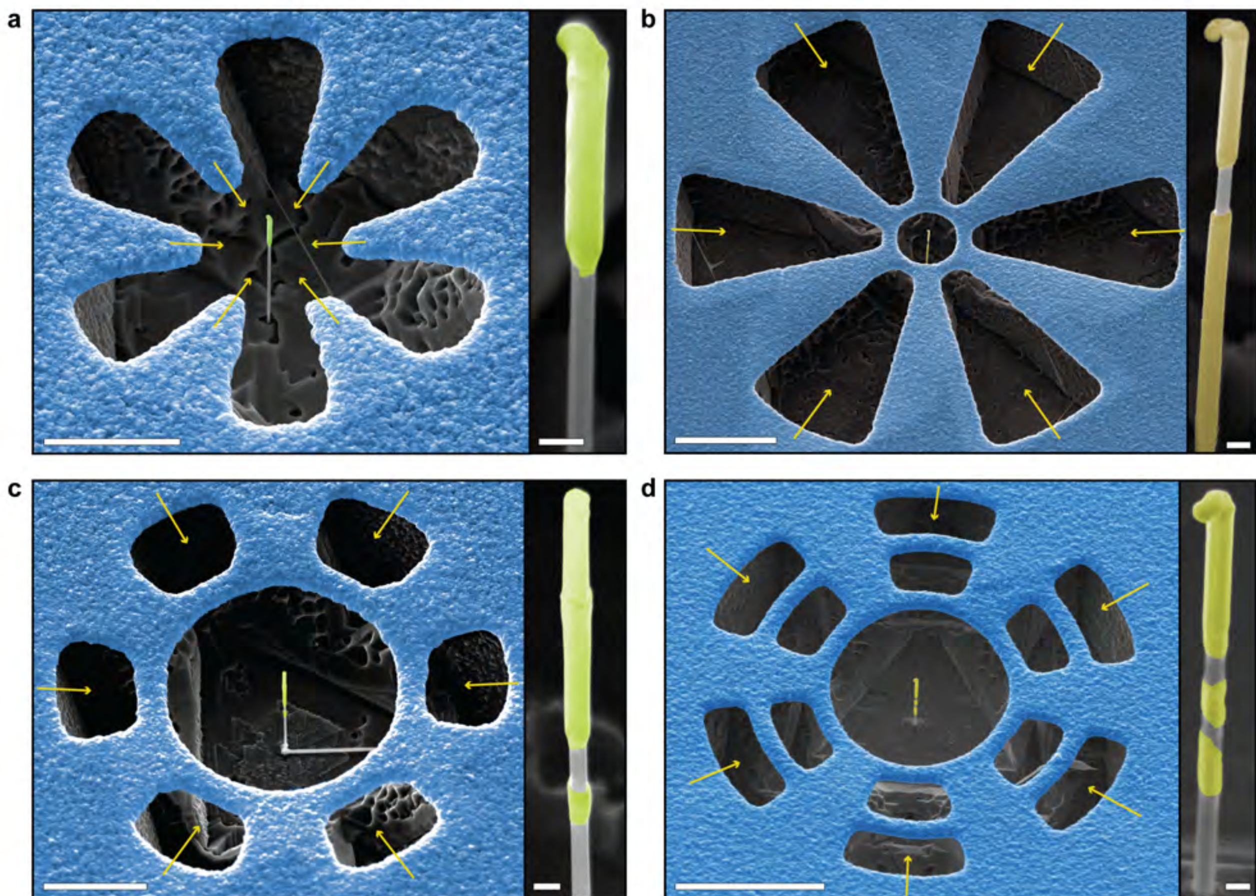

Figure 3.4: **Full shell shadow mask lithography a** False-color SEMs demonstrating a full-shell extension of the shadow mask lithography concept. Depositing from six different angles (arrows) matching a six-fold symmetric bridge structure (blue) aligned with the facets of the NW, yielded full-shell Al shells (yellow) in the four device geometries; **a** tunnel-spectroscopy, **b** Josephson junction, **c** single ring-shaped island, and **d** double ring-shaped island. Scale bars represent: **a,c**: 5 μm, **b,d**: 10 μm, inserts: 200 nm.

3.1.5 Geometrical considerations

The demonstrated flexibility of the platform relies on the tunability of mask dimensions, NW position and deposition angles, here modelled to calculate the geometrically expected segment and gap lengths. Figure 3.5**a** illustrates how bridge width, W, separation, S_{B}, SiOx thickness, t, and deposition angle, θ determine l_{SE} and l_{SU}, the length of the semiconducting (i.e. shadowed) and superconducting (i.e. not shadowed) segments, respectively. The equations for the segment lengths read:

$$l_{\mathrm{SE}} = W\tan(\theta) + t \tag{3.1}$$

$$l_{\mathrm{SU}} = S_{\mathrm{B}}\tan(\theta) - t \tag{3.2}$$

Given θ and t are fixed for each substrate/deposition, W and S_{B} are the free variables used to define l_{SE} and l_{SU}.

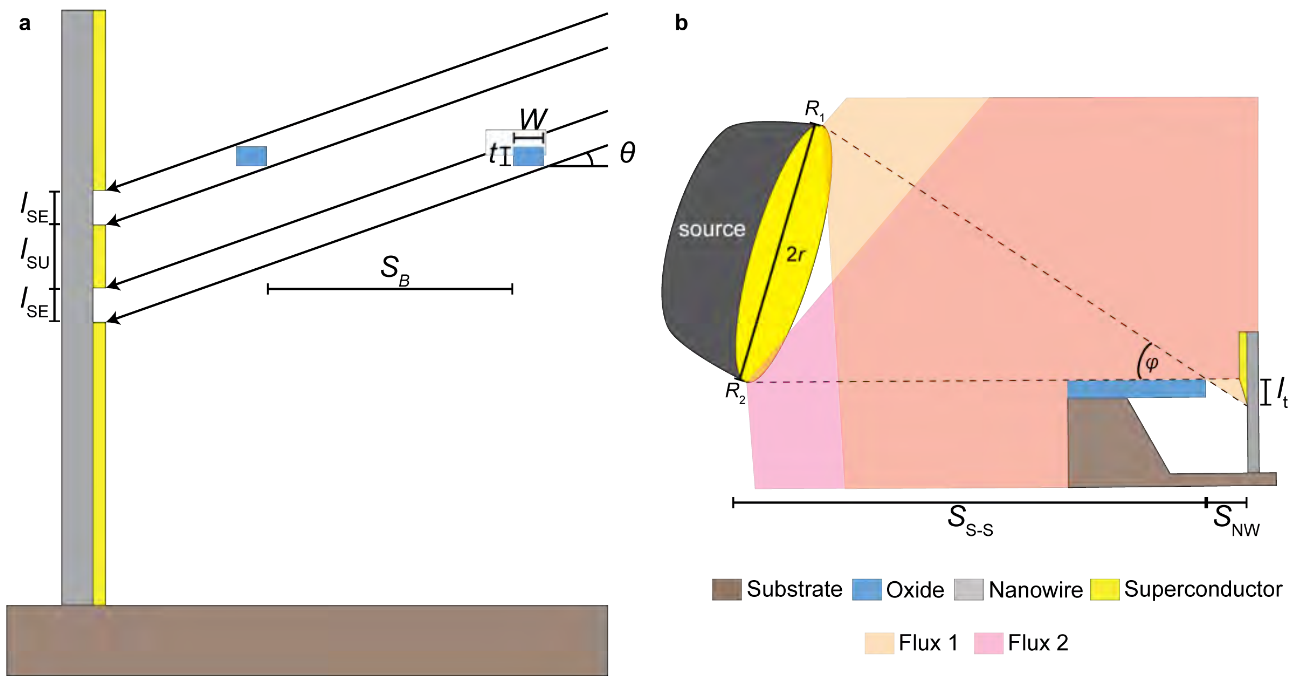

Figure 3.5: **Geometrical schematics.** Schematics illustrating geometric considerations in shadow lithography. **a** Deposition angle θ and bridge dimensions determine semiconductor and superconductor segment lengths according to $l_{\mathrm{SE}} = W\tan(\theta) + t$ and $l_{\mathrm{SU}} = S_{\mathrm{B}}\tan(\theta) - t$. **b** The finite size of the deposition source is expected to result in SU tails with length $l_{\mathrm{t}} \sim 2rS_{\mathrm{NW}}/S_{\mathrm{S-S}}$. In practice, material diffusion also impacts this parameter.

Additional factors that contribute to l_{SE} and l_{SU} were determined experimentally. Firstly, material grew on the bridges during semiconductor growth, which depended on the surface growth selectivity at the required growth conditions (temperature, time, flux, etc.). This increased W and t, thereby increasing l_{SE} and decreasing l_{SU}.

Secondly, the finite radius of the deposition source, r, influenced the abruptness and morphology of the SU tails as depicted in Fig. 3.5**b**. Each point of the deposition source generated material flux over a wide, solid angle. The orange and pink coloured areas in Fig. 3.5**b** represent the material flux originating from points $R_{1,2}$ at either extremity of the source. The shadow mask causes different terminating edges for material originating

from each position, indicated by the dashed lines. This effect, taking into account all points across the source, is a gradual decrease in deposited material thickness across the tail, with length l_{t}. For small deposition angle θ, $l_{\mathrm{t}} \sim 2rS_{\mathrm{NW}}/S_{\mathrm{S-S}}$ where S_{NW} is the distance between the nanowire and oxide barrier, and $S_{\mathrm{S-S}}$ is the source-substrate separation. Additionally, the non-linear dependence of flux on r – arising since the e-beam is focussed at the center of the source – generates a non-linear thickness profile in the tail. The dimensions of our evaporation chamber and substrates yields estimated $l_{\mathrm{t}} = 100 - 200$ nm.

Thirdly and finally, cluster diffusion played an increased role for materials with a lower heat of vaporisation, such as Al. Materials with higher heat of vaporisation, like Ta and Nb, have lowered mobility on the InAs surface and therefore the tail profile of the deposited material is determined largely by the adatom flux gradient due to the finite source size and shadow geometry. Adatoms for other materials, such as Al, remain mobile, and may form a crystalline, epitaxial film that does not have a geometrically defined l_{t}. By measuring the effect of all three of these factors it was possible to accurately estimate and predict the resultant l_{SE} and l_{SU} for the various shadow mask designs.

3.1.6 Platform fabrication

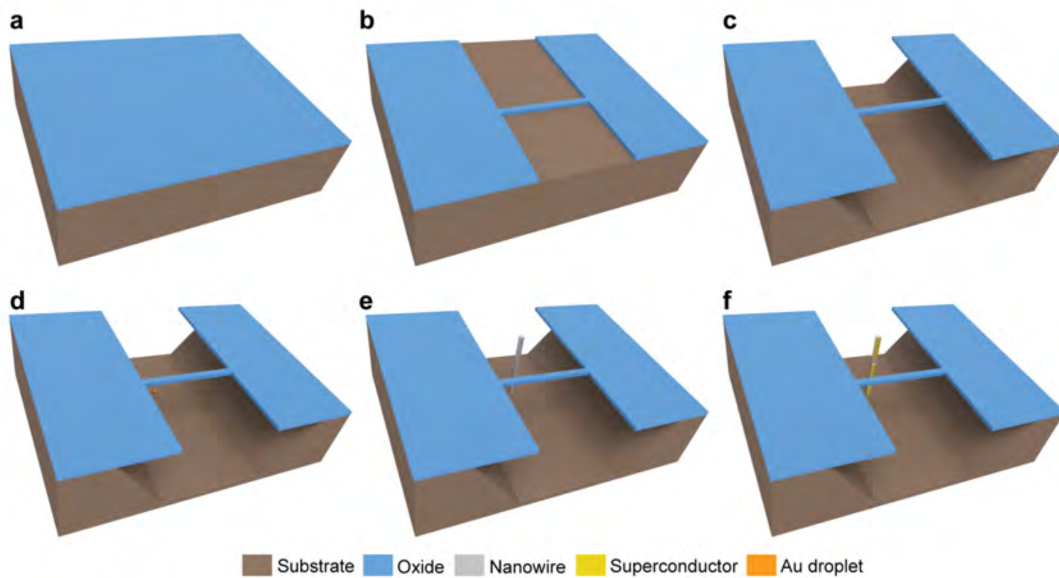

Figure 3.6: **Platform processing.** Each step is described is the main text.

Figures 3.6**a-f** illustrates the overall platform fabrication process. A detailed recipe is found in Appendix 5.1. An epi-ready InAs (111)B oriented wafer is capped with 150 nm of SiOx by plasma-enhanced chemical vapour deposition (Fig. 3.6**b**). Photoresist (AZ1505) is spun onto this surface, and a custom shadow mask pattern exposed using a Heidelberg μPG501 LED writer[1]. After resist development and a soft post-bake, buffered hydroflouric acid (HBF) (6% HF) is used to etch the SiOx (Fig. 3.6**c**). This way, bridge widths down to $W = 400$ nm – less than the optical lithography resolution limit – can be obtained by controlled overetching. The resist is then removed, and the exposed InAs is etched using a citric acid, phosphoric acid, hydrogen peroxide, H_2O solution (Fig. 3.6**d**). The solution anisotropically etches the InAs crystal, leaving (111) surfaces in the bottom

[1] Electron beam lithography (EBL) is also suitable if finer features are required

of trenches. Importantly, InAs beneath defined SiOx strips is removed, leaving the strips as suspended bridges across the trench. After resist removal, the entire growth wafer is covered in the desired shadow lithography patterns, as shown in Fig. 3.7. Subsequently, gold catalyst particles for InAs nanowire growth are defined by means of electron beam lithography (EBL). First, a conformal 15 nm thick Al_2O_3 layer is deposited by atomic layer deposition (ALD). This layer is optional – and therefore not illustrated in the figure – but was included to align the process more closely to our standard MBE process in two ways. Firstly, a short HF cleaning step is performed immediately before loading; the slow etch rate of Al_2O_3 compared to SiOx protects the bridges during this step. Secondly, our highest quality nanowires were grown using Al_2O_3-masked substrates with EBL-defined Au catalyst particles. For subsequent EBL in the etched trenches, a stack of PMMA A4 or A4.5 (lower layer) and copolymer EL13 (top layer) is spun. EBL is used to define $\sim$ 100 nm diameter circular openings in the resist proximal to each bridge ensemble. Transene$^{\text{TM}}$Aluminum etchant D is then used to remove the Al_2O_3, and buffered hydroflouric acid to clean the exposed InAs surface. Immediately after BHF cleaning, the sample is loaded in a e-beam evaporation chamber and 10-15 nm Au is deposited, leaving catalyst particles after lift off (Fig. 3.6**e**). The purpose of the copolymer EL13 is to coat the bridges during Au deposition and prevent Au sticking to them; the exposed regions in the copolymer EL13 are much wider than in the PMMA after development and therefore do not impact the definition of the catalyst particles.

The substrate is then loaded into the MBE chamber, and nanowires are grown by molecular beam epitaxy as described in the next section (3.1.7) (Fig. 3.6**f**). Finally, the substrate is transferred under ultra high vacuum to the general purpose metal evaporation chamber, with freely rotatable sample holder. The sample holder can be cooled to approx -150°C using liquid nitrogen or heated. The superconductor layers (Al, In, V, Ta, Nb) were deposited using e-beam evaporation at a fixed angle such that the bridges produced shadowed regions on the desired section(s) of the nanowires (Fig. 3.6**g**). After deposition, the samples were left to warm/cool to room temperature under vacuum before unloading.

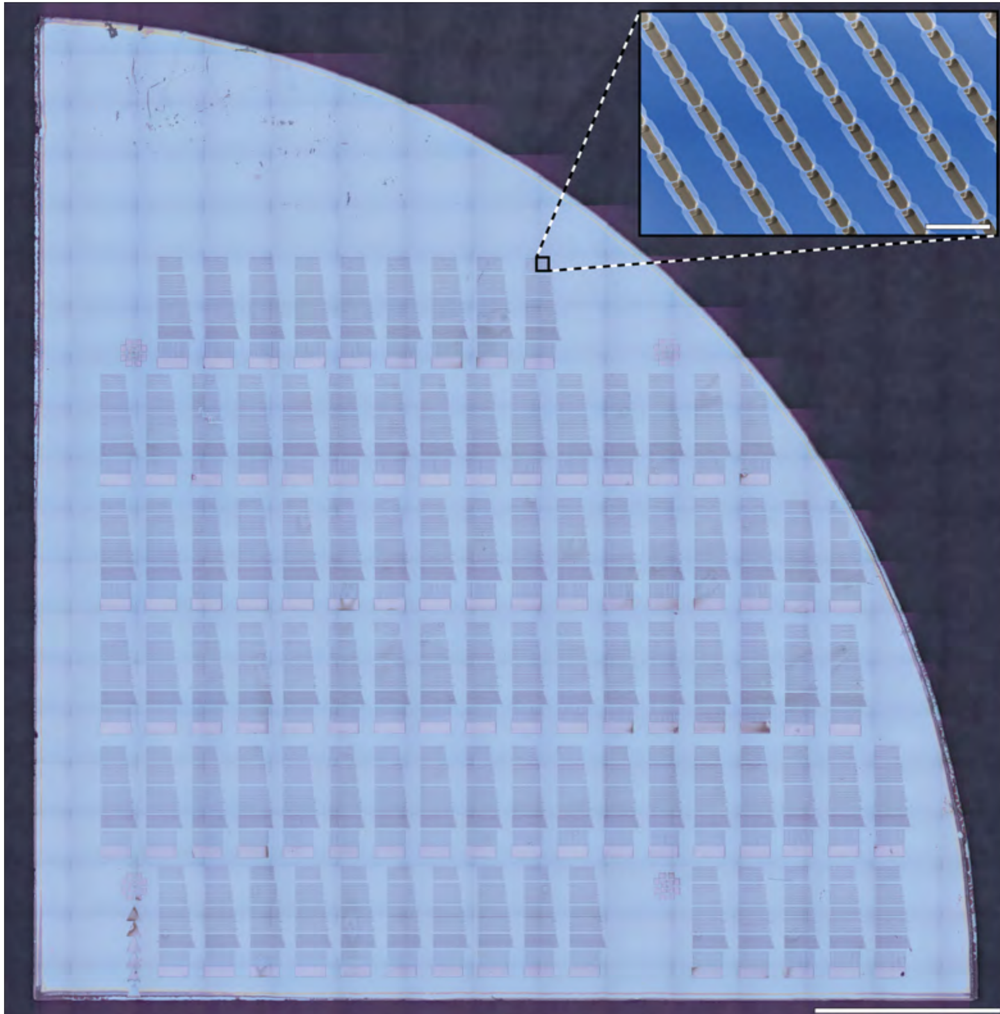

Figure 3.7: **Shadow mask lithography on wafer scale.** Overview image of finished substrate with shadow mask. A (111)B-oriented InAs growth substrate is patterned with etched trenches and a series of silicon oxide (SiOx) 'bridges'. Wafer scale patterned, device-ready hybrids are realized simultaneously in all the different geometries. Scale bars on main image and inset represent 5 mm and $50\ \mu$m, respectively.

3.1.7 Nanowire growth schemes

Crystalline wurtzite InAs NWs were grown *via* the Au-catalyst assisted vapour-liquid-solid mechanism [35, 78] from the etched InAs (111)B surfaces in a solid-source Varian GEN-II MBE, using two different growth schemes. One scheme involved *in-situ* MBE deposition of a Au thin film and annealing to obtain Au catalyst nanoparticles on the surface. The other scheme used the Au nanoparticle catalysts defined and positioned by EBL in the platform fabrication. For future reference of which growth scheme was used for the individual hybrid nanowire growth, they will be referenced as either "*in-situ* Au" or "EBL Au". The substrate temperature, T_{S}, refers to the temperature measured by the thermocouple.

Nanowire growth from Au catalysts defined by *in-situ* deposition and annealing

Like shown in Fig.3.8, the *in-situ* Au scheme was used for samples featuring lithographically defined etched trenches that during SU deposition at an angle $\theta \sim 25°$ enabled shadowing the bottom-half of the NWs. The trenches were etched using the same chemical solution as introduced for the shadow mask platform (Sec. 3.1.6). After loading a trench-patterned InAs (111)B sample into the MBE, Au was deposited *in-situ* at a thermocouple temperature, T_{S}, of 605°C producing Au particles with random diameter (approx. 100 nm) and pitch (approx. 5 μm) throughout the entire substrate. During nanowire growth, the substrate temperature was kept constant at $T_{\mathrm{S}} = 445$°C with a calibrated $\mathrm{As_2/In}$ flux ratio of 15 for 30 minutes and with a projected planar growth rate of ~0.5 ML/s. These growth conditions yielded nanowires grown along the $[111]$ direction with typical lengths $5-8$ μm and diameters $\sim 80-100$ nm (3.8**a**). The substrates were then transferred to the metallisation chamber and SU was deposited at an angle θ, coating the upper-half of the NWs in the trenches (3.8**b**). NWs in the trenches further than $\sim$ 5 μm from the masking edge were not shadowed. After SU deposition, the samples were left to warm/cool to room temperature under vacuum before unloading.

Nanowire growth from Au catalysts defined by EBL

In this growth scheme, InAs nanowires were grown from pre-positioned EBL defined Au nanoparticles positioned in the trenches of the shadow mask platform like shown in Figs. 3.1,3.3 and 3.4. Using a two-step protocol nanowires were first grown vertically along the [111] direction, using $\mathrm{As_4}$ cracker temperature 500°C, substrate thermocouple temperature of 447°C and V/III flux ratio $\sim$ 10. The low V/III flux ratio combined with $\mathrm{As_4}$-based growth produced a lower stacking fault density and higher nucleation probability compared to the "*in-situ* Au" scheme. A growth time of 80 mins resulted in $5-8$ μm-long nanowires. The second step involved growth at reduced substrate thermocouple temperature (350°C) and increased As cracker temperature (800°C) for 10 minutes. These conditions promoted radial overgrowth – concomitant with approx. 100–300 nm of continued axial growth – which was found to result in formation of flatter nanowire facets. Flat facets are beneficial for subsequent superconductor/metal deposition. The resulting nanowire diameters were around $80-100$ nm.

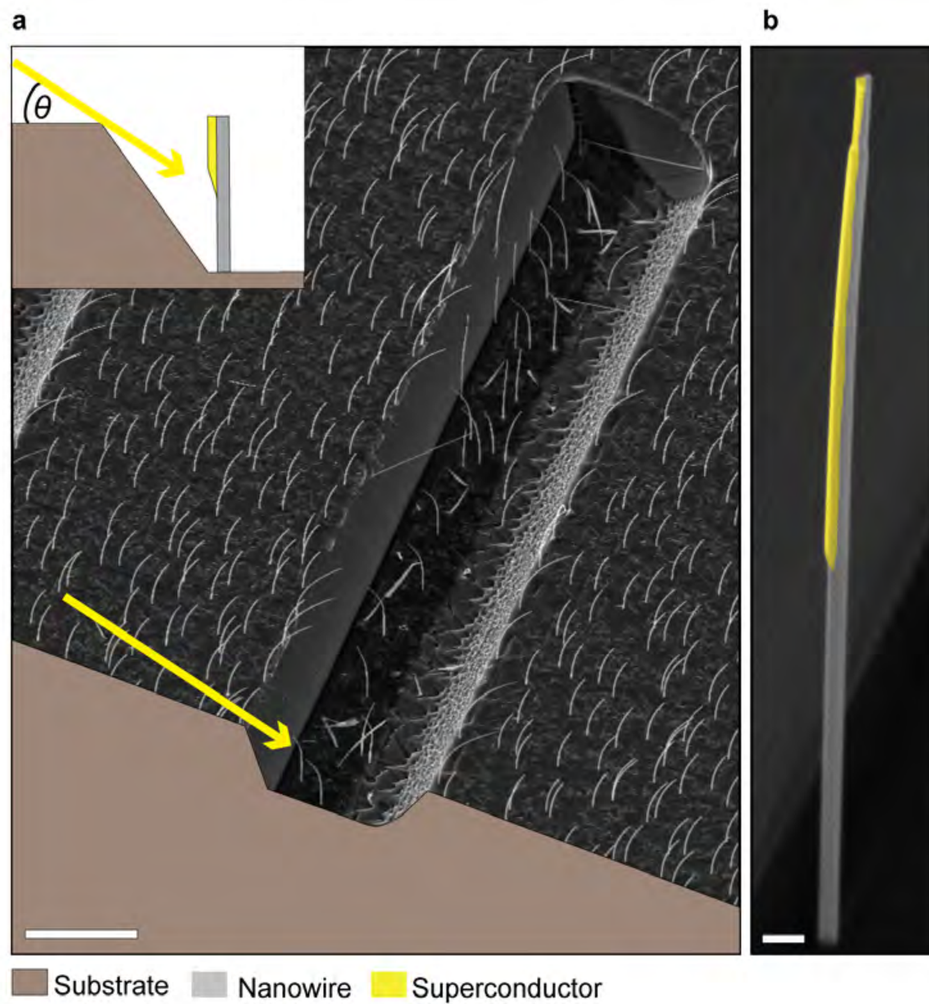

Figure 3.8: **Nanowire growth using *in-situ* Au deposition and shadow masking using trenches.** **a** SEM of as-grown Ta/InAs NWs on a (111)B-oriented InAs growth substrate with etched trenches. Insert: Schematic of how the trench was used to shadow the lower NW segment by deposition at an angle θ. **b** False-color SEM of a NW grown in a trench where only the top half was coated by Ta (yellow) during deposition. Scale bars represent: **a**: 10 μm, **b**: 200 nm

3.1.8 Chemical Beam Epitaxy integration

An alternative to MBE for the growth of InAs nanowires is to replace the molecular beam by metalorganic precursors such as trimethylindium (TMIn), tert-butylarsine (TBAs) and tert-butylphosphine (TBP), utilised in chemical beam epitaxy (CBE) systems. CBE enables the ability to switch abruptly between growing e.g. InAs and InP axial segments, which can be used to define tunnel barriers and quantum dots within the nanowire [79, 80]. Combining the shadow mask lithography platform with axially grown heterostructures, such as InAs/InP/InAs, thus has the potential of compactly integrating tunnel junctions in nanowire along with radially deposited thin film segments. During my change of scientific environment in Pisa with Lucia Sorba, CBE NW growths were conducted in a Riber C-21 using shadow mask growth substrates prepared at QDev. Figure 3.9 shows a false-colored SEM of a CBE grown InAs NW by two shadow mask bridges. The nanowires were grown with a substrate thermocouple temperature of $T_\mathrm{S} = 420°\mathrm{C}$ for 75 min with a TMIn/TBAs line pressures of 0.6/2.4 Torr.

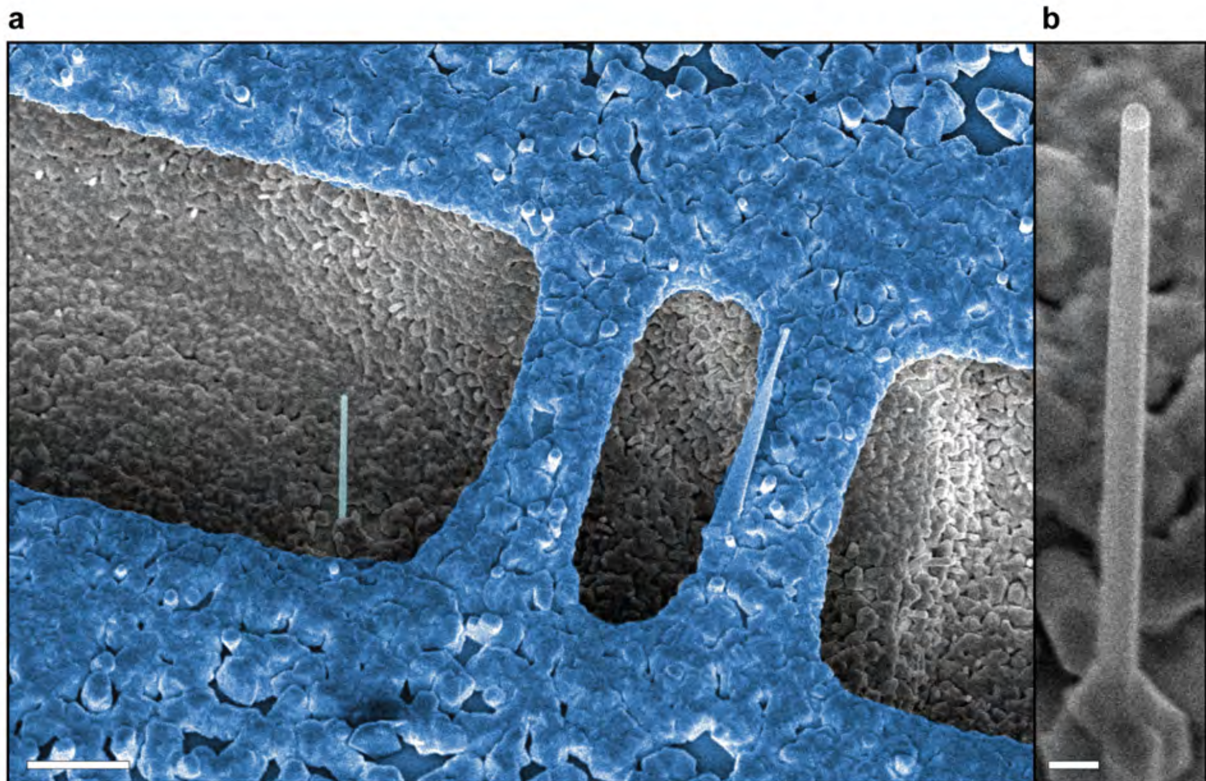

Figure 3.9: **Chemical Beam Epitaxy InAs growth integration. a** False-colored SEM showing a CBE grown InAs NW by two SiOx shadow mask bridges. **b** Higher magnification SEM showing that the NW grew uniformly until tapering in the top segment. Like for the MBE growths, surface overgrowth was covering the shadow masks and trenches. Scale bars: **a**: 2 μm, **b**: 200 nm.

3.1.9 Conclusions and outlook

This section demonstrated the growth several different SU segment geometries in InAs NWs with the *in-situ* shadow mask lithography technique. One of the key advantages of the technique was to realise wafer scale of patterned, device-ready hybrids simultaneously in different geometries by tuning the design parameters. While the described fabrication process for the shadow mask lithography platform was designed specifically for InAs nanowire growth, using other materials and etchants would enable the growth of different semiconductors. Growth of InSb is trivially related, since growth of a short InAs stem typically precedes InSb nanowire growth[81]. A method for producing SiN bridge structures on silicon substrates has been presented in Ref. [82]. This would allow the platform to be applied to growth of many nanowire materials, including silicon, germanium[83], GaAs[84], and GaN[85]. Similarly, the etches used in Ref. [59] for InP coated with SiOx would produce bridges on these substrates with the appropriate lithography, enabling phosphide- and antimonide-based nanowire growth. Naturally, the semiconductor growth should be done in a vacuum system where deposition of the superconductor is possible without breaking vacuum after growth. Alternatively, hydrogen cleaning[86] immediately before superconductor deposition appears sufficient to generate a pristine surface and hard superconducting gap[59]. Exploring this option for materials beyond InAs and InSb[59, 86] would be very interesting.

3.2 Al/InAs hybrid nanowires

The contents of this section is largely based on the manuscript of Pub. B.

In previous studies of *in-situ* grown Al/InAs hybrids, aluminium was either epitaxially grown with a solid-source MBE cell on wurtzite InAs NWs grown from InAs (111)B wafers [35] or e-beam evaporated onto mix-phase (ZB/WZ) InAs NWs grown from Si substrates [53]. In Ref. [53] it was found that no epitaxial growth of Al on InAs was present for NWs showing polytypism. Rather, a polycrystalline film with grain sizes of several hundred nanometers formed.

In this study, Al was deposited by e-beam evaporation using a sample holder with free rotation and tilt, improving the flexibility of the shadow lithography platform. Furthermore, the improved cooling capabilities using liquid nitrogen was important for Al as the lower temperature decreases the surface diffusion length, critical to avoid small Al islands forming inside the shadowed segment. Structural characterisation of Al evaporated *in-situ* onto wurtzite InAs NWs using e-beam evaporation had not been reported, motivating a study of Al films produced with the shadow mask platform. Low temperature transport experiments on Al/InAs hybrids were performed to demonstrate the expected improved device performance, reproducibility and stability offered by shadow-patterned hybrids and benchmark them against the wide literature on etched epitaxial Al [35, 36, 37, 42, 43, 50, 51, 67, 68, 72].

3.2.1 Sample descriptions

Three substrates (A1-A3) featuring single-sided (A1), double-sided (A2) and full-shell (A3) shadow masks were used for InAs NW growth using the ”EBL Au” scheme described in Sec. 3.1.7. After NW growth the samples were transferred *in-situ* to the metal deposition chamber and cooled to a substrate temperature of $-150°$C. Aluminium was then evaporated with $\theta = 10°$ at a rate of 1 Å/s. Samples A1 and A2 had 10 nm Al evaporated along the $[11\bar{2}]$ wafer direction, parallel to the etched trenches of the SiOx shadow mask. Sample A3 had six consecutive 10 nm evaporations incremented by a substrate rotation of 60° starting from the $[11\bar{2}]$ direction to utilize the six-fold shadow mask designs for full-shell lithography. An overview of the sample deposition parameters is shown in Table 3.1. The resulting NW growths and control of number and position of Al segments from shadow masking were already shown and described while presenting the platform in Figs.3.1(A1), 3.3 (A2) and 3.4 (A3).

	T_{S} (°C)	t_{Al} (nm)
A1 - single-sided masks	-150	10 (3-facet half shell)
A2 - double-sided masks	-150	10 (3-facet half shell)
A3 - full-shell masks	-150	30 (full shell)

Table 3.1: **Al/InAs samples.** Overview of Al deposition temperatures T_{S} and thicknesses t_{Al} for the three InAs nanowire growths in shadow mask substrates A1-A3. The Al film thicknesses were measured from TEMs.

3.2.2 Structural characterisation

For the structural characterisation, Al/InAs hybrids from (A1) featuring the NS geometry (Fig. 3.10**a,b**) were characterised by TEM as shown in Fig. 3.10**c-f**. Fig. 3.10**c** shows a low magnification bright field TEM of the

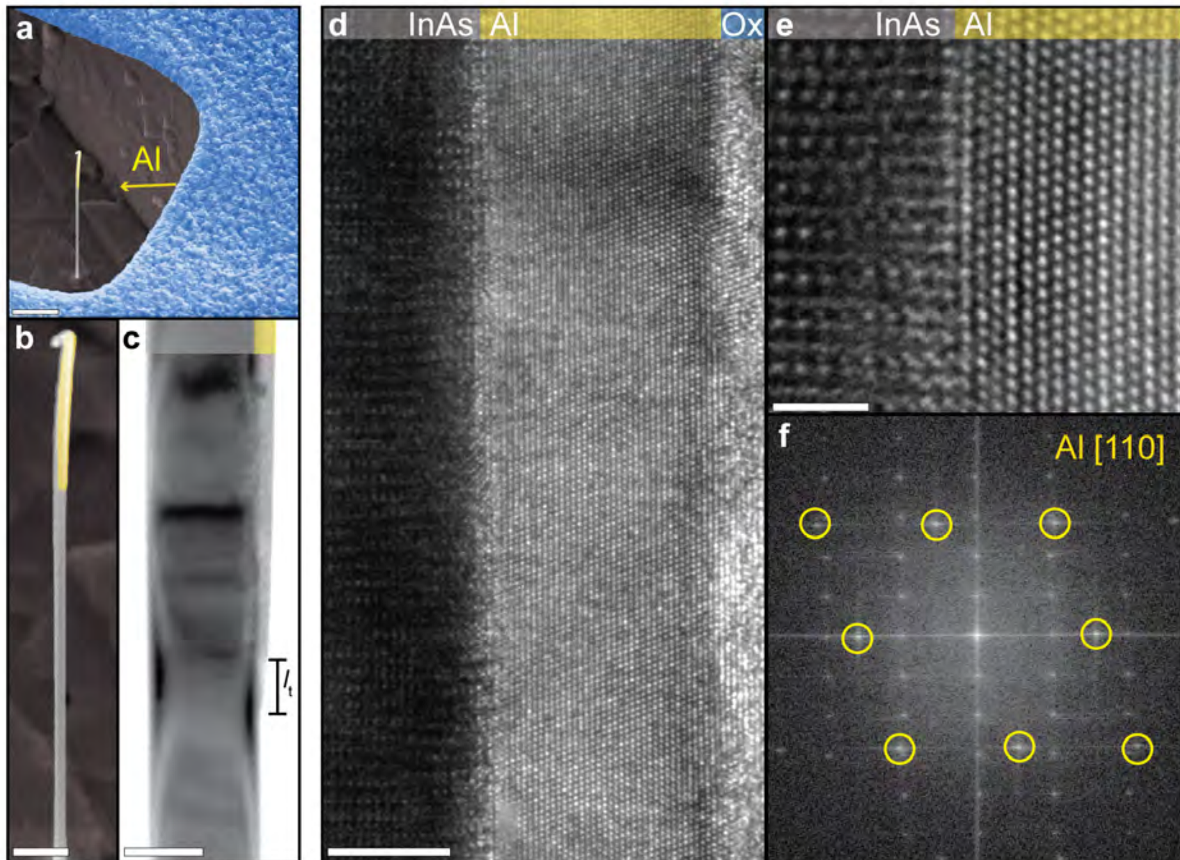

Figure 3.10: **Electron microscopy of Al/InAs hybrids. a-b** False-color SEMs of an as-grown Al/InAs hybrid nanowire by a wide SiOx bridge in the growth substrate (A1). The yellow arrow indicate the direction of Al evaporation. **c** Low magnification TEM of an Al/InAs hybrid nanowire by the shell termination facilitated by the shadow mask. **d-e** HRTEM of the Al/InAs interface. The InAs is aligned to the $[2\bar{1}\bar{1}0]$ zone axis to feature the nanowire facets parallel to the viewing direction. **f** FFT of **d** showing that single-crystalline FCC Al is grown on the facets featuring the [110] zone axis and a [111] out-of-plane direction. Scale bars: **a**: 2 μm **b**: 500 nm **c**: 100 nm, **d**: 5 nm **e**: 1 nm.

transition region between an Al-coated and uncoated segment of the nanowire. The length of the transition from full film thickness to film termination, l_t, was $\sim 10 - 60$ nm for the Al/InAs hybrids. As discussed in Sec. 3.1.5, l_t is the result of a combination of the finite size effect of the evaporation source as well as material surface mobility. The surface mobility for Al was high enough for adatoms arriving at the junction to be collected by the nearby grain even at -150°C. The InAs NWs were pure WZ phase and so the observed contrast contours and fringes in the nanowire likely arise from a combination of bending contours and fringes due to thickness variations [60]. HRTEMs (Figs. 3.10**d,e**) revealed the crystalline nature of the Al film. In Fig. 3.10**d**, lattice fringes in the Al film showed single crystalline grains in the full film thickness until termination by a surface oxide layer. Measurements of interplanar distances and angles between the lattice fringes confirmed that Al crystallised in the face-centred cubic (FCC) phase featuring the [110] zone axis transverse to the NW facets and a [111] out-of-plane orientation. A Fast-Fourier Transformation (FFT) (Fig. 3.10**f**) of Fig. 3.10**d** shows the plane alignment of Al (111) planes and the NW $\{1\bar{1}00\}$ facet planes. This matched the previously reported epitaxial arrangement of MBE-grown Al/InAs hybrids [35]. Confirming the epitaxy ensured that the shadow-patterned Al/InAs hybrids structurally would have the same starting point as the etched epitaxial Al/InAs.

3.2.3 Electrical characterisation

Tunnel-spectroscopy

Five devices (DA1-DA5), similar to that shown for D5 in Fig. 3.11**a** were fabricated for tunnel-spectroscopy measurements (Sec. 2.2.2). Bias spectra from all five devices (Fig. 3.11**b-f**) exhibited a hard superconducting gap with coherence peaks at $V_{\rm sd} = \pm\Delta/e = \pm 0.20 - 0.25$ mV, highlighted in Fig. 3.11**f** by the line trace at $V_{\rm g} = -9.195$ V. All bias spectra featured multiple gate-dependent sub-gap peaks below the coherence peaks at Δ, reproducing ABS as have been observed in previous experiments involving a quantum dot formed between a normal and superconducting segment [56, 65, 87, 88]. Figure 3.11**g** shows logarithmic line traces of normalised conductance $G/G_{\rm N}$ vs $V_{\rm sd}$ (where $G_{\rm N}$ is the out-of-gap conductance $G(V_{\rm sd} = -0.4$ mV)) at fixed gate voltages indicated by white lines in Fig. 3.11**b-f**. The traces were vertically offset by two decades for clarity. The gap hardness, $G_{\rm N}/G_{\rm S}$ (where $G_{\rm S} = G(V_{\rm sd} = 0$ mV)), was approx. 50-100 in the studied devices which compares favourably to reported hardness for etched epitaxial Al/InAs [36].

The properties of the tunnel barrier affect $G_{\rm N}/G_{\rm S}$ [36, 56, 89] meaning that the hardness value varies as a function of $V_{\rm g}$. We therefore measured $G_{\rm N}/G_{\rm S}$ for D5 over the entire presented $V_{\rm g}$ range in order to ascertain the range where the reported hardness is valid. For DA5, $G_{\rm S}(G_{\rm N})$ was averaged from 2000(100) individual measurements at each $V_{\rm g}$ as shown in Fig. 3.12**a**. At $V_{\rm g} = -10$ V, the device was in deep pinch-off, providing a measurement of the noise floor $\sim 10^{-4}$ 2e^2/h. The gap hardness, $G_{\rm N}/G_{\rm S}$, vs. $V_{\rm g}$ is plotted in Fig. 3.12**c**, having subtracted the noise floor from $G_{\rm N}$ and $G_{\rm S}$. For most of the studied range, $G_{\rm N}/G_{\rm S} = 50 - 110$ (highlighted by dashed lines), with peaks occurring that are likely associated with variations in properties of the tunnel barrier.

Figure 3.13 shows the gap evolution in parallel magnetic field, $B_{\parallel}$, with $V_{\rm g}$ fixed at the position of the line trace in D5 of Fig. 3.11. The gap closes at critical field $B_{\rm C} = 2$ T; the high value is enabled by the thin, flat, epitaxial film, as seen previously [43]. Coalescing bound states which stick to zero energy for $B_{\parallel} > 1.3$ T are also observed – highlighted by the line trace taken with $B_{\parallel} = 1.5$ T – resembling the topological MBS reported previously [21, 43]. As discussed already in Sec. 2.2.2, coalescing ABS can also be pinned exponentially close to zero energy, thus mimicking a topological zero-energy MBS [65, 70]. The sub-gap states driven towards zero-energy with increasing B had an effective g-factor = 6.5, consistent with previous results [72]. High $B_{\parallel}$ is

an important prerequisite for topological devices, since the magnetic field otherwise will turn the whole system normal before any states turn topological. The shadow-patterned Al hybrids thus maintained all the qualities needed to study topological superconductivity, with the additional advantage of high device yield (5 of 5), unlike etched devices where some usually do not show superconductivity [90]

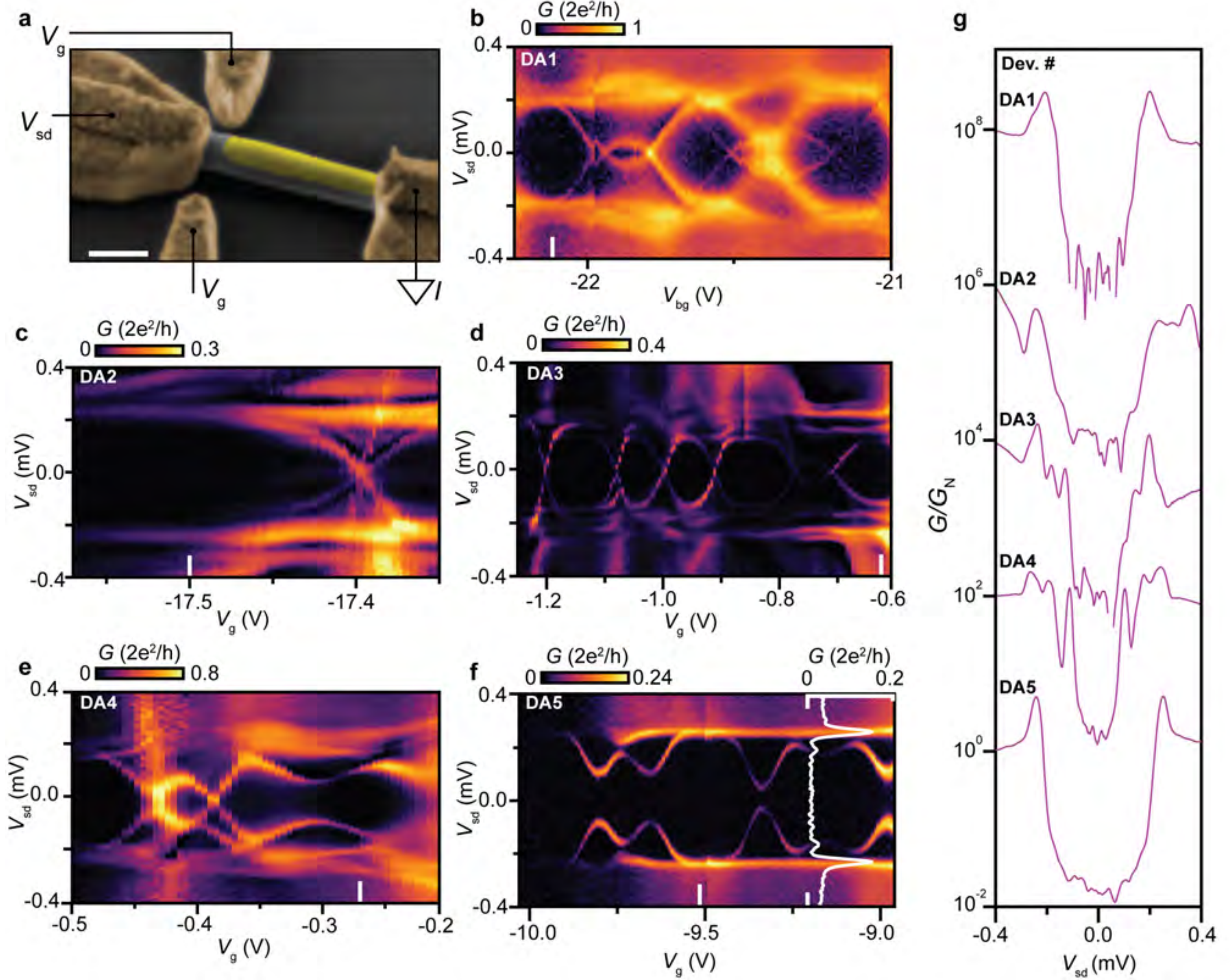

Figure 3.11: **Tunnel spectroscopy of Al/InAs hybrids. a** False-colour SEM of Al/InAs hybrid NW device for tunnel-spectroscopy and **b-f** bias spectra from the five studied devices DA1-DA5. All devices showed a hard induced superconducting gap with coherence peaks at $V_{\mathrm{sd}} = \pm\Delta/e = \pm 0.20 - 0.25$ mV, highlighted in DA5 by the line trace at $V_{\mathrm{g}} = -9.195$ V. SEM scale bar represents 200 nm. **b** Logarithmic line traces of conductance G normalised to the out-of-gap conductance G_{N} vs. V_{sd} at fixed gate voltages indicated by white lines in the bias spectra of Fig. 3.11**a**. The traces were vertically offset by two decades for clarity.

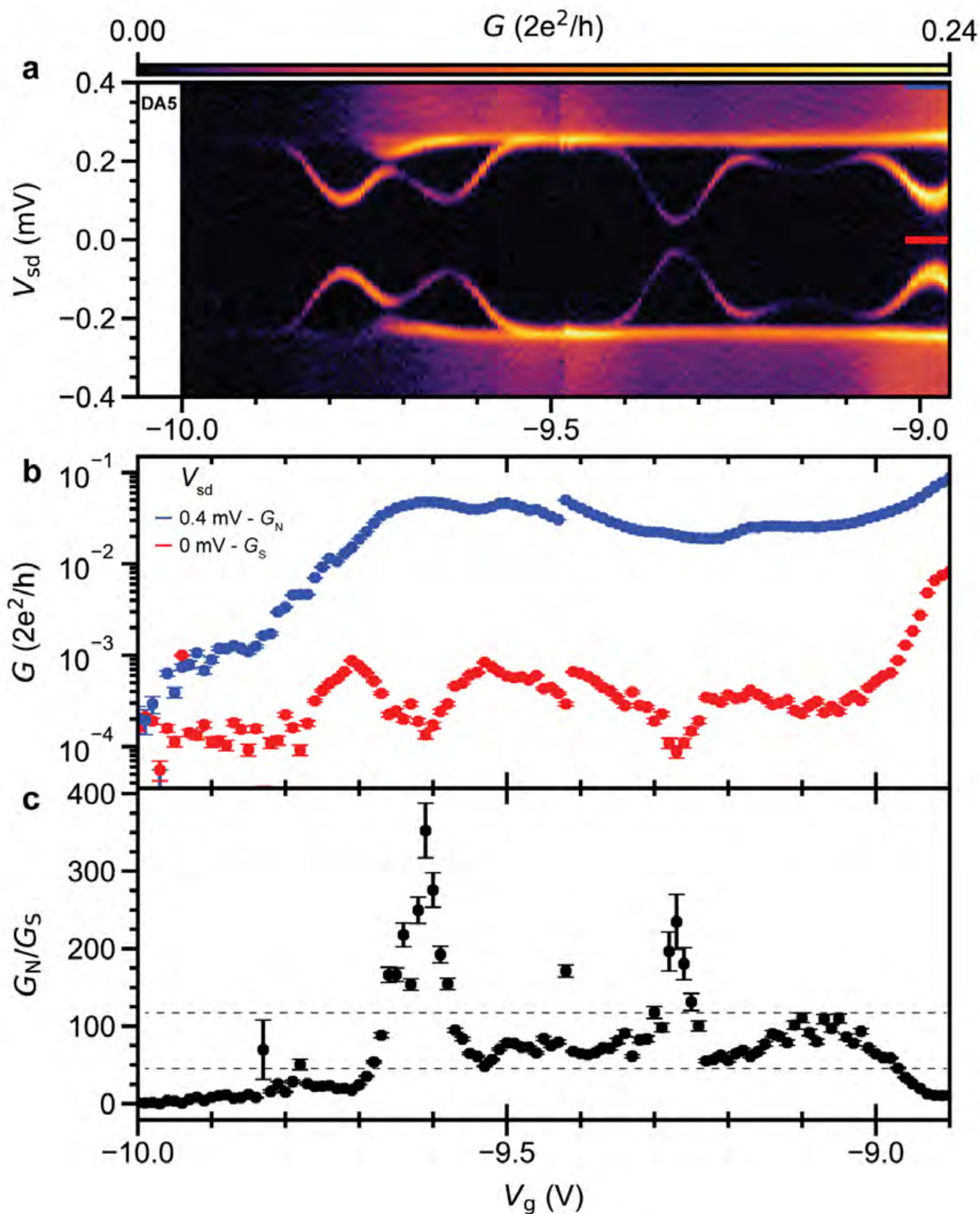

Figure 3.12: **Gap hardness statistics. a** Bias spectroscopy from DA5. **b** Normal state and superconducting state conductance, G_{N} (blue) and G_{S} (red) averaged from 2000 and 100 individual measurements, respectively, at each V_{g}. **c** Hardness, $G_{\mathrm{N}}/G_{\mathrm{S}}$ calculated from the data in **b**. Dashed lines are guides highlighting that hardness was $G_{\mathrm{N}}/G_{\mathrm{S}} = 50 - 110$ over most of the measured V_{g} range.

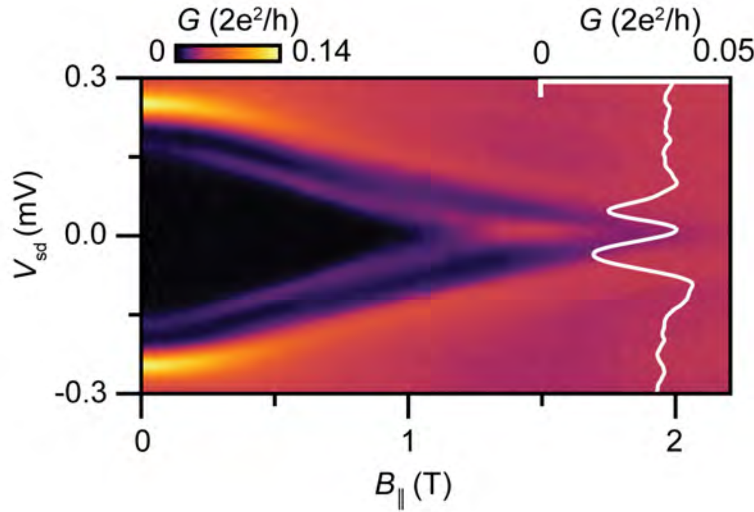

Figure 3.13: **Magnetic field dependence of Al/InAs hybrids.** Measured G vs. $B_{||}$ and V_{sd} for V_{g} fixed at the position of the line trace in Fig. 3.11**D5**. The superconducting gap closes at $B_{\mathrm{C}} \sim 2$ T. A peak at zero bias emerges at $B = 1.3$ T from coalescing bound states. Line trace was taken at $B_{||} = 1.5$ T.

Stability of *in-situ* Majorana island devices

Aluminum based superconducting island devices (as introduced in Sec. 2.2.2), shown in Fig.3.14**a**, were measured to compare the performance of the shadow lithography devices with conventional etched devices. In the ideal case, V_{g} acts only on the hybrid segment to tune island charge occupation, while $V_{\mathrm{sg1,sg2}}$ statically define barriers in the bare segments. However, stray fields from V_{g} also couple to the bare segments and cause the barrier properties to change. To compensate for this, the cross-coupling between $V_{\mathrm{g}}/V_{\mathrm{sg1}}$ and $V_{\mathrm{g}}/V_{\mathrm{sg2}}$ was experimentally determined, and set as proportionality factors in the sweeps. Figure 3.14**b**, shows G vs. V_{sd} and V_{g} exhibiting $2e$-periodic Coulomb diamonds corresponding to a charging energy $2E_{\mathrm{C}} \sim 130\ \mu$eV (dashed lines). Quasi-particle $1e$ periodic charging is seen for $|V_{\mathrm{sd}}/e| > \Delta \sim 180\ \mu$eV (solid lines) [50, 67]. Figure 3.14**c** shows the temperature dependence of the low-bias V_{g}-induced charging. The $2e$ periodic state persists up to $T \sim 250-300$ mK where a transition to $1e$ periodicity occurs due to thermal excitation of quasi-particles. This value is set by Δ and island volume and was comparable to that observed in etched devices [42, 52, 67].

The single electron sensitivity makes Majorana island devices highly sensitive to the local electrostatic environment. Therefore, V_{g}-induced discrete charging of nearby impurity sites can lead to uncontrolled switches of the island charge/parity. This typically limits the stable operation range to $\lesssim 20$ electrons [42, 50, 68]. The shadow-patterned Al/InAs devices exhibited an increase of this range by at least an order of magnitude consistent with a cleaner electrostatic environment due to the obviation of etching i.e. not having Al residue by the tunnel barriers or a damaged InAs surface. This is demonstrated in Fig. 3.14**d** by the stable evolution of 182(364) consecutive $2e(1e)$ charge states accessed by continuously sweeping V_{g} and an interleaved step-wise increase of $B_{||}$. The island is superconducting in this field range, and the bifurcation of the spectrum at $B_{||} \sim 200\,\mathrm{mT}$ is caused by the appearance of an odd parity bound state below the gap, which can happen for various reasons as discussed in Sec. 2.2.2. Several of these effects leading to the $1e$-periodic bifurcation in $B_{||}$ with distinct behaviour of peak spacing and amplitude modulation were observed within the gate range. Examples are shown in Figs. 3.14**e-g**, zooming in on three regions of panel Fig. 3.14**d**. Fig. 3.14**e** features $1e$-spacing independent

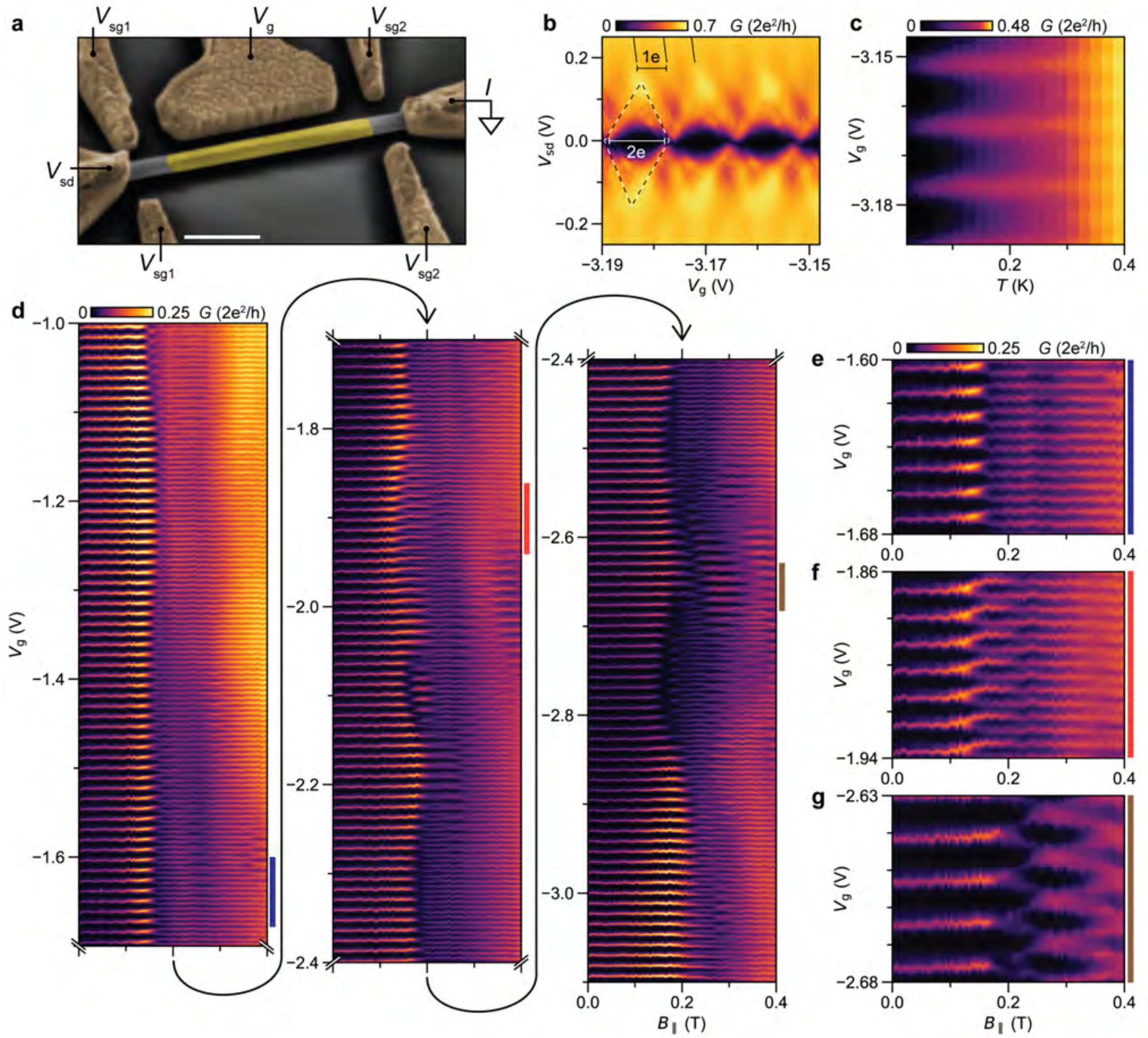

Figure 3.14: **Electron transport in a Majorana island.** **a** False color SEM of shadow patterned Al/InAs island device. Middle gate voltage V_g was varied, with the four other gates used to generate tunnel barriers. Scale bar represents 500 nm. **b** Bias spectroscopy showing Coulomb blockade diamonds with $2e$-periodicity in V_g for $V_\mathrm{sd} < \Delta$ and $1e$-periodicity for $V_\mathrm{sd} > \Delta$. **c** Zero bias conductance G vs. V_g and temperature, T. 1e-periodic peaks above $T = 250 - 300$ mK emerge due to thermally excited quasi-particles. **d** A single, continuous measurement of G vs. V_g and $B_\parallel$, presented without corrections for, e.g., switching. 364 electrons were removed from the island. The $2e$- to $1e$-periodic transitions in the range $B_\parallel = 0.15 – 0.25$ T occur as bound states move to zero energy. This can occur with **e**, equal spacing between $1e$ peaks, or **f**, $B_\parallel$-dependant spacing, depending on the nature of the bound states [42, 50, 68]. **g** A parity transition to a state where only odd numbers of electrons are on the island is also possible [68]. The cross-coupling of V_g to the tunnel barrier segments was compensated by $V_\mathrm{sg1,sg2}$ using experimentally determined proportionality factors.

of $B_{\parallel}$, whereas in Fig. 3.14**f** the peaks spacing and amplitude are modulated by $B_{\parallel}$ [91]. Similar to the zero bias peak observed in tunnel spectroscopy (Fig.3.13), the behaviour in 3.14**f** has been suggested as a possible signature of topological superconductivity in island devices [42, 50, 68, 71, 91]. However, a detailed study involving numerous devices of varying island lengths to confirm the presence of topological states was not the aim of our study. Rather, we focussed on showing the stability of devices, which was evidenced by the fact that we observed different phenomena within a single continuous measurement. A third observed behaviour, shown in Fig.3.14**g**, was a transition between two $2e$-periodic ground states occurring with a change in the parity on the island, as introduced in Sec. 2.2.2.

The order of magnitude increase in measurement range enables tracking slowly varying features such as for example, the field of the $2e$-$1e$ transitions which could be linked to gate-dependent g-factor of the bound state [72] and this way provide aid in fine-tuning of the cross-coupled parameters towards the topological regime [65].

3.2.4 Conclusions and outlook

Aluminium evaporated from a e-beam target onto InAs NWs was successfully benchmarked against that from a MBE solid-source cell and found to yield Al/InAs hybrid nanowires with the same epitaxy as the MBE grown variants. The shadow lithography platform is thus compatible in manufacturing Al/InAs nanowires with the desired structural properties. Low temperature electron transport characterisation confirmed the high quality of the Al/InAs hybrids synthesized using shadow lithography where 5 out of 5 devices showed a hard induced gap. The high yield compares favourably with conventional device processing using wet etching, where etch quality variations result in much lower yield. Variations in gap hardness across a ~ 1 V range was measured and averaged based on 2000 zero-bias measurements at each step in gate voltage generating a statistically more robust value interval for the figure of merit compared to values based on single measurements. The hybrids showed magnetic field-compatibility with a sub-gap state g-factor of 6.5, larger than the g-factor of the hybrid system. Majorana island devices exhibited an unprecedented large range electrostatic stability which in future may enable reliable, rapid identification of the topological regimes. Furthermore, the stable, non-hysteretic operation of the shadow devices will likely allow adapting the automatic tuning procedures under development for spin-qubit devices [92].

3.3 In/InAs hybrid nanowires

Successfully establishing the shadow mask lithography platform and benchmarking it using Al/InAs hybrids opened for implementations with other superconductors. The first new hybrid nanowire system to be presented here is In/InAs.

Previous reports on the structural properties indium showed that bulk indium crystallizes in a tetragonal body-centred (TBC) phase within space group $I4/mmm$ at room temperature and atmospheric pressure, [93, 94]. The TBC crystal structure has been observed at the nanoscale, as reported for indium nanoparticles of 15 ± 2 nm mean diameter decomposed from an organometallic precursor [95]. It can be noted that pressures above 45 GPa induces a phase transition to the face-centred orthorhombic crystal structure [96]. Confining indium in 7 nm porous glass cavities results in a different pressure-induced phase transition to the face-centred cubic structure [97]. In 2011, attempts were made by M.H. Madsen (NBI) to deposit indium on *in-situ* Au grown, non-shadowed, InAs NWs using the indium cell of the MBE. It was found that depositing at room temperature resulted in indium grain formation on the NWs [unpublished work]. The only prior reports on the structural properties of indium on InAs NW facets has been from experiments towards self-catalysed InAs NW growth and growth of kinked InAs nanowires by knocking over In droplets to sit on the NW facets [98]. In those experiments, the indium catalyst droplets on top of the nanowires were annealed in order to destabilise and subsequently slide down and pin on NW facets. The indium droplets were found to be amorphous after cool-down. This is consistent with the low heat of vaporisation for indium, $\sim$ 230 kJ/mol, and suggests that low substrate temperatures $T < 0$°C are likely required to produce crystalline indium, similar to aluminium [35].

3.3.1 Sample descriptions

Two InAs nanowire samples were grown using single-sided shadow mask substrates, featuring differing nanowire diameters. The first, I1 had EBL-defined catalysts with diameter = 100 nm and thickness = 15 nm, while the second, I2, had catalyst diameter = 100 nm and thickness = 15 nm. Note that nanowire diameter depends on droplet volume in the liquid phase at $T = 447°$C, and therefore a nominally identical “EBL Au” growth procedure produced nanowire diameters of $\sim$ 100 nm and 120 nm for I1 and I2, respectively (Table 3.2). After growth, the nanowire samples were transferred *via* UHV to the metal deposition chamber where indium deposition was performed at $T_{\mathrm{S}} \sim -150°$C with a tilt angle $\theta = 10°$ along the $[11\bar{2}]$ direction for a 3-facet shell with nominal thickness 40 nm. The nominal deposition rates were 0.3 Å/s (I1) and 3 Å/s (I2). The higher rate of deposition for I2 was used in an attempt to promote the formation of an increased density of indium nucleation sites for the thin film growth [99].

	t_{Au} (nm)	T_{S} (°C)	t_{In} (nm)	In evap. rate (Å/s)
I1	15	-150	40	0.3
I2	20	-150	40	3

Table 3.2: **In/InAs samples.** Overview of Au catalyst thicknesses, t_{Au}, indium deposition temperatures T_{S} (thermocouple), indium film thicknesses t_{In} and evaporate rates for the two In/InAs nanowire growths I1-I2. The indium film thicknesses are the nominal evaporated film thicknesses measured by the quartz crystal monitor.

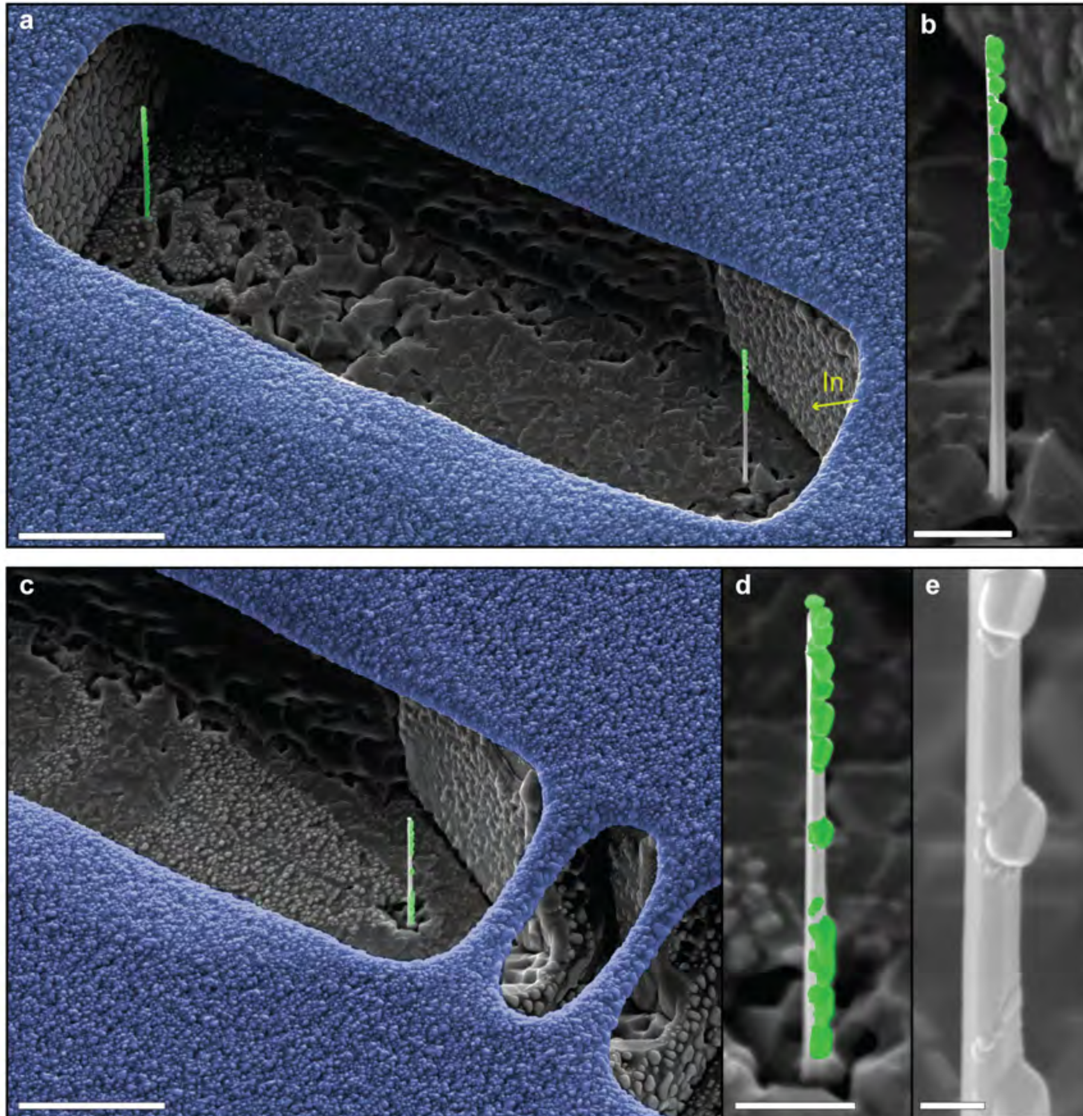

Figure 3.15: **Scanning electron microscopy of as-grown In/InAs hybrid nanowires.** False-colored SEMs of the as-grown hybrid nanowire growth substrate featuring indium (green) evaporated onto InAs nanowires through an SiOx shadow mask (blue). **a-b** In/InAs nanowires grown by a wide bridge SiO_x shadow mask (blue) for NS device geometry. Indium was evaporated from the direction indicated by the green arrow with a 10° angle between substrate surface and the crucible. This provided a partial shadow for the rightmost nanowire (magnified in **b**). Indium formed several grains on the nanowire facets. **c-e** In/InAs nanowires grown by a double bridge shadow mask geometry providing two larger gaps in the In grain formation. Scale bars: **a**,**c**: 5 μm, **b**,**d**: 1 μm, **e**: 200 nm.

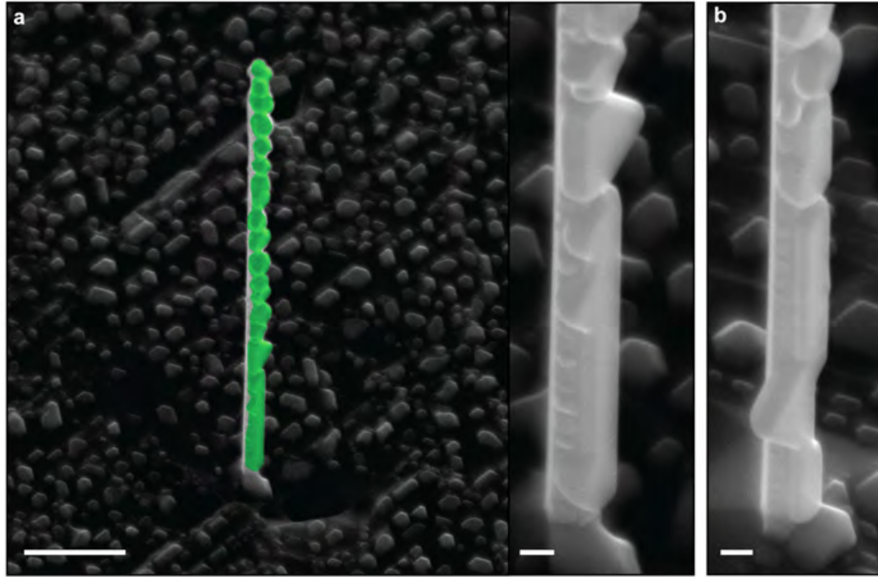

Figure 3.16: **Scanning electron micrographs of as-grown In/InAs nanowires** False-colored SEM micrographs of indium (green) evaporated onto InAs nanowires. The nanowires were not grown by any shadow mask features and thus coated in full length. Larger continuous indium segments formed near the base of the wires. Scale bars: **a**: 1 μm (left), 100 nm (right), **b**: 100 nm.

3.3.2 Structural characterisation

Figure 3.15 shows scanning electron micrographs of the as-grown In/InAs hybrids from sample I2 at the wide bridge (Fig 3.15**a-b**) and double bridge (Fig. 3.15**c-e**) geometries. The higher magnification SEMs in Figs. 3.15**b** and 3.15**d-e** reveal that indium formed non-uniform grains on the InAs nanowires, in contrast to the thin films observed for aluminium. Both I1 and I2 exhibited a granular indium structure, albeit with some nanowires on I2 featuring extended continuous segments of $\sim$ 500 nm towards the base as shown in Fig. 3.16. This could arise from the overall larger diameter of the wires from I2 due to a larger catalyst volume or the higher deposition rate. Facet area increase could facilitate a recrystallisation that formed the extended grain segments [99]. The indium grains had anisotropic surfaces, featuring sharp grain edges and well-defined flat surfaces.

Structural analysis of the indium grains using TEM revealed them to be crystallised in the same TBC structure as reported for bulk indium [94], as will be shown in the following. Double junction NWs were used for TEM, and alignment performed using the bare InAs segment. TEM characterisation centred on the isolated indium segment between the two bare junctions to limit the potential for a large number of grains to influence the signal. Using longer segments proved especially problematic for SAD where having $>$ 20 grains contributing to the signal made distinguishing diffraction signal origins prohibitively difficult. TEM, SAD, and DF signal from a double junction In/InAs nanowire are shown in Fig. 3.17. The displayed NW region in 3.17**a**, found between two shadow junctions, featured $\sim$ 12 indium grains of various sizes spanning from a projected grain area of $\sim$150 nm^2 to $\sim$25 000 nm^2. The associated SAD signal (Fig. 3.17**b**) shows that the InAs NW was aligned parallel to a $\langle 2\bar{1}\bar{1}0\rangle$ zone-axis. Additional peaks (marked by green circles) arose from diffraction in the indium crystals. Interestingly, an intense pair of indium Bragg peaks aligned with the InAs $\{1\bar{1}00\}$ facet planes are seen (blue). The dark field signal associated with one of these peaks, marked by a blue circle in Fig. 3.17**b**, is shown in Fig. 3.17**c**. The DF signal revealed the selected Bragg peaks to be common for all the indium grains interfacing the aligned facets. All grains in that region thus featured crystal planes that were parallel to facet

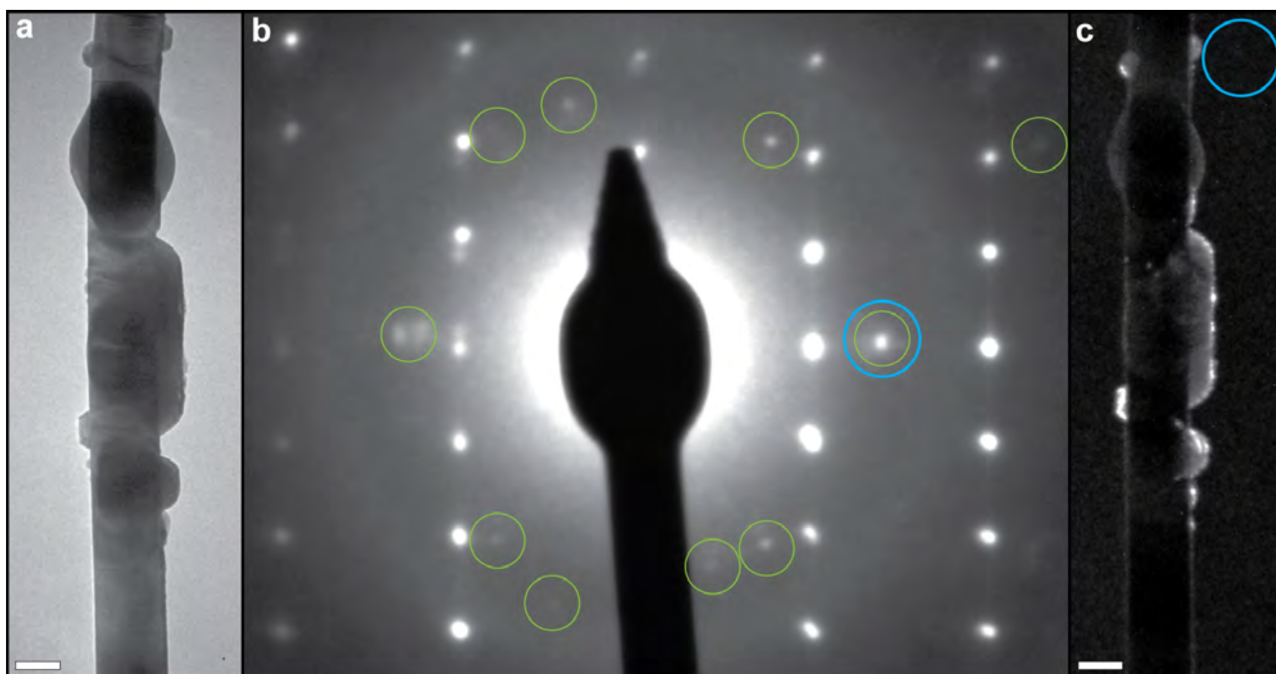

Figure 3.17: **Low magnification TEM and selected area diffraction of In/InAs nanowire hybrids**. **a** TEM of an In/InAs hybrid nanowire shadow mask patterned by two SiOx bridges (like in Fig.3.15**c**). The InAs nanowire featured ~ 12 indium grains of various sizes between the shadowed segments. **b** SAD signal from **a**. The rectangular peak grid is a signature of the InAs WZ crystal aligned parallel to $\{1\bar{1}00\}$ facet planes. Additional peaks (green circles) arose from the indium grains. **c** Dark field signal from placing the objective aperture on indium peaks aligned to the facet planes (blue circle in **b**). Scale bars: 50 nm.

surfaces, well in agreement with the initial SEM observations of the flat, anisotropic grain surfaces.

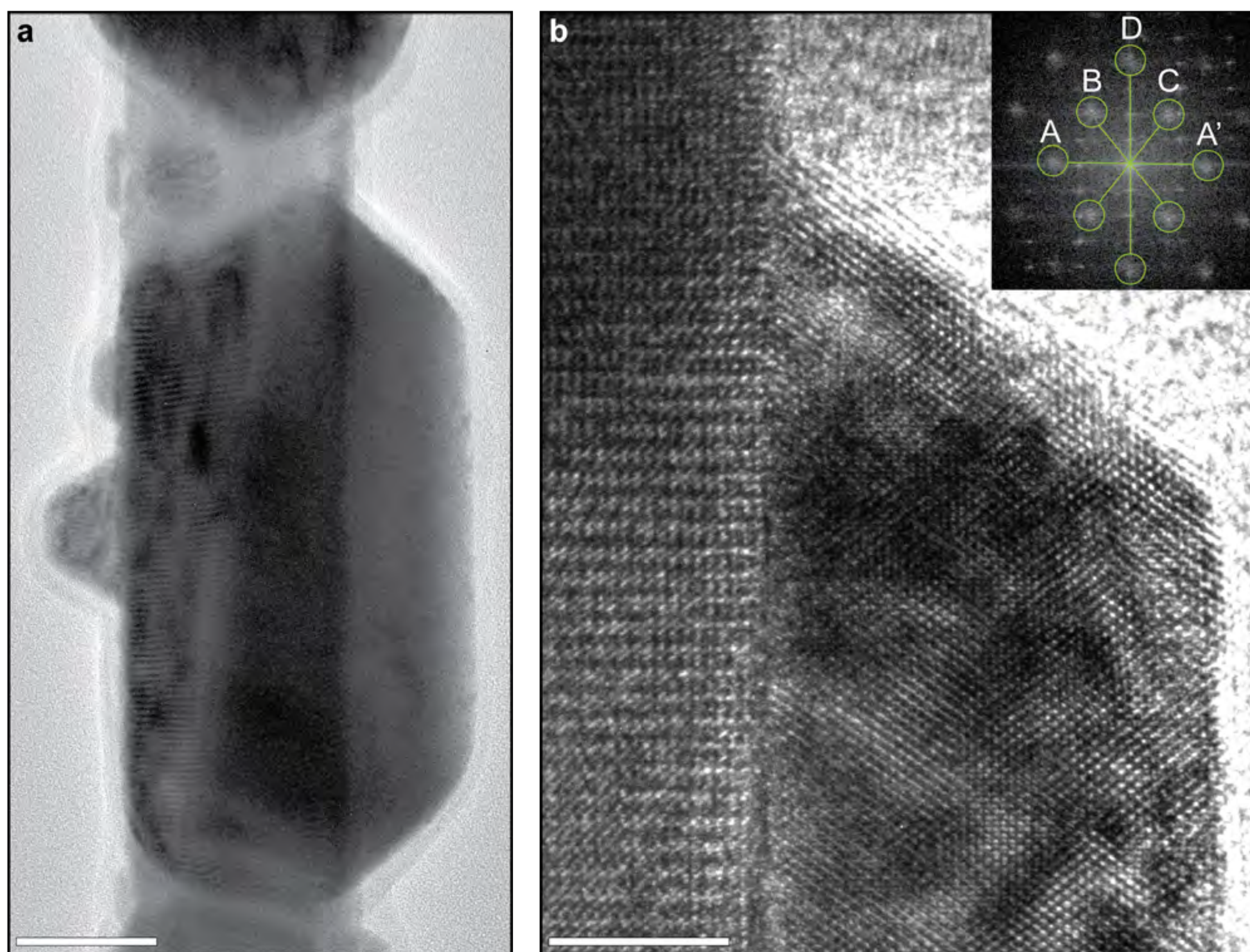

Figure 3.18: **Transmission electron microscopy of In/InAs hybrids.** **a** TEM of an In/InAs nanowire with the electron beam aligned parallel to $\{1\bar{1}00\}$ facets. Indium grains of various sizes formed on the nanowire with anisotropic surfaces and top surfaces aligned to the nanowire surface. Moiré fringes are visible in overlapping grains, suggesting rotational variation. **b** HRTEM of an indium grain interfacing an InAs facet. Atomic lattice fringes are visible throughout the grain with overlaying Moiré fringes. FFT (insert) showed that crystal planes denoted A and D in the indium grain aligned with facet $(1\bar{1}00)$ and axial (0002) planes, respectively. Scale bars: **a**: 50 nm. **b**: 5 nm.

TEM imaging at higher magnification (Fig. 3.18**a**), confirmed well-defined surface formation and showed that the grains were mostly disconnected on the NW surface. Moiré fringes in regions where indium grains overlapped each other (seen in Fig. 3.18**a**,**b**), suggesting small rotational offsets between crystals.

In HRTEM images, like Fig. 3.18**b**, 3.19**a-b**, well-resolved atomic lattice fringes in the indium grains enabled measurements of interplanar distances, $d_{(hkl)}$. Additionally, fast Fourier transformations of the crystalline periodicity in the HRTEM images made it possible to measure the angles between indium planes A, B and C like featured in inserts of Fig. 3.18**b** and 3.19**a**. Measurements of the angles between the indium related intensity FFT peaks, where O denotes the position of the central peak of the FFTs, and interplanar distances are compiled in Table 3.3 along with calculated values from low-index planes in TBC indium reported in literature. Tables of calculated angles and distances for all low-index planes in TBC indium are displayed in Appendix 5.2.

The measured angles and interplanar distances of A, B, C & D matched the TBC crystal phase with with

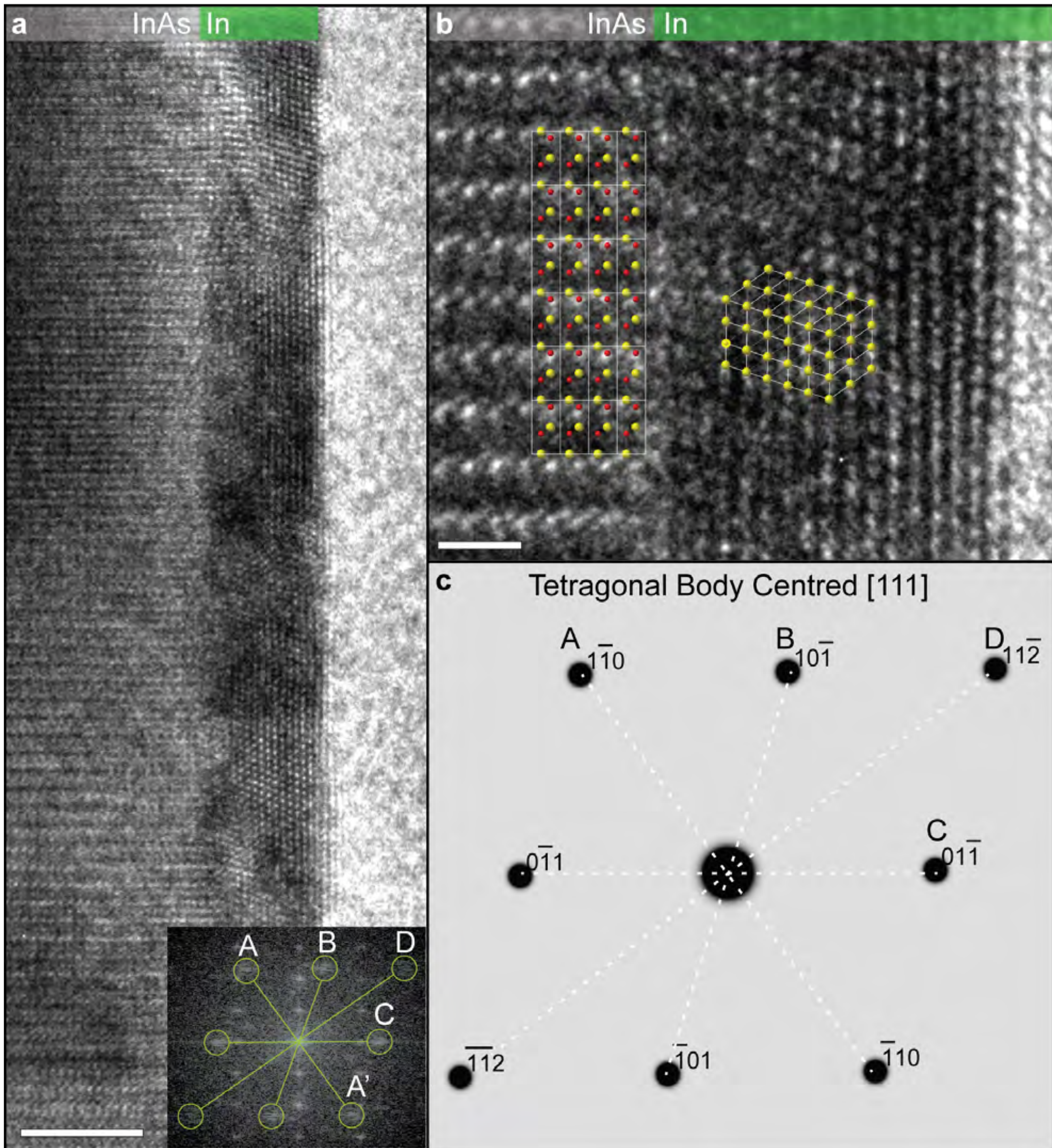

Figure 3.19: **Transmission electron microscopy of In/InAs hybrids. a** HRTEM of indium interfacing an InAs nanowire facet. Indium lattice fringes are visible through the indium film with contrast variations suggesting overlapping grains. FFT (insert) shows the alignment of planes with respect to the InAs. C fringes align with the nanowire facet planes **b** HRTEM of an In/InAs interface with CrystalMaker^{TM}model overlay of wurtzite InAs and tetragonal body-centred (TBC) indium [111] zone-axis. **c** Simulated transmission electron diffraction signal of TBC indium [111] zone-axis, matching the observed indium crystal structure. Scale bars: **a**: 5 nm. **b**: 1 nm.

FFT angle	Avg. measured angle	TBC angle	Calc. angle
$\measuredangle AOB \wedge \measuredangle A'OB$	54.1° ± 3°	$\angle\{110\}O\{101\}$	53.8°
$\measuredangle BOC$	72.3° ± 3°	$\angle\{101\}O\{011\}$	72.4°
$\measuredangle AOC \wedge \measuredangle A'OC$	54.3° ± 3°	$\angle\{110\}O\{101\}$	53.8°

Interplanar dist. in HRTEM	Avg. measured dist.	TBC interplanar dist.	Calc. dist.
d_A	2.3 Å ± 0.2 Å	$d_{(110)}$	2.30 Å
d_B	2.8 Å± 0.3 Å	$d_{(101)}$	2.72 Å
d_C	2.8 Å± 0.3 Å	$d_{(101)}$	2.72 Å
d_D	1.7 Å± 0.2 Å	$d_{(112)}$	1.68 Å

Table 3.3: **Angle measurements from FFT signals of Figs. 3.18b and 3.19a**. From symmetry, $\measuredangle AOB$ ($\measuredangle AOC$) is equivalent to $\measuredangle A'OB$ ($\measuredangle A'OC$) which is why they share table row. A' denotes the opposite reflection of A, introduced here to clarify the reference points for the angle measurements. The uncertainty of the measurements was assessed to be ± 3° based on the FWHM of the peaks. Interplanar measurements from HRTEM micrographs in Figs. 3.18**b** and 3.19**a**. All measurements were based on averaging 6-10 planes. The propagated uncertainty from calibration and measurement was assessed to be $\sim 10\%$

$A = \{110\}$ and $B = C = \{101\}$ and $D = \{112\}$ constituting $\langle 111 \rangle$ zone-axes. The two indium crystals measured here thus shared a [111] zone-axis, but aligned with different out-of-plane orientations. Figure 3.18**b** had an [110] out-of-plane orientation and [112] in-plane orientation, while the grain Fig.3.18**b** had an [011] out-of-plane orientation and no low-index in-plane orientation. All ten studied indium grains featured $\langle 111 \rangle$ zone-axes parallel to the nanowire facets. A different example of a grain featuring the [111] zone-axis and [110] out-plane-orientation is shown in Fig. 3.19**b** with a matching overlay of TBC indium and WZ InAs crystal models simulated in CrystalMaker$^{\text{TM}}$software.

Finally, bi-crystal domain mismatches between indium and InAs were calculated to assess the potential for epitaxy and the anticipated strain between the crystals. The domain mismatch is a relative length difference between domains of single or multiple interplanar distances in InAs and single or multiple parallel aligned lattice planes in indium grains. The calculated mismatch percentage between low-index TBC indium interplanar distances and the interplanar distances of axial InAs (0002) (3.498 Å) and transverse InAs ($2\bar{1}\bar{1}0$) (2.142 Å) planes are tabulated in Appendix 5.2. This model considers only geometrical mismatch, and therefore doesn't take into account thermodynamic relaxation which may impact the possibility of epitaxial indium thin film formation on InAs. Nevertheless, it provided insight to the possible origins of observed crystal alignments. The observed In grains with [111] zone-axes had a 1:1 domain mismatch with transverse InAs planes of 2.6 % and the observed axially aligned (112) planes had an axial 2:1 domain mismatch of 3.7 %. These mismatch values exceeded those usually deemed realistic for long-range, dislocation-free epitaxy (< 1 %), but within those for domain-matched epitaxy [35, 100, 101]. As a consequence, the interface strain was likely too large to allow long-range epitaxial growth of indium, but instead, as observed e.g. in Fig 3.18**b**, allow growth of grains domain-matched to the InAs crystal.

Facet-aligned, well-defined out-of-plane crystal planes in all the indium grains suggests that grain formation during growth was mainly driven by minimisation of grain surface energies, where $\{110\}$ and $\{101\}$ could represent surface planes with local surface energy minima [102]. Formation of a multitude of disconnected grains with a large size range suggested the following; Firstly, that the probability for the indium to form a nucleation site was low i.e. the critical nucleation size was high. Compared to the incoming indium flux from the e-beam source, only a small number of grains nucleated and grew, partially covering the nanowire

surface. Secondly, the energetic cost of forming grain boundaries between grains may have been too low for most grains to recrystallise. This notion is supported by observation of Moiré fringes in regions where indium grains overlapped each other (seen in Fig. 3.18**a**,**b**), suggesting small rotational offsets between crystals which can arise from grain boundaries formed between them.

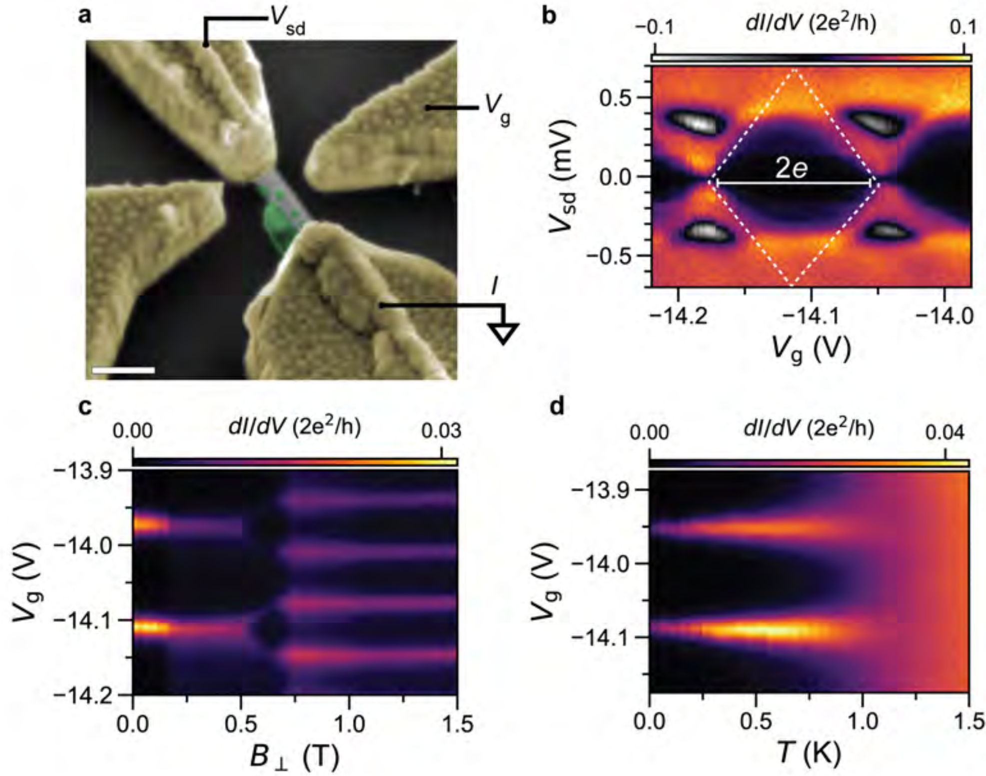

Figure 3.20: **Electron transport in superconducting indium islands. a** False colour SEM of In-coated (green) hybrid contacted with Ti/Au (yellow). The indium grains acted as self-formed superconducting islands. Scale bar: 200 nm. **b** Differential conductance, dI/dV, versus source-drain bias, V_{sd}, and gate voltage V_{g} shows a 2-e periodic diamond structure characteristic for superconducting islands [50, 103] with $\Delta \sim 0.45$ meV. **c** Like for Al/InAs, a perpendicular magnetic field broke $2e$-periodic charging into $1e$-periodic charging of the island at $B_\perp = 0.75$ T. **d** The island remained $2e$-periodic, i.e. free of quasi-particles up to at least $T = 1.2$ K.

3.3.3 Electrical characterisation

Electron transport measurements of In/InAs devices in the dilution cryostat showed an interesting interplay between the InAs nanowire and the indium grains. Initially, the aim of the measurements was to perform tunnelling spectroscopy for the characterisation of an induced superconducting gap, if any. To this end, a single indium grain on the hybrid NW was contacted in the tunnel spectroscopy geometry described in Sec. 2.2.2 and shown in Fig. 3.20**a**. However, the device behaved electrically as a superconducting island, like introduced in Sec. 2.2 and seen for the Al/InAs hybrids (Sec. 3.2.3). Like for Al, bias spectroscopy (Fig. 3.20**b**) showed $2e$-periodic charging as a function of gate voltage, V_g with characteristic regions of NDC near the the superconducting gap between $\pm\Delta = 0.45$ meV. The gap value was reduced 85% from the bulk value $\Delta_{\text{bulk}} = 0.53$ meV [104]. The $2e$-periodicity was broken into $1e$-periodic charging by a perpendicular magnetic field at $B_\perp = 0.75$ (Fig. 3.20**c**),

like seen for the Al/InAs hybrids (Sec. 3.2.3). The change of periodicity could happen for the same reasons discussed for Al/InAs or because the critical magnetic field was reached. Increasing temperature also broke $2e$ periodicity via thermally excited quasiparticles [67, 105]. For the indium device in Fig. 3.20**d**, the peaks broadened, and possibly split at $T \sim 1.2$ K, putting a lower bound on the device operation temperature. This indicated a potential for higher device operation temperature by using indium based hybrids in stead of aluminium based hybrids where thermally excited electrons started tunnelling through the island $T = 0.25 - 0.3$ K (Fig. 3.14**c**), splitting the $2e$-transport to $1e$.

3.3.4 Conclusions and outlook

In summary, In/InAs provided a contrast to Al/InAs in structural properties whereby an unfavourable bicrystal interface and grain growth kinetics lead to the formation of disconnected epitaxial crystalline grains, rather than an epitaxial thin film. The grains formed in the bulk TBC phase with well defined low-index surfaces suggested that the grain formations and re-crystallisations primarily were driven by surface energy minimisation. The absence of indium thin film formation was likely a consequence of low nucleation probability on the surface as well as high interface energy/strain to InAs. Electrically, the grains behaved as superconducting islands. Compared to Al island devices, an increased poisoning temperature combined with the fact that the superconducting gap remained close to the bulk value, suggests indium as a potentially useful material assuming ultimate control of film/island growth. Controlling island size would be an interesting route to obtain chains of superconducting islands for, e.g., Kitaev chains [16], or to study Majorana interactions between two adjacent islands [106]. Achieving a continuous thin film would allow for hardness characterisation of the induced superconducting gap, while utilising the shadow lithography technique. Deposition of thicker indium films may produce continuous thin films, although the discussed barriers to epitaxy would likely result in a polycrystalline structure. A route to obtain a crystalline thin film may be the introduction of an intermediate superconducting layer (e.g Al), to potentially increase the probability of forming nucleation sites on the surface or to mediate strain. Alloying indium (e.g. with tin, InSn is a $T_{\mathrm{C}} = 6$ K superconductor [107]) could be an alternative way of promoting the surface wetting properties. Since amorphous indium thin films also are superconducting ($T_C \sim 4.5$ K) [108], annealing the indium grains to obtain an amorphous thin film could be another interesting approach.

3.4 V/InAs hybrid nanowires

The contents of this section is largely based on the manuscript of Pub. A.

Since previous reports on vanadium has showed that it, in bulk, is a type II superconductor with a critical temperature, $T_C = 5.4$ K and critical magnetic field, $B_c \sim 0.1$ T [109, 110, 111], it is an interesting candidate towards expanding the use of semi-super hybrids to operation in higher temperatures and fields. Hybrid devices based on III-V nanowires with *ex-situ* e-beam deposited vanadium contacts have previously been used for studies of Andreev bound states [65] and in superconducting quantum interference devices (SQUIDs) [112, 113]. However, there were no prior reports of *in-situ* integration of III-V nanowire and vanadium thin film growth under UHV conditions and no structural analysis reported. Structurally, it is expected that the lattices of body-centred cubic (BCC) vanadium and InAs would match in certain orientations [35, 101], which motivated the study. One expected potential challenge was that obtaining monocrystalline growth of vanadium on sapphire by e-beam evaporation required substrate temperatures exceeding 460°C [114]. This temperature regime is incompatible with InAs due to desorption of arsenic at approximately 400°C [115].

3.4.1 Sample descriptions

Five trench-patterned (111)B growth substrates, V1-V5, were used in the MBE to grow InAs following the "*in-situ* Au" scheme described in Sec. 3.1.7. A sixth sample, V6, was grown using a single-sided bridge shadow masks. Vanadium was deposited along the $[11\bar{2}]$ substrate orientation with a rate of ~ 1 Å/s and at a tilt angle $\theta = 28°$. This ensured continuous 2-facet shells on each nanowire, with little or no effects of shadowing from neighboring nanowires, given the average inter-wire pitch > 5 μm. The six growths (V1-V6) were conducted with different vanadium deposition conditions and film thicknesses as shown in Table 3.4. The substrates were cooled with liquid nitrogen to minimum $T_\mathrm{S} = -150$°C, or heated to maximum $T_\mathrm{S} = 250$°C. In attempts to achieve variation in crystallinity, four different substrate temperatures in this range were investigated as well as different nominal vanadium film thicknesses ranging 12-27 nm. In an attempt to protect the vanadium from subsequent oxidation, potentially impairing the superconducting properties when leaving the MBE system [116], sample V3 was capped with an 11 nm full shell of amorphous AlO_x deposited by e-beam evaporation immediately after the vanadium deposition. Sample V6 was used to demonstrate the double angle deposition scheme introduced in Sec.3.1.2. Two evaporations of 20 nm each were performed with angles of 16° and 17°.

	T_S (°C)	t_V (nm)
V1	-150	19
V2	25	26
V3	25	27*
V4	100	12
V5	250	~ 12
V6	25	40 (2×20)

Table 3.4: **V/InAs samples.** Overview of substrate thermocouple temperatures T_S during vanadium deposition and measured vanadium film thicknesses t_V samples V1-6. Sample V3 - marked with * had an additional 11 nm AlO_x full shell cap. The film thicknesses were measured from transmission electron micrographs with one of the two vanadium-covered nanowire facets aligned parallel to the electron beam.

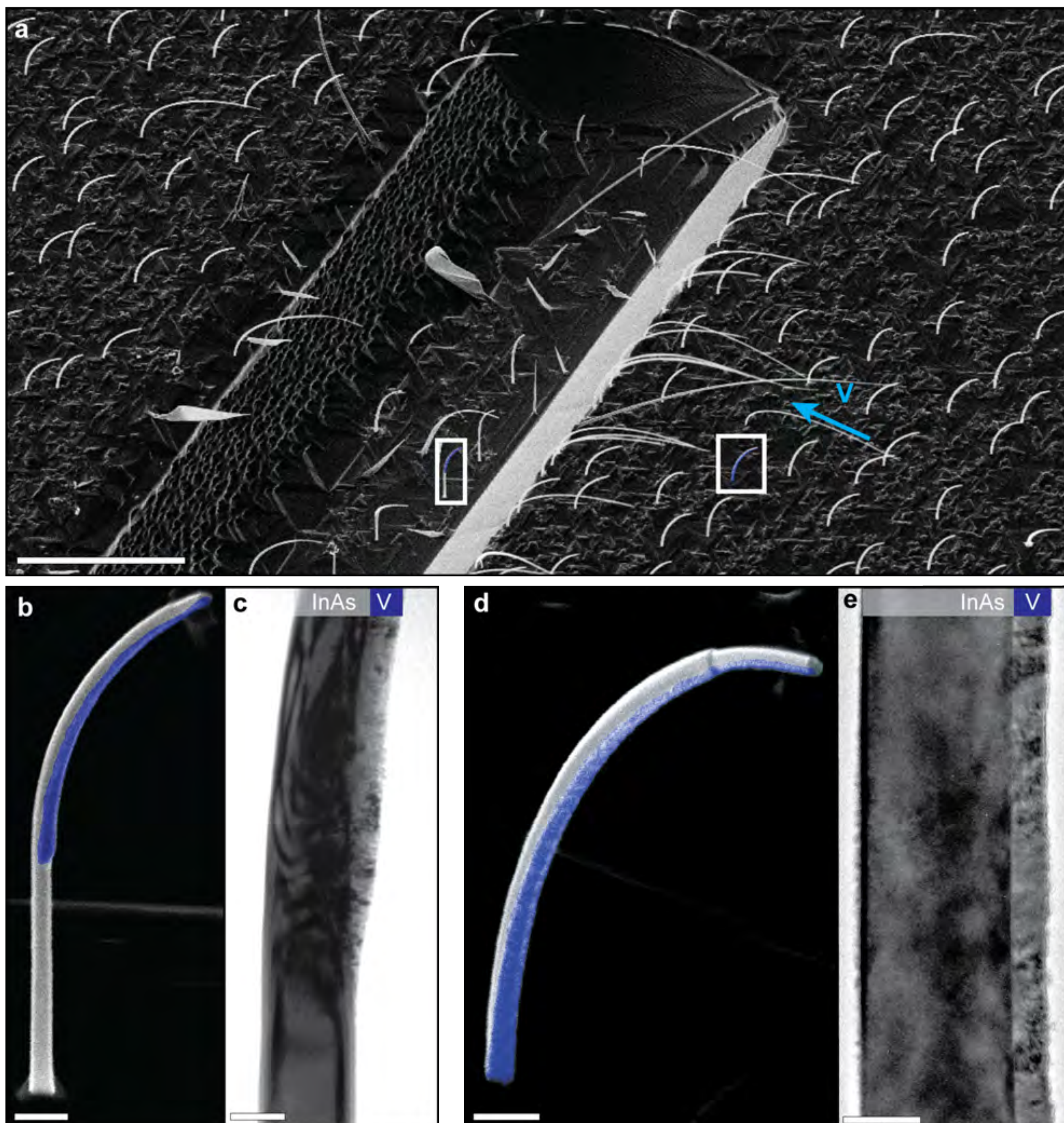

Figure 3.21: **Overview of as-grown V/InAs nanowires from room temperature deposition. a** SEM of as-grown V/InAs nanowires in a sample featuring lithographically defined etched trenches (sample V2). The nanowires are bent towards the vanadium half-shell. Blue arrow indicates the direction of vanadium flux during evaporation. White frames indicate the position of the magnified nanowires in frame **b** and **d**. **b** SEM of a single InAs nanowire coated by vanadium (blue) in the upper-half segment. Note that the nanowire is bent only in the V coated segment. **c** TEM of an upper-half coated V/InAs nanowire at the transition from fully coated to fully shadowed. Bending contours indicate strain in the coated nanowire segment. **d** SEM of an InAs nanowire coated by vanadium (blue) in full length. **e** TEM of a V/InAs nanowire. Scale bars: **a**: 10 μm, **b, d**: 300 nm, **c**: 100 nm, **e**: 50 nm. Micrographs **a, b, d** were acquired with the substrate tilted by 30°.

3.4.2 Structural characterisation

Figures 3.21**a, b, d** show electron micrographs of V/InAs hybrid nanowires after growth and subsequent vanadium deposition at room temperature (sample V2). The nanowires from all six growths bend towards the direction of the vanadium half-shell. Nanowires that grew in the trench had uncoated nanowire segments from being out of line-of-sight during evaporation (3.21**b**). These uncoated segments remained straight and confirmed that the vanadium shells caused the bending. The bending may have been a result of e.g. difference in thermal expansion coefficients between InAs and vanadium or strain in the crystal structure due to interface mismatch [35, 117]. As the thermal expansion coefficient of vanadium is larger than that of InAs [109, 118], in the case of the cold deposition (V1), the effect from thermal expansion upon returning to room temperature after growth would make the nanowires bend away from the vanadium. Thus, the lattice mismatch at the interface is likely the main contributor to the observed strain. The strain was visible as bending contours in TEM micrographs (Fig. 3.21**c, e**) in V-coated nanowire segments.

The nanowires had WZ $(11\bar{2}0)$, type II facets [119], atypical for InAs nanowires grown under these conditions [78][2]. The vanadium shell, by contrast, showed an overall polycrystalline, granular thin film morphology, as seen in Fig. 3.21**e**. The film exhibited a glancing near columnar structure [102], similar to that reported for InAs/Nb hybrids in Ref. [53].

Insights into the V/InAs interface and the crystallographic properties of the hybrid nanowire crystal were obtained by detailed Transmission Electron Microscopy (TEM) analysis, using the JEOL 3000F microscope operated at 300 kV. Figure 3.22 shows the hybrid crystal morphology at higher magnification with resolved atomic lattice fringes in the InAs nanowire and the vanadium shell. Interplanar distances and angles of the vanadium lattice fringes were used to characterise the vanadium to be crystallised in the bulk BCC ($Im3m$) phase [109]. The grains resolved in Fig. 3.22**a** exhibited orthogonal $\{110\}$ planes, consistent with $\langle 100\rangle$ BCC zone-axes. We ascribe the bright and dark regions on the length scale of ~ 5 nm across the image to the presence of overlapping nanoscale crystalline grains with different orientations as these large scale fringes, Moiré fringes, usually are signatures of polycrystalline films with translational displacement or rotational variation amongst overlapping grains of the same lattice [63]. SAD signal (insert of Fig. 3.22**a**) from a ~ 800 nm long segment confirmed the polycrystalline morphology since no single vanadium-related diffraction pattern was visible. Rather, a continuous ring from $\{110\}$ vanadium planes was visible due to a large number of differently oriented grains. Some grains have common orientations indicated by distinct peaks in the ring (black circles).

The grain sizes, which ranged from $\sim$2 nm up to approx. 21 nm – i.e. close to the film thickness – were estimated from 33 HRTEM images and varied with the deposition temperature. The grain structure of vanadium films grown on nanowires was expected to depend on temperature for several reasons. Firstly, the initial stage of growth yields clusters with sizes and spacings that depend on the surface adatom diffusion length, which in turn depends on temperature. For two vanadium depositions on similar nanowire facets with the same deposition rate but at different substrate temperatures, it was expected that the lowest substrate temperature would produce the smallest initial average cluster size. The orientation of the individual clusters is determined mainly by the minimization of surface energy, V/InAs interface energy, and strain energy contributions to the overall excess energy. In the subsequent surface driven reconstruction stage a kinetically limited coalescence process can

[2]After a bake out of the MBE system, type I facets were produced again under similar growth conditions. The change between nanowire growth with type I and type II facets was likely related to the presence of Sb in the MBE chamber [120]. Vanadium was not deposited onto type I facets in this study.

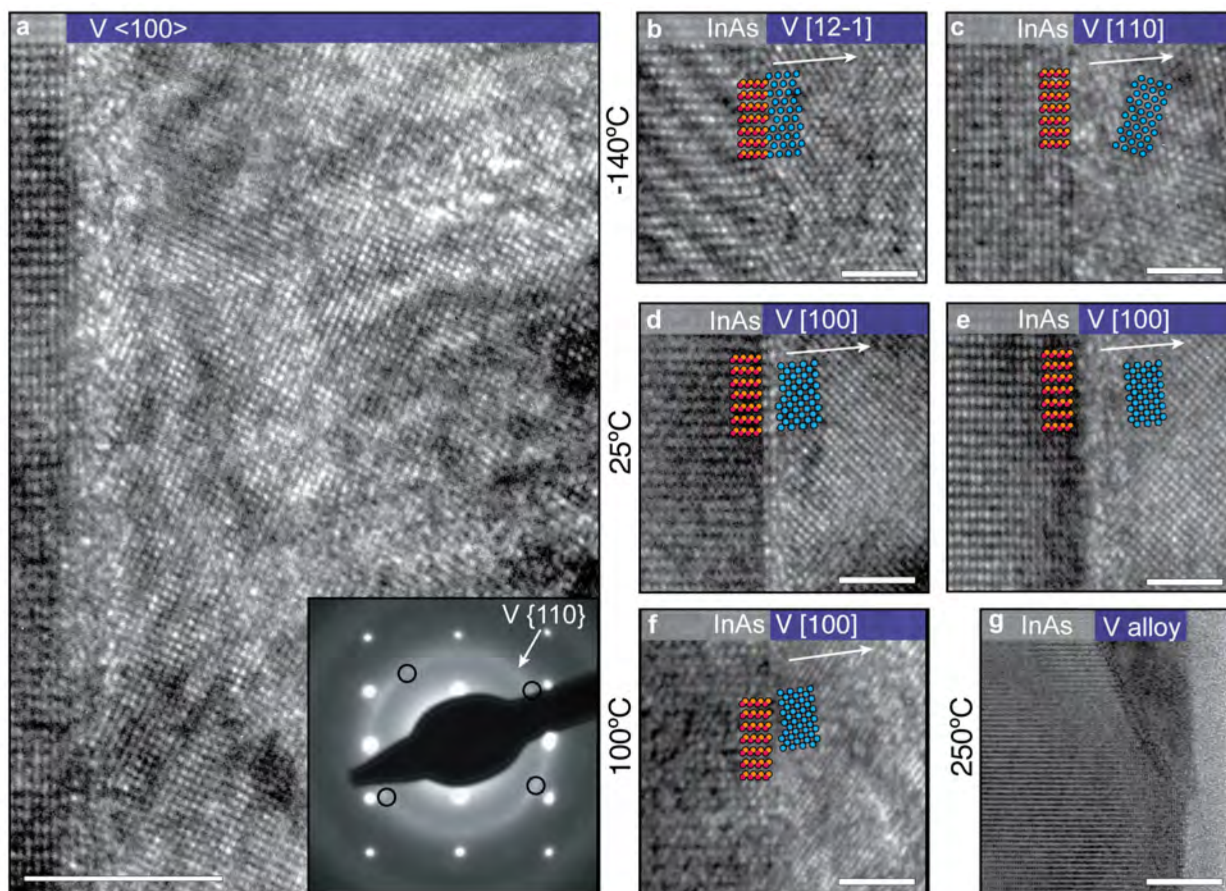

Figure 3.22: **Transmission electron micrographs of the V/InAs interfaces from vanadium deposition at various substrate temperatures. a** HRTEM showing the V/InAs interface. Lattice fringes in the vanadium are visible as well as Moiré fringes, indicating the overlap of multiple grains. Insert: SAD signal from region around **a**, showing the bi-crystal overlapping of the InAs $[1\bar{1}00]$ zone axis and vanadium. The arrow indicates the diffraction ring signal from the family of (110) planes of polycrystalline BCC vanadium. The ring features peaks (black circles) from grains with common orientations **b, c** Examples of the resulting interface for deposition at $T_\mathrm{S} = -150°\mathrm{C}$ (V1). **d, e** Examples of the resulting interface for films deposited at room temperature (V2). **f, g** Examples of the resulting interface when heating the substrate to 100°C (V4) and 250°C (V5), respectively. In the -150°C–100°C range, the hybrids had regions both with (**b,d,f**) and without (**c,e**) crystalline interfaces. **g** For deposition at at 250°C the InAs and vanadium reacted. Coloured dots provide a guide to the crystal structure. White arrows indicate the locally observed direction closest to the out-of-plane direction, labelled in the top bar. All images were acquired with alignment parallel to a InAs $[1\bar{1}00]$ zone axis). Scale bars: **a**: 5 nm, **b-f**: 2 nm **g**: 10 nm.

occur [78, 102]. The result is strongly dependent on the initial cluster sizes, cluster-cluster orientations, binding-strength and temperature. Finally, in some cases, the thermodynamical driving forces change as function of shell thickness and an additional re-crystallization of the vanadium film may occur. However, the films investigated here had grain sizes that were smaller than the film thickness. This means that re-crystallization was unlikely to occur, and the variation of film thickness likely had little to no impact on the structural properties. For a full description of the above processes see Ref. [78].

A comparison of the V/InAs interfaces obtained for the 4 different deposition temperatures is given in Figs. 3.22**b-g**. The coloured circles provide a guide to the observed crystal zone-axis orientation, and the white arrows indicate the locally observed low-index direction closest to the out-of-plane direction indicated in the top bar. Interestingly, the crystalline vanadium grains always grew with particular crystal planes parallel to the (1$\bar{1}$00) planes of the nanowire. However, no typical match along the nanowire (0002) axial planes (i.e. the growth planes) was apparent and therefore also no typical out-of-plane grain growth direction was observed. The planes parallel to the (1$\bar{1}$00) crystal planes appeared to change with increasing temperature being $\{111\}$ in the cold deposition V1 (Figs 3.22**b, c**) and $\{100\}$ for V2-V4 (Figs. 3.22**d, e**). Figures 3.22**b, c** and 3.22**d, e** exemplify the observed variation in out-of-plane direction. Depending on the local grain morphology, the [111] zone axis was also observed in the V2-V4 on rare occasions, but [100] dominated. A common feature of the vanadium hybrids from all deposition temperatures in this study was the absence of a coherent crystal lattice match at the V/InAs interface. While some of the crystalline grains grew from the InAs interface (Figs 3.22**b, d, f**), the most commonly observed growth mode was the initial formation of a polycrystalline interfacial layer without epitaxial match to the InAs from which other crystalline vanadium grains nucleated and grew (Figs 3.22**c, e**). Such polycrystalline interface morphology is consistent with the ring-formed $\{110\}$ diffraction signal found in Fig. 3.21. The most abundant grain sizes observed ($> 65\%$) were in the 6-12 nm range for $T_{\mathrm{S}} = 25°$C room temperature deposition (V2) while it was 11-17 nm for the cold $T_{\mathrm{S}} = -150°$C deposition (V1). For deposition at $T_{\mathrm{S}} = 100°$C (V4), the grain sizes were evenly distributed and ranged from 5-12 nm (i.e. up to the entire film thickness).

Depositing vanadium with a substrate temperature of $T_{\mathrm{S}} = 250°$C (V5) resulted in a reaction between the vanadium and InAs nanowire (Fig. 3.22**g**). The nanowires developed indentations where the InAs was replaced by an alloy. From HRTEM analysis it was found that this alloy had a face-centred cubic crystal phase with lattice constant $a = 4.7 \pm 0.1$ Å. One possible alloy that matches these properties is AsV_3 [121]. However, properly determining the composition of the alloy would require electron energy loss spectroscopy, energy-dispersive x-ray spectroscopy or other x-ray techniques. An in-depth study of the alloy was not performed, since the general morphology with the indentations was unsuitable for making semiconductor-superconductor hybrid devices. Further it was expected that the alloying was determined mainly by the substrate temperature and would occur regardless of film thickness [122]. Therefore, no more depositions at $T_{\mathrm{S}} = 250°$C were performed.

3.4.3 Electrical characterisation

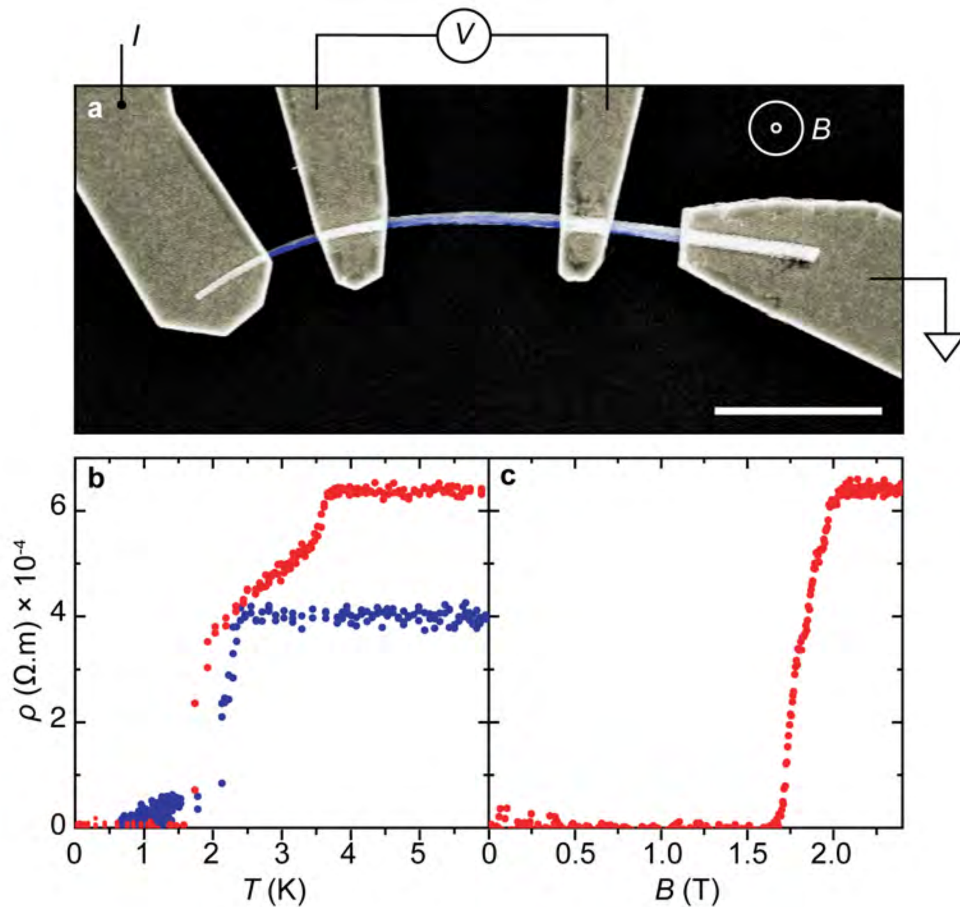

Figure 3.23: **Four terminal measurements of V/InAs hybrids. a** False-coloured SEM of a four terminal V/InAs device with Ti/Au ohmic contacts (gold) to the vanadium (blue). Scale bar represents 2 μm. **b** Resistivity ρ vs. temperature T showing superconducting transitions for two example devices, one with RT vanadium deposition (red) and the other with a cooled substrate holder $T_\mathrm{S} = -150°\mathrm{C}$ (blue). **c** Resistivity ρ vs. out-of-plane magnetic field B for the RT V/InAs device.

The superconducting properties of the V/InAs hybrids were studied using four terminal devices such as that shown in Fig. 3.23. Contacting the nanowire device in this way was aimed at determining how the crystal structure and morphology impacted the electrical properties of the vanadium. Device dimensions used for the resistivity calculation were measured from scanning electron micrographs of each device.

Resistivity, ρ, as a function of temperature for two representative devices is shown in Fig. 3.23**b**. Red and blue data points are from different devices fabricated from V3 and V1, respectively, with the vanadium deposited at $T_\mathrm{S} = 25°\mathrm{C}$ and $T_\mathrm{S} = -150°\mathrm{C}$. Each device exhibited a transition from the normal ($\rho = 4 - 6 \times 10^{-4}$ Ωm) to superconducting phase ($\rho = 0$). However, neither device exhibited a clear, single transition with a well defined critical temperature. Rather, the transition of these and all other measured devices was gradual and no two devices behaved identically. Additionally, 4 of the 10 measured devices showed no zero resistance state at base temperature of the cryostat ($T \sim 20$ mK). The observed behaviour can likely be explained by the grain structure observed in Figs. 3.21 and 3.22. Obtaining a single, well-defined T_C in polycrystalline superconductors relies on effective proximitisation of the insulating grain boundaries to form a series of Josephson junctions [123, 124]. This was clearly not achieved for the vanadium films studied here and therefore the following possible

explanation was proposed. For vanadium, size effects lower T_C as grain size is reduced [114, 116], and thus each grain is expected to undergo a superconducting transition at a different temperature. The smallest grains may not turn superconducting at all due to the Anderson criterion [125]. Naturally, observing a zero resistance superconducting state cannot occur if portions of the nanowire remain in the normal state, either due to a small grain size or poor proximitisation of the grain boundaries. Additionally, the particular ρ vs. T behavior would strongly depend on the exact grain configuration in the measured segment. The behavior observed in Fig. 3.23**b** is consistent with this picture, and the range of the transition region ($T = 1-4$ K) is similar to previous reports of the size-related T_C variation in vanadium thin films [114, 116]. Note that thin, two dimensional films of vanadium with a similar granular structure are more likely to exhibit 'bulk-like' superconducting properties, including a clear critical temperature. This is because the additional dimension increases the likelihood of forming a percolating pathway between superconducting grains. The reduced dimensionality of the quasi-1D nanowires limits this possibility, hence obtaining much more variable results between devices. One possibility for obtaining a higher number of superconducting devices would be to increase film thickness to be much greater than the grain size ($t_{\mathrm{V}} \gg 20$ nm), although this may further increase the nanowire bending for much thicker films.

Fig. 3.23**c** shows the response to a magnetic field applied perpendicular to the substrate, as illustrated in Fig. 3.23**a**. As expected, the value of $B_C \sim 1.8$ T exceeds the reported bulk value [110, 111, 126] due to the nanoscale morphology of the films. Even larger critical fields for B applied parallel to the nanowire are expected. Importantly, the perpendicular critical field was far greater than that reported for aluminium covered InAs nanowires [36], which is highly desirable in applications towards topological superconductivity [21, 88], superconducting qubits [48, 49] and fundamental physics [65, 127, 128]. Tunnel spectroscopy was performed in five devices featuring shadow-patterned V/InAs NWs, but no proximity-induced gap was measured. This combined with the fact that no clear, consistent critical temperature was observed showed that the films are not suitable for obtaining proximity-induced superconductivity in the InAs.

3.4.4 Conclusions and outlook

In conclusion, the structural and superconducting properties of vanadium shells on InAs nanowires were studied, motivated by a desire to understand the possibilities for forming high quality bi-crystal interfaces with materials beyond aluminium and form hybrid electronic devices based on these. To do so, vanadium was deposited at a wide range of temperatures, from liquid nitrogen cooled, $T_{\mathrm{S}} \approx -150°$C to above the point where the two materials formed an alloy, at $T_{\mathrm{S}} = 250°$C. Deposition at temperatures $-150°\mathrm{C} \leq T_{\mathrm{S}} \leq 100°$C favoured growth of grains where the vanadium (100) or (111) planes grew parallel with the underlying InAs nanowire crystal $(1\bar{1}00)$ planes. However, a typical bi-crystal interfacial match was not found along the axial direction, limiting the potential for large-scale epitaxy between the two materials. Rather, the vanadium films consisted of polycrystalline grains with diameters 2-21 nm. The wide variety of grain sizes dominated the electrical behaviour of devices fabricated from these growths. In some, but not all cases, the nanowire hybrids turned superconducting at cryogenic temperatures, and exhibited a higher critical magnetic field than aluminium-based hybrids with similar film thickness. The gradual nature of the transition to the superconducting state and the device-to-device variation was consistent with the films consisting of a large number of small grains with varying size. This is because the critical temperature of each grain is expected to decrease with decreasing grain size [123]. Observation of an induced superconducting gap in future hybrids will likely depend on achieving

films with a well-defined, macroscopic T_C. This encourages further optimisation towards entirely crystalline, epitaxially matched vanadium/semiconductor hybrids. Doing so would likely involve substrate temperatures between 100°C and 250°C (or above) during vanadium deposition to promote formation of larger crystalline grains, which may exhibit a more well-defined collective T_C. Deposition at such temperatures may require a different semiconductor nanowire material, since we found alloying occurred for $T_{\mathrm{S}} = 250°\mathrm{C}$. Alternatively, other semiconductor materials may have more favourable surface energy configurations for vanadium growth at lower temperatures. Finally, an intermediate crystalline layer could be grown on the InAs prior to vanadium deposition, such that an epitaxial match would be possible between each layer.

3.5 Ta/InAs hybrid nanowires

The contents of this section is largely based on the manuscript of Pub. B.

Tantalum is a type I superconductor with $T_C = 4.48$ K which in bulk crystallises with a body-centred cubic (bcc) crystal structure, also known as the α-phase [104, 109, 129]. In thin films, tantalum is also known to exist in other allotropes; tetragonal (β-phase) [130], and face-centred cubic (fcc) [131, 132, 133]. Relatively large grains (10–20 nm in diameter) of tantalum can also exist with an hcp structure [132]. A critical temperature in nanocrystalline pure α-phase tantalum has been found to persist even down to grain sizes of 2.6 nm ($T_C = 0.9$ K), 40% below the Anderson limit [124], while lower critical temperatures has been reported for very thin amorphous tantalum ($t = 3.5$ nm, $T_C = 0.6$ K)[134].

3.5.1 Sample descriptions

Three InAs NW samples were grown using the "*in-situ* Au" growth scheme in substrates featuring lithographically defined etched trenches (Sec. 3.1.7). Tantalum was deposited along the $[11\bar{2}]$ substrate orientation with a rate of ~ 1 Å/s and at an angle of $\theta = 28°$ with respect to the substrate surface plane. This ensured continuous 3-facet shells on each nanowire, with little or no effects of shadowing from neighbouring nanowires for an average inter-wire pitch > 5 μm. This angle of evaporation did, however, enable the trenches to mask the lower part of some nanowires grown inside the etched trenches as demonstrated in Fig. 3.24. Three growths (samples T1-T3) were performed with different tantalum deposition conditions and film thicknesses as listed in Table 3.5. Two different tantalum film thicknesses were tested such that the measured thicknesses ranged from 20-30 nm. One sample, T2, was heated to $T_{\mathrm{S}} = 180$°C during deposition in an attempt to increase the adatom surface diffusion. In an attempt to protect the tantalum from subsequent oxidation when leaving the MBE system, sample T3 was capped with an 30 nm full shell of amorphous AlO_x deposited by e-beam evaporation immediately after the tantalum deposition. Additionally, two InAs (111)B samples ($\mathrm{T}^{\mathrm{Bulk}}$1-2) had tantalum thin films deposited directly on the bulk surface in the metallisation chamber after degassing the surfaces in the MBE. These served as thin film references for nanowire measurements.

	T_{S}(°C)	t_{Ta} (nm)
T1	25	20
T2	180	20†
T3	25	30*
$\mathrm{T}^{\mathrm{Bulk}}$1	25	20
$\mathrm{T}^{\mathrm{Bulk}}$2	25	100

,

Table 3.5: Overview of tantalum deposition temperatures T_{S} (thermocouple) and tantalum film thicknesses t_{Ta} for the three nanowire growths T1-T3. Sample marked with * had an additional 30 nm AlO_x full shell cap. The film thicknesses of T1 and T3 were measured from transmission electron micrographs with one of the two Ta-covered nanowire facets aligned parallel to the electron beam. Film thickness marked with † was the nominal thickness as recorded by the quartz crystal monitor, as the actual film thickness on the wire could not be measured in this case due to degradation.

3.5.2 Structural characterisation

Resulting Ta/InAs hybrid nanowires from samples T1 are displayed in Fig. 3.24. Fig. 3.24**a-b** shows SEMs of the hybrids after nanowire growth and subsequent tantalum deposition at room temperature (sample T1). The

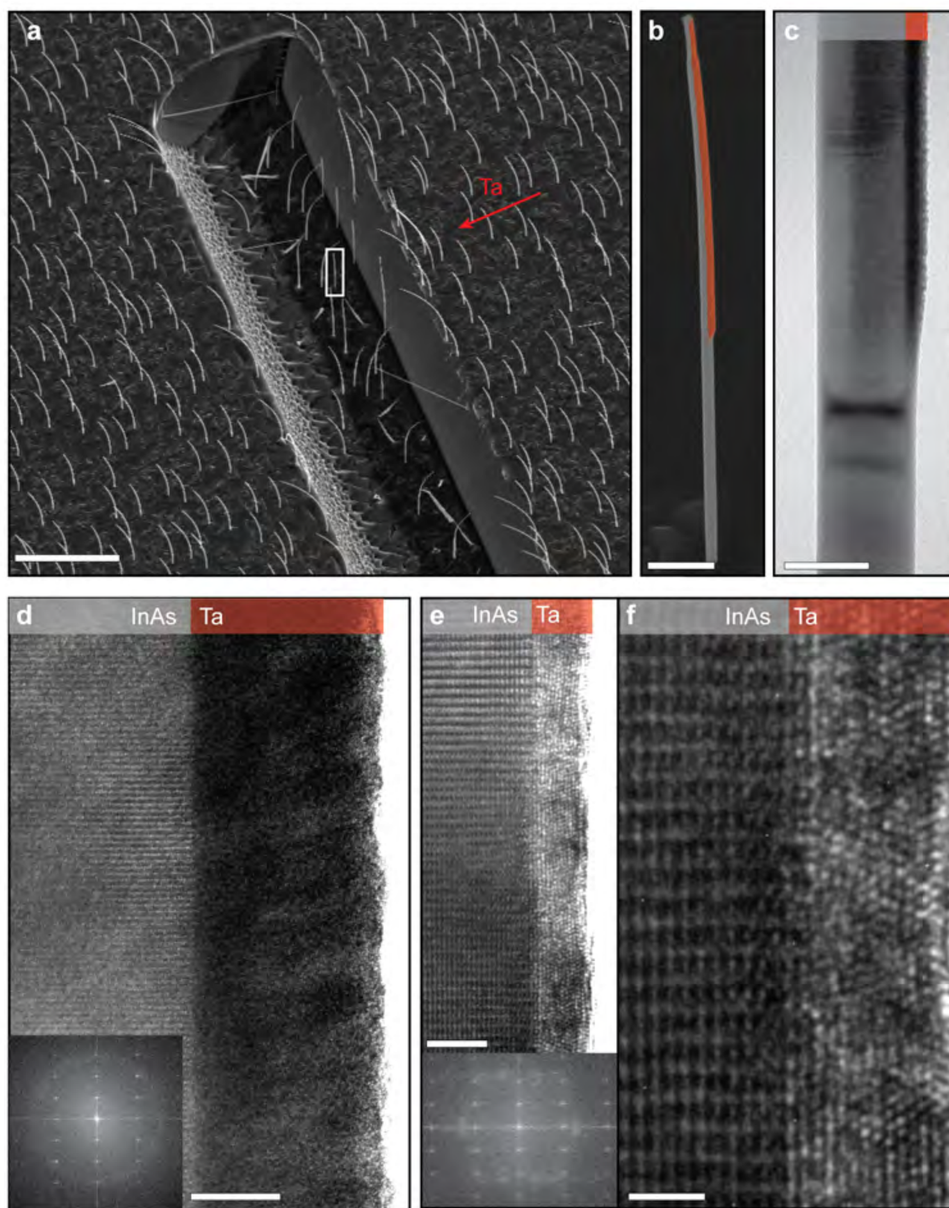

Figure 3.24: **Structural characterisation of Ta/InAs hybrids by electron microscopy.** **a** SEM showing as-grown Ta/InAs nanowires on the surface (sample T1). The direction of tantalum evaporation is indicated by the red arrow. The nanowires are bent away from the tantalum shells. The white frame indicates the nanowire hybrid magnified in **b**. **c** Low-resolution TEM taken at the junction of a half shadowed Ta/InAs hybrid nanowire. **d** HRTEM the interface between an InAs nanowire facet and a 20 nm tantalum layer evaporated at room temperature. Tantalum exhibited a glancing column-like structure. Insert: FFT of the HRTEM showing the periodic InAs peaks from the crystalline nanowire encircled by a diffuse ring signal from the amorphous tantalum. **e** HRTEM showing the interface between an InAs nanowire and a 5 nm layer of tantalum. The nanocrystalline structure of tantalum was visible by lattice fringes, magnified in **f**. Insert: FFT of HRTEM showing the sharp InAs peaks and diffuse but localised signal from tantalum lattice fringes. Scale bars: **a**:10 μm. **b**: 500 nm. **c**: 100 nm. **d**: 10 nm. **e**: 5 nm. **f**: 2 nm.

red arrow indicates the direction of the evaporated tantalum. The nanowires were bent away from the tantalum shell, unlike the V/InAs hybrids which were bent toward the vanadium. The masked wires were not (or only slightly) bent, and so the nanowire bending was likely to arise from the tantalum shells. The higher thermal expansion

In low-resolution TEM (Fig. 3.24**c**) the overall morphology of the tantalum shells was continuous but granular on the InAs nanowire facets when evaporated at room temperature. Similarly to vanadium, the tantalum shells exhibited a glancing column-like structure [102]. Elevating the substrate temperature to 180°C during evaporation (T2) resulted in degradation of the nanowires as tantalum reacted with the InAs at this temperature. The InAs nanowires were wurtzite crystalline with type I $\{1\bar{1}00\}$ facets, and therefore the nanowires were aligned to $\langle 2\bar{1}\bar{1}0\rangle$ zone-axes for characterising the hybrid interface. Studying the hybrids using HRTEM (Fig. 3.24**d-f**) confirmed a granular morphology in tantalum and revealed it to be amorphous/nanocrystalline. Unlike vanadium, crystal grains were not clearly visible in HRTEM of 20 nm thick films (Fig. 3.24**d**, T1), suggesting a typical grain size $\ll t_{\mathrm{Ta}}$. Further evidence for this was found by imaging a nanowire from growth T1 which featured a 5 nm parasitic growth layer on one of the facets (Fig. 3.24**e-f**). Here, lattice fringes from nanocrystalline grains were visible, and measurements of interplanar spacings and lattice fringe angle indicated a cubic lattice parameter of $a = 4.3\pm0.3$ Å. This value is within the margin of error for FCC tantalum ($a = 4.42$ Å)[133], and far from the lattice constant for the BCC phase ($a = 3.3$ Å). The level of nano-grain rotational disorder in the film was assessed from an FFT of the TEM (insert of Fig. 3.24**e**), where Ta related peaks were localised, but too scattered to determine an overall zone-axis for the grains. Tantalum may initially have formed FCC grains on the nanowire surface and with increasing film thickness formed a glancing columnar structure, like reported in Ref. [133].

3.5.3 Electrical characterisation

Low temperature transport experiments on nanowires from growth T1 were performed on five devices (DT1-DT5) to characterise the superconducting properties of the Ta-based hybrids. The length of the nanowires ($\sim 10-15$ μm) allowed for tunnelling spectroscopy and four terminal measurements to be performed on the same nanowire, as shown in Fig. 3.25**a**. Four terminal measurements on nanowires and bulk films were performed with the circuitry illustrated in Figs. 3.25**b** and 3.25**c** to determine the basic superconducting properties of our nanoscale Ta films. We find a critical perpendicular field for the nanowire, $B_{\mathrm{C}\perp}^{\mathrm{Ta}} \sim 3.5$ T, which is over an order of magnitude higher than that reported for Al/InAs hybrid wires with similar dimensions, $B_{\mathrm{C}\perp}^{\mathrm{Al}} \sim 0.1$ T.

The temperature dependence of the four terminal resistance in a nanowire device as well as the the bulk samples is shown in Fig. 3.25**e**. The critical temperature of the nanowire device $T_{\mathrm{C}}^{\mathrm{Ta}} = 0.7$ K was consistent with that of the bulk film of matching thickness, while the thicker 100 nm film had $T_{\mathrm{C}} \sim 2.5$ K. A dependence of T_C on film thickness was expected [129], but T_C was lower than $T_C = 0.9$ K reported for 2.4 nm pure-phase nanocrystalline tantalum [124].

The induced superconducting properties were probed via tunnel spectroscopy on the half-shadowed segment of the Ta/InAs nanowires (Fig. 3.26). A false-colored SEM of a tunnel-spectroscopy device is shown in Fig 3.26**a** along with a device schematic. Shown in Fig. 3.26**a**, all five Ta/InAs devices exhibited an induced superconducting energy gap with coherence peaks at $V_{\mathrm{sd}} = \pm\Delta/e = \pm0.13$ mV. The measured gap, $\Delta^{\mathrm{Ta}} = 0.13$ meV matches the T_{C} for 20 nm films shown in Fig. 3.25. Bound states in the superconducting gap were evident, similar to those observed in the Al/InAs hybrids. Line traces of G/G_{N} vs. V_{sd} (where G_{N} is the out-of-gap

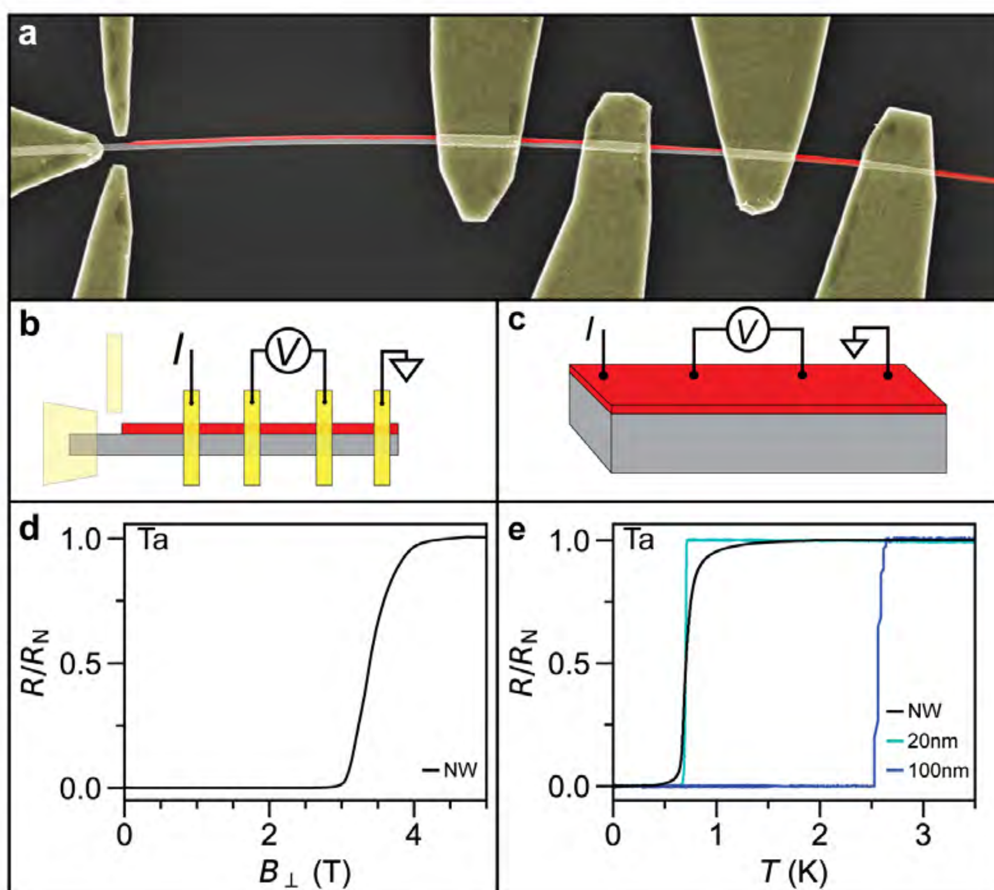

Figure 3.25: **Low temperature four terminal measurements of Ta/InAs hybrid nanowires and bulk substrates. a** False-color SEM of a tantalum (red) hybrid nanowire device with Ti/Au contacts (gold). The device was used for both tunnelling spectroscopy (left side) and four point resistance measurements (right side) as shown in the device schematic (**b**). **c** Schematic of four point measurement on bulk substrates. **d** Measurement of resistance R, normalised with respect to the resistance at 5 T, R_N, versus applied perpendicular magnetic field for the Ta/InAs nanowire. The 20 nm thick nanowire thin film exhibited a perpendicular critical field $B_\mathrm{C} \sim 3.5$ T. **e** R/R_N versus temperature for nanowires and bulk substrates coated by tantalum. The nanowire device (black curve) exhibited a critical temperature of $T_\mathrm{C} \sim 0.7$ K and the 20 nm (light blue) and 100 nm (dark blue) thick thin films on bulk substrates had $T_\mathrm{C} \sim 0.7$ and 2.5 K, respectively.

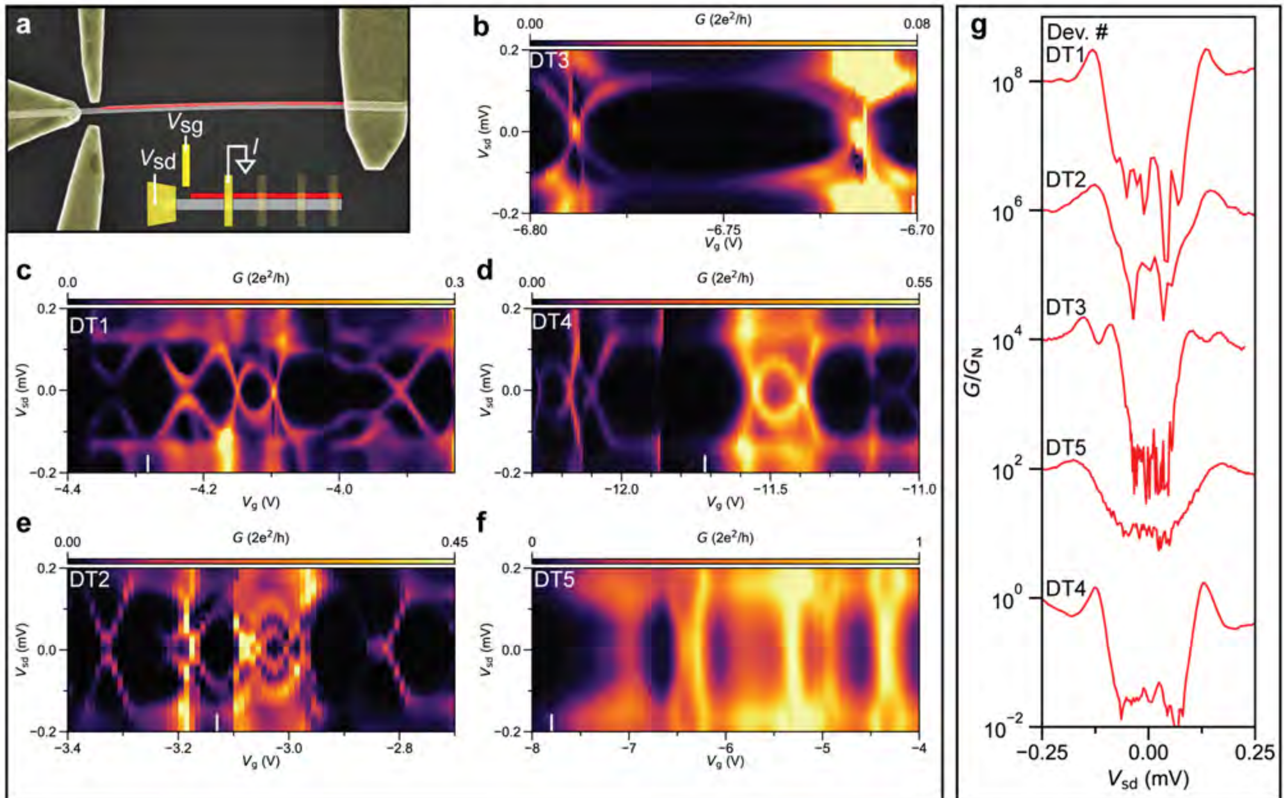

Figure 3.26: **Low temperature tunnelling spectroscopy of Ta/InAs hybrid devices. a** False-colour SEM of a Ta/InAs nanowire contacted for tunnel spectroscopy (schematic inserted). **b-f** Bias spectra, with measured differential conductance, G, plotted as a function of source-drain bias V_{sd} and gate voltage V_{g}, for five devices DT1-DT5 are shown, each one exhibiting proximity-induced superconductivity in the hybrid nanowires. **g** Line traces of G normalised to the out-of-gap conductance G_{N} as a function V_{sd} from the gate voltages indicated by white lines in **a**. The traces were vertically offset by two decades. Gap hardness, $G_{\mathrm{N}}/G_{\mathrm{S}}$, was found to be $50 - 100$ for devices DT1-DT4 and ~ 10 for DT5.

conductance $G(V_{\rm sd} = -0.25 \text{ mV})$) from the five spectra are plotted in Fig.3.26**b** with gate voltage positions marked in the spectra by white lines. The traces were vertically offset by two decades. Devices D1-D4 exhibited hard gaps with values $G_{\rm N}/G_{\rm S} = 50 - 100$ (where $G_{\rm S} = G(V_{\rm sd} = 0 \text{ mV})$), persisting over a wide $V_{\rm g}$ range, similar to that seen for Al/InAs hybrids. D5 exhibited were more broadened features and a lower gap hardness of ~ 10, which may have been caused by a less well-defined tunnel barrier by e.g. contaminating resist residue.

3.5.4 Conclusions and outlook

Since the Ta was nanocrystalline (Fig. 3.24) but nevertheless produced a hard proximity-induced superconducting gap, these results showed that the atomic registry of epitaxial interfaces is not a prerequisite for hard gap superconductivity. Rather, an impurity-free, uniform interface is sufficient if the thin film itself supports well-defined superconductivity, unlike observed for e.g. the vanadium films in Sec. 3.4. The hard gap, bound sub-gap states and high critical field potentially makes the Ta/InAs hybrids attractive for studies of topological superconductivity. Increasing the Ta film thickness on the nanowires would likely result in a higher T_C, as observed for the 100 nm bulk sample.

3.6 Nb/InAs hybrid nanowires

The contents of this section is largely based on the manuscript of Pub. B.
The final InAs nanowire hybrid combination studied was Nb/InAs. The technological importance of niobium based-superconductors – owing to their high $T_C \sim 9$ K and high critical magnetic fields – has motivated many previous efforts to incorporate them in *ex-situ* fabricated hybrid nano-devices [21, 33, 40, 54, 135]. The shadow lithography developed here enabled *in-situ* Nb/InAs devices previously impossible due to lack of selective process techniques. Niobium crystallises predominantly with a BCC structure [109]. Planar epitaxy between InAs(001) and Nb(001) has been observed for MBE grown films at 200°C ($T_C = 8.6$ K) [136], however this substrate temperature was found incompatible with Nb deposition on InAs nanowires [53]. Electrical investigations showed, however, that polycrystalline Nb growth at $T = 50$°C did not strongly affect the superconducting properties compared to the single crystalline film grown at $T = 200$°C, as T_C remained 8.6 K [136].

3.6.1 Sample descriptions

Three Nb/InAs samples, N1-N3, were grown on single-sided shadow mask substrates using the "EBL Au" NW growth scheme (Sec.3.1.7). After growth, niobium was deposited along the $[1\bar{1}0]$ direction with $\theta = 10°$. The thickness, t_{Nb}, and substrate deposition temperature T_{S} for each sample are listed in Table 3.6.

	T_{S} (°C)	t_{Nb} (nm)
N1	25	48
N2	-150	20
N3	25	30*

Table 3.6: Overview of niobium deposition temperatures T_{S} and niobium film thicknesses t_{Nb} for the three InAs nanowire growths N1-N3. Sample N3 marked with * had an additional 30 nm AlO_x full shell cap. The film thicknesses were measured from transmission electron micrographs.

3.6.2 Structural characterisation

Figure 3.27**a** shows a false-colored SEM of a niobium coated (purple) hybrid nanowire from sample N2 grown proximal to a wide SiOx segment (blue) shadowing the lower part of the nanowire during evaporation. The niobium formed a smooth, continuous film on the nanowire, as seen in 3.27**b** (magnified SEM) and 3.27**c** (low-resolution TEM). A similar morphology was found from depositing niobium at room temperature (N1). At higher TEM magnification of a Nb/InAs corner interface (InAs $[1\bar{1}00]$ zone-axis) (Fig.3.27**d**), a column-like grain structure from the nanowire was evident, similar to that observed for V/InAs and Ta/InAs and previous reports on Nb/InAs [53]. SAD confirmed an overall nanocrystalline morphology by the presence of Debye-Scherrer rings overlaying a regular grid of crystalline InAs Bragg peaks from a $\langle 1\bar{1}00 \rangle$ (Fig. 3.27**e**).

3.6.3 Electrical characterisation

Low temperature transport experiments on wires was performed to characterise the superconducting properties of the Nb-based hybrids. Devices for tunnelling spectroscopy (Sec. 2.2.2) was fabricated, as shown in Fig. 3.28**a-b**. Nb/InAs devices showed 'soft gap' induced superconductivity seen in the bias spectra (Fig. 3.28**c**) in the form of a superconducting energy gap with coherence peaks at $V_{\mathrm{sd}} = \pm\Delta/e = \pm 0.2$ mV and a continuum

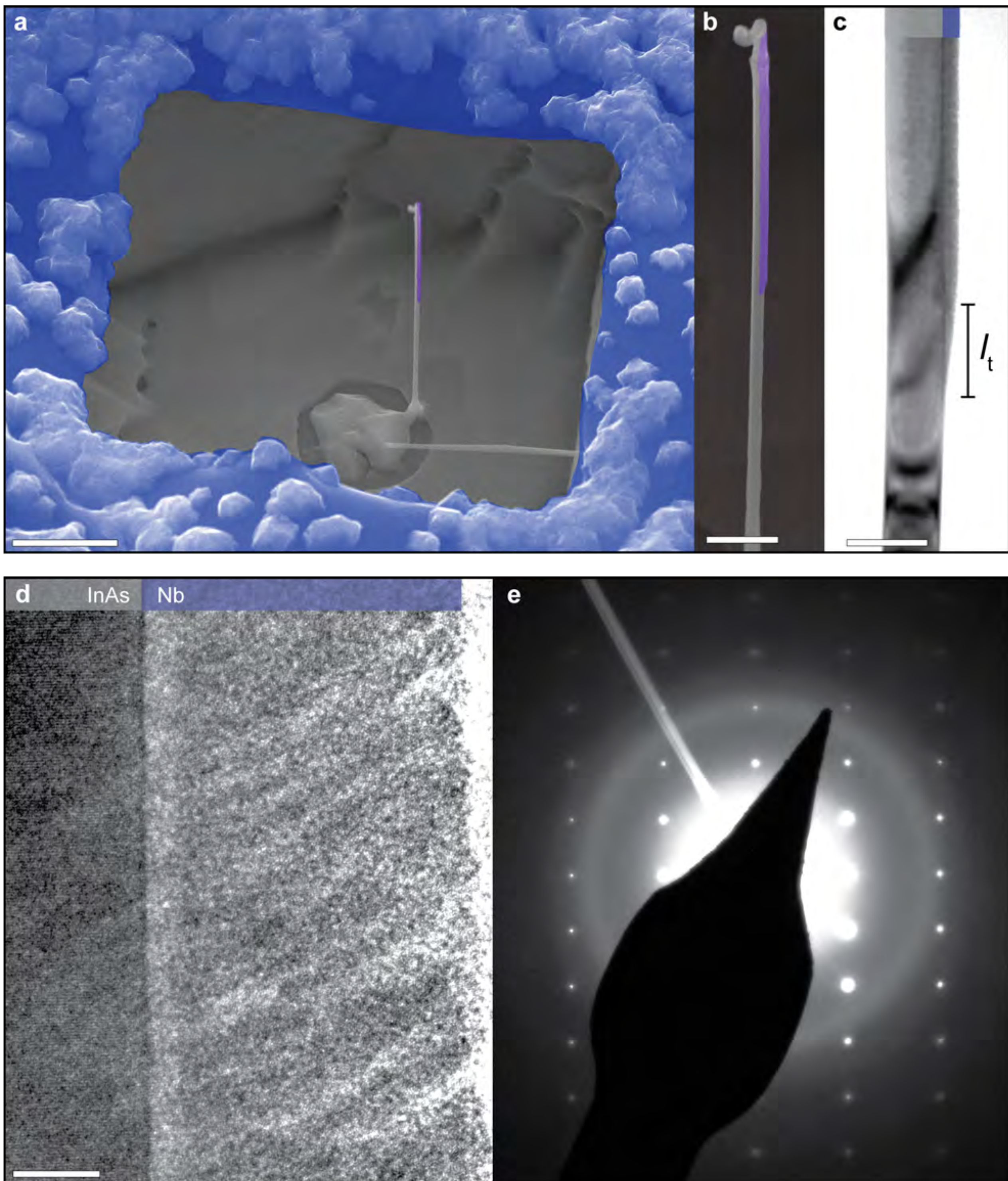

Figure 3.27: **Electron microscopy of Nb/InAs hybrids.** **a-b** False-color SEMs of InAs nanowire partially coated by Nb (purple) grown in a SiOx shadow mask (blue). **c** TEM of the Nb/InAs by the Nb-film transition l_t from coated to non-coated. **d** HRTEM showing the Nb interface to a nanowire corner. **e** SAD signal from a $\sim 1\mu$m Nb/InAs segment. Scale bars: **a**: 2 μm, **b**: 500 nm, **c**: 100 nm, **d**: 10 nm.

of sub-gap states. In the tunnelling regime, $V_g \leq -12.5$ V, conductance suppression was clearly observed for $eV_{sd} < |\Delta| \sim 0.2$ meV in Fig. 3.28**e**, albeit with relatively low hardness ($G_N/G_S \sim 3$). Figures 3.28**d** present G vs. V_{sg} line-traces for $V_{sd} = 0$ and $V_{sd} = 0.5$, marked in the bias spectrum by colored lines. Upon increasing V_{sg} from pinch-off, the conductance for $V_{sd} = 0.5$ mV $>$ Δ increased in steps of $0.7 \times 2e^2/h$ and shows a doubling at the plateaus for $V_{sd} = 0$. This is consistent with a near ballistic QPC junction and near perfect transmission at the contacts [39, 54, 55, 137, 138, 139].

The soft superconducting gap for these *in-situ* Nb/InAs hybrids was unlikely caused by contaminated or process-damaged interfaces considering the near ballistic device characteristic, high contact transmission, and given the excellent gap hardness achieved in Al/InAs and Ta/InAs shadow devices. Rather, native oxides of niobium could provide an explanation. Niobium oxides can be superconducting with lower $T_C \sim 2$ K, metallic, or magnetic [140, 141]; each of these effects leads to soft-gap superconductivity in thin niobium films. Oxidation of the niobium shell was consistent with the observed nanocrystalline morphology. Using *in-situ* surface passivation of Nb hybrids would likely provide insights into how the surface impacts gap properties. This was attempted with growth N3 using *in-situ* evaporated AlOx. However, the AlOx was very granular and non-continuous, potentially containing a substantial amount of pin-holes. Ultimately it did not effectively passivate the Nb surface, since tunnel spectroscopy devices fabricated from AlOx-coated Nb/InAs hybrids also exhibited a soft gap.

3.6.4 Conclusions and outlook

E-beam evaporation of niobium was compatible with the shadow lithography platform, patterning a smooth Nb film on the nanowire surface. Electron diffraction and high resolution imaging showed a polycrystalline film structure, consistent with previous reports. Devices for tunnel spectroscopy reflected a near ballistic, high contact transmission, albeit with a soft induced superconducting gap likely arising from a formed Nb-oxide. An attempt was made to passivate the Nb surface by e-beam evaporated AlOx but the granular and non-continuous AlOx did ultimately not protect the Nb. An *in-situ* coating with ALD AlOx or HfOx could provide a way protect the Nb against oxidation in future experiments.

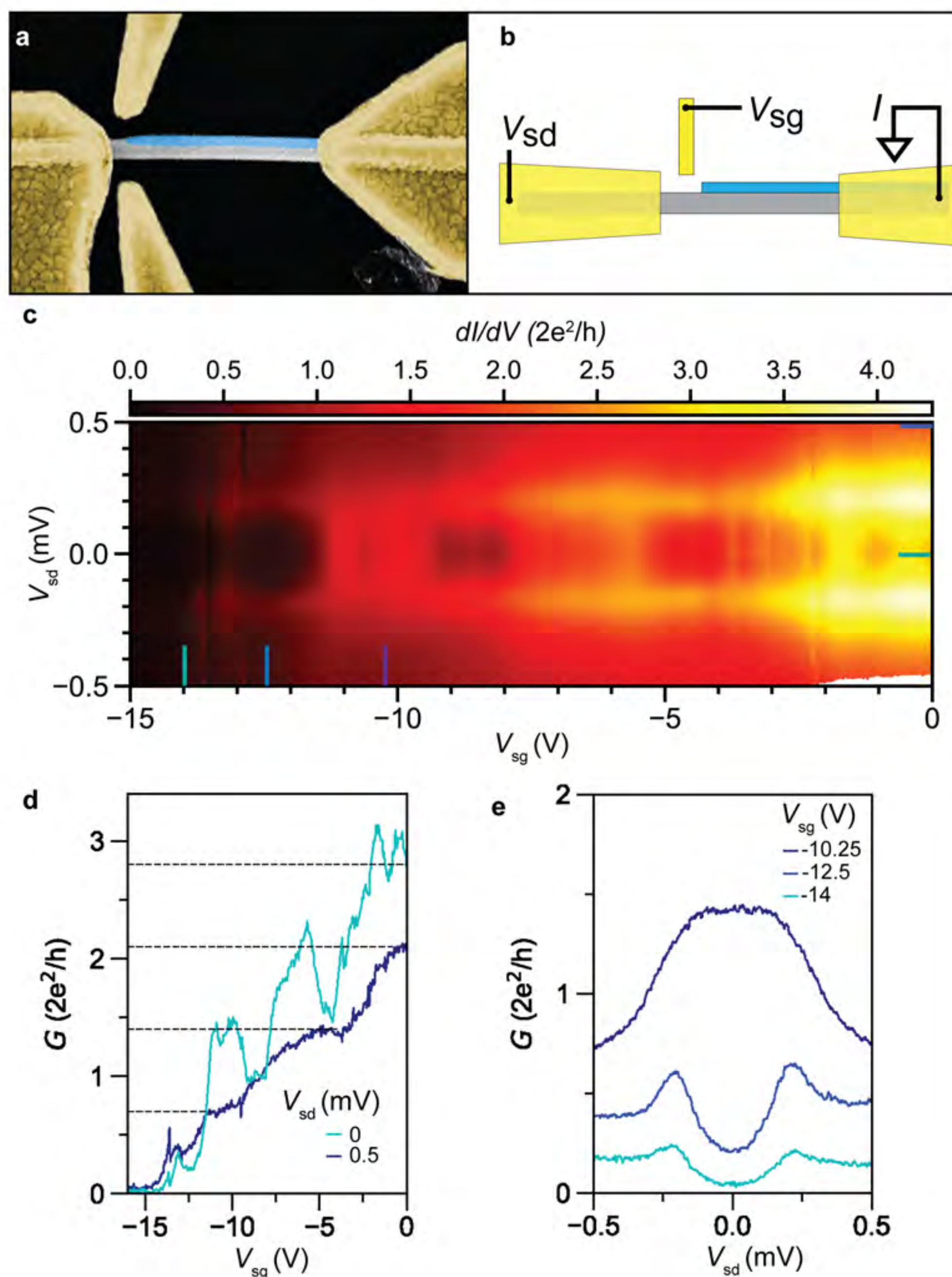

Figure 3.28: **Low temperature spectroscopy of a Nb/InAs hybrid. a** False-colored SEM of Nb/InAs hybrid nanowire device for tunnelling spectroscopy. The niobium (purple) was shadow masked during evaporation, creating bare InAs segment for contacting the semiconducting nanowire. **b** The device schematic for tunnelling spectroscopy. **d** Differential conductance G vs. side gate voltage $V_{\rm sg}$ for a Nb/InAs device exhibiting conductance plateaus for $V_{\rm sd} = 0.5$ mV $> \Delta$ at multiples of $0.7 \times 2e^2/h$ (dashed lines), and conductance doubling in the superconducting state, $V_{\rm sd} = 0$. **e**, G vs. $V_{\rm sd}$ shows conductance doubling on the first plateau at $V_{\rm g} = -10.25$ V, and a soft gap in the tunnelling regime, $V_{\rm g} = -12.5, -14$ V. Contact resistance $R_{\rm C} = 3.2$ kΩ was subtracted from the data in **d-e**.

Chapter 4

Conclusions and outlook

Superconductor/semiconductor hybrid devices form the backbone of many electronic implementations of quantum information ranging from topological qubits, gatable transmon devices and Andreev qubits [30, 44, 45, 46, 47, 48, 49, 51, 50, 66, 67, 68]. The shadow mask platform presented in this thesis removes previous restrictions on the possible material combinations, and obviates the most damaging fabrication steps, thus providing a clear enhancement of device quality and functionality. Eliminating post-process chemical etching increased spectroscopic device yield (5 out of 5 for Al/InAs and Ta/InAs devices), enabled ballistic superconductivity in Nb/InAs devices, and enhanced electrostatic stability by an order of magnitude in Al/InAs Majorana island devices. High yield and large-range, hysteresis-free device operation are crucial metrics for future advanced circuitry incorporating a large number of hybrid elements as well as any adaptation of automatic tuning procedures like those currently under development for spin-qubit devices [92].

Shadow mask geometries featuring masks at multiple azimuthal angles around the nanowire enabled demonstrations of multi-hybrid nanowires with different patterned shell materials as well as patterned full-shell geometries, not previously achieved using shadowing techniques. The demonstrated stability in shadow-patterned devices combined with the full-shell geometries is a promising route for improving e.g. Josephson junctions for Andreev qubits [142, 143, 144] or studies of flux-induced Majorana zero-modes in full-shell islands [71]. The platform furthermore allows for functional devices to be encapsulated *in-situ* with passivating dielectrics, thus protecting sensitive elements which may be crucial for implementations of e.g. high T_C Nb-based superconductors. While developed for nanowire growth using molecular beam epitaxy, growth of nanowires in the platform is also demonstrated using chemical beam epitaxy. This may allow future work on combining axial heterostructures defining tunnel barriers/quantum dots in semiconductor nanowires [80] with *in-situ* deposition of patterned superconductors for ultra-compact device architectures.

Engineering the superconducting properties of materials at the nanoscale, including the conditions for obtaining hard-gap proximity-induced superconductivity in hybrid devices, relies on understanding how different degrees of crystallinity can enable or prohibit superconductivity. Therefore, combining data from low temperature electron transport measurements and high-resolution electron microscopy was essential to this work in correlating the crystallinity of thin-film superconductors to their superconducting properties. The characterisation techniques provided basis for choosing parameters for nanowire growth and superconductor deposition parameters towards improved hybrids. Previous studies on Al/InAs hybrids attributed the successful proximity-induced hard gap superconductivity to the epitaxy between the crystals [35]. This work showed that epitaxy is not a prerequisite for proximity-induced hard gap superconductivity, as nanocrystalline tantalum on InAs in-

duced a gap with a hardness comparable to that observed in Al/InAs. Rather, an impurity-free, uniform interface may be sufficient if the thin film itself supports well-defined superconductivity. Naturally, the results from vanadium and niobium provide a caveat: For vanadium, no well-defined, macroscopic superconducting transition temperature was observed, which precluded the observation of an induced gap in V/InAs hybrids. Similarly, the oxidation of Nb films was likely responsible for the observed soft gap. Overall, the wide range of superconducting materials made possible by the shadow mask platform has provided these crucial insights into the behaviour of nanoscale superconductivity and hybrid device properties.

The presented work enables future advances in hybrid device architectures, new hybrid combinations of nanomaterials and *in-situ* protection of surfaces. Beyond the applications in devices handling quantum information, electrical contact quality, reproducibility and surface disorder play an pivotal role in nearly *all* nanoscale devices and thus the shadow platform holds the potential to strongly impact also conventional electronics, sensor-applications and optoelectronic devices [145, 146].

Bibliography

[1] W. Hu. ‘Transistors.’ In: *Transistors*, pp. 167–167. World Scientific (1998)

[2] A. Ostendorf & H. Hundertmark. ‘Laser.’ In: *Technology Guide*, pp. 104–109. Springer Berlin Heidelberg, Berlin, Heidelberg (2009)

[3] S. Suresh. ‘Semiconductor Nanomaterials, Methods and Applications: A Review.’ *Nanoscience and Nanotechnology* **3** (3), pp. 62–74 (2013)

[4] M. Rudan. *Physics of Semiconductor Devices*. Springer New York, New York, NY (2015)

[5] D. D. Coon & M. D. Fiske. ‘Josephson ac and step structure in the supercurrent tunneling characteristic.’ *Physical Review* **138** (3A) (1965)

[6] M. Tinkham. *Introduction to Superconductivity*. McGraw-Hill, New York, 2 edition (1996)

[7] S. Matsumoto, T. Kiyoshi, A. Otsuka, M. Hamada, H. Maeda, Y. Yanagisawa, H. Nakagome & H. Suematsu. ‘Generation of 24 T at 4.2 K using a layer-wound GdBCO insert coil with Nb 3 Sn and Nb–Ti external magnetic field coils.’ *Superconductor Science and Technology* **25** (2), p. 025017 (2012)

[8] K. M. Shen & J. S. Davis. ‘Cuprate high-Tc superconductors.’ *Materials Today* **11** (9), pp. 14–21 (2008)

[9] D. A. Neamen. ‘Semiconductor physics and devices.’ *Materials Today* **9** (5), p. 57 (2006)

[10] R. Holm & W. Meissner. ‘Einige Kontaktwiderstandsmessungen bei tiefen Temperaturen.’ *Zeitschrift für Physik* **86** (11-12), pp. 787–791 (1933)

[11] H. Meissner. ‘Superconductivity of Contacts with Interposed Barriers.’ *Physical Review* **117** (3), pp. 672–680 (1960)

[12] Y.-J. Doh. ‘Tunable Supercurrent Through Semiconductor Nanowires.’ *Science* **309** (5732), pp. 272–275 (2005)

[13] L. Fu & C. L. Kane. ‘Superconducting Proximity Effect and Majorana Fermions at the Surface of a Topological Insulator.’ *Physical Review Letters* **100** (9), p. 096407 (2008)

[14] A. Cook & M. Franz. ‘Majorana fermions in a topological-insulator nanowire proximity-coupled to an s-wave superconductor.’ *Physical Review B* **84** (20), p. 201105 (2011)

[15] L. Fu & C. L. Kane. ‘Josephson current and noise at a superconductor/quantum-spin-Hall-insulator/superconductor junction.’ *Physical Review B* **79** (16), p. 161408 (2009)

[16] A. Y. Kitaev. 'Unpaired Majorana fermions in quantum wires.' *Physics-Uspekhi* **44** (10S), pp. 131–136 (2001)

[17] R. M. Lutchyn, J. D. Sau & S. Das Sarma. 'Majorana Fermions and a Topological Phase Transition in Semiconductor-Superconductor Heterostructures.' *Physical Review Letters* **105** (7), p. 077001 (2010)

[18] Y. Oreg, G. Refael & F. von Oppen. 'Helical Liquids and Majorana Bound States in Quantum Wires.' *Physical Review Letters* **105** (17), p. 177002 (2010)

[19] J. D. Sau, R. M. Lutchyn, S. Tewari & S. Das Sarma. 'Generic New Platform for Topological Quantum Computation Using Semiconductor Heterostructures.' *Physical Review Letters* **104** (4), p. 040502 (2010)

[20] J. Alicea. 'Majorana fermions in a tunable semiconductor device.' *Physical Review B* **81** (12), p. 125318 (2010)

[21] V. Mourik, K. Zuo, S. M. Frolov, S. R. Plissard, E. P. A. M. Bakkers & L. P. Kouwenhoven. 'Signatures of Majorana Fermions in Hybrid Superconductor-Semiconductor Nanowire Devices.' *Science* **336** (6084), pp. 1003–1007 (2012)

[22] A. Das, Y. Ronen, Y. Most, Y. Oreg, M. Heiblum & H. Shtrikman. 'Zero-bias peaks and splitting in an Al–InAs nanowire topological superconductor as a signature of Majorana fermions.' *Nature Physics* **8** (12), pp. 887–895 (2012)

[23] C. Nayak, S. H. Simon, A. Stern, M. Freedman & S. Das Sarma. 'Non-Abelian anyons and topological quantum computation.' *Reviews of Modern Physics* **80** (3), pp. 1083–1159 (2008)

[24] F. Wilczek. 'Majorana returns.' *Nature Physics* **5** (9), pp. 614–618 (2009)

[25] B. van Heck, A. R. Akhmerov, F. Hassler, M. Burrello & C. W. J. Beenakker. 'Coulomb-assisted braiding of Majorana fermions in a Josephson junction array.' *New Journal of Physics* **14** (3), p. 035019 (2012)

[26] J. D. Sau, S. Tewari & S. Das Sarma. 'Universal quantum computation in a semiconductor quantum wire network.' *Physical Review A* **82** (5), p. 052322 (2010)

[27] J. Alicea, Y. Oreg, G. Refael, F. von Oppen & M. P. A. Fisher. 'Non-Abelian statistics and topological quantum information processing in 1D wire networks.' *Nature Physics* **7** (5), pp. 412–417 (2011)

[28] A. Kitaev. 'Fault-tolerant quantum computation by anyons.' *Annals of Physics* **303** (1), pp. 2–30 (2003)

[29] S. Das Sarma, M. Freedman & C. Nayak. 'Topologically Protected Qubits from a Possible Non-Abelian Fractional Quantum Hall State.' *Physical Review Letters* **94** (16), p. 166802 (2005)

[30] D. Aasen, M. Hell, R. V. Mishmash, A. Higginbotham, J. Danon, M. Leijnse, T. S. Jespersen, J. A. Folk, C. M. Marcus, K. Flensberg & J. Alicea. 'Milestones Toward Majorana-Based Quantum Computing.' *Physical Review X* **6** (3), p. 031016 (2016)

[31] T. D. Stanescu, R. M. Lutchyn & S. Das Sarma. 'Soft superconducting gap in semiconductor-based Majorana nanowires.' *Physical Review B* **90** (8), p. 085302 (2014)

[32] S. Takei, B. M. Fregoso, H.-Y. Hui, A. M. Lobos & S. Das Sarma. ‘Soft Superconducting Gap in Semiconductor Majorana Nanowires.’ *Physical Review Letters* **110** (18), p. 186803 (2013)

[33] Ö. Gül, H. Zhang, F. K. de Vries, J. van Veen, K. Zuo, V. Mourik, S. Conesa-Boj, M. P. Nowak, D. J. van Woerkom, M. Quintero-Pérez, M. C. Cassidy, A. Geresdi, S. Koelling, D. Car, S. R. Plissard, E. P. A. M. Bakkers & L. P. Kouwenhoven. ‘Hard Superconducting Gap in InSb Nanowires.’ *Nano Letters* **17** (4), pp. 2690–2696 (2017)

[34] D. B. Suyatin, C. Thelander, M. T. Björk, I. Maximov & L. Samuelson. ‘Sulfur passivation for ohmic contact formation to InAs nanowires.’ *Nanotechnology* **18** (10), p. 105307 (2007)

[35] P. Krogstrup, N. L. B. Ziino, W. Chang, S. M. Albrecht, M. H. Madsen, E. Johnson, J. Nygård, C. M. Marcus & T. S. Jespersen. ‘Epitaxy of semiconductor–superconductor nanowires.’ *Nature Materials* **14** (4), pp. 400–406 (2015)

[36] W. Chang, S. M. Albrecht, T. S. Jespersen, F. Kuemmeth, P. Krogstrup, J. Nygård & C. M. Marcus. ‘Hard gap in epitaxial semiconductor–superconductor nanowires.’ *Nature Nanotechnology* **10** (3), pp. 232–236 (2015)

[37] J.-H. Kang, A. Grivnin, E. Bor, J. Reiner, N. Avraham, Y. Ronen, Y. Cohen, P. Kacman, H. Shtrikman & H. Beidenkopf. ‘Robust Epitaxial Al Coating of Reclined InAs Nanowires.’ *Nano Letters* **17** (12), pp. 7520–7527 (2017)

[38] R. S. Wagner & W. C. Ellis. ‘VAPOR-LIQUID-SOLID MECHANISM OF SINGLE CRYSTAL GROWTH.’ *Applied Physics Letters* **4** (5), pp. 89–90 (1964)

[39] M. Kjaergaard, F. Nichele, H. J. Suominen, M. P. Nowak, M. Wimmer, A. R. Akhmerov, J. A. Folk, K. Flensberg, J. Shabani, C. J. Palmstrøm & C. M. Marcus. ‘Quantized conductance doubling and hard gap in a two-dimensional semiconductor–superconductor heterostructure.’ *Nature Communications* **7** (1), p. 12841 (2016)

[40] A. C. C. Drachmann, H. J. Suominen, M. Kjaergaard, B. Shojaei, C. J. Palmstrøm, C. M. Marcus & F. Nichele. ‘Proximity Effect Transfer from NbTi into a Semiconductor Heterostructure via Epitaxial Aluminum.’ *Nano Letters* **17** (2), pp. 1200–1203 (2017)

[41] F. Krizek, J. E. Sestoft, P. Aseev, S. Marti-Sanchez, S. Vaitiekenas, L. Casparis, S. A. Khan, Y. Liu, T. Stankevič, A. M. Whiticar, A. Fursina, F. Boekhout, R. Koops, E. Uccelli, L. P. Kouwenhoven, C. M. Marcus, J. Arbiol & P. Krogstrup. ‘Field Effect Enhancement in Buffered Quantum Nanowire Networks.’ *Physical Review Materials* **2** (9), p. 93401 (2018)

[42] S. Vaitiekenas, A. M. Whiticar, M.-T. Deng, F. Krizek, J. E. Sestoft, C. J. Palmstrøm, S. Marti-Sanchez, J. Arbiol, P. Krogstrup, L. Casparis & C. M. Marcus. ‘Selective-Area-Grown Semiconductor-Superconductor Hybrids: A Basis for Topological Networks.’ *Physical Review Letters* **121** (14), p. 147701 (2018)

[43] M. T. Deng, S. Vaitiekenas, E. B. Hansen, J. Danon, M. Leijnse, K. Flensberg, J. Nygård, P. Krogstrup & C. M. Marcus. ‘Majorana Bound State in a Coupled Quantum-Dot Hybrid-Nanowire System.’ *Science* **354** (6319), pp. 1557–1562 (2016)

[44] D. J. van Woerkom, A. Proutski, B. van Heck, D. Bouman, J. I. Väyrynen, L. I. Glazman, P. Krogstrup, J. Nygård, L. P. Kouwenhoven & A. Geresdi. 'Microwave spectroscopy of spinful Andreev bound states in ballistic semiconductor Josephson junctions.' *Nature Physics* **13** (9), pp. 876–881 (2017)

[45] D. Laroche, D. Bouman, D. J. van Woerkom, A. Proutski, C. Murthy, D. I. Pikulin, C. Nayak, R. J. J. van Gulik, J. Nygård, P. Krogstrup, L. P. Kouwenhoven & A. Geresdi. 'Observation of the 4π-periodic Josephson effect in indium arsenide nanowires.' *Nature Communications* **10** (1), p. 245 (2019)

[46] L. Tosi, C. Metzger, M. F. Goffman, C. Urbina, H. Pothier, S. Park, A. L. Yeyati, J. Nygård & P. Krogstrup. 'Spin-Orbit Splitting of Andreev States Revealed by Microwave Spectroscopy.' *Physical Review X* **9** (1), p. 011010 (2019)

[47] M. Hays, G. de Lange, K. Serniak, D. J. van Woerkom, D. Bouman, P. Krogstrup, J. Nygård, A. Geresdi & M. H. Devoret. 'Direct Microwave Measurement of Andreev-Bound-State Dynamics in a Semiconductor-Nanowire Josephson Junction.' *Physical Review Letters* **121** (4), p. 047001 (2018)

[48] T. W. Larsen, K. D. Petersson, F. Kuemmeth, T. S. Jespersen, P. Krogstrup, J. Nygård & C. M. Marcus. 'Semiconductor-Nanowire-Based Superconducting Qubit.' *Physical Review Letters* **115** (12), pp. 1–5 (2015)

[49] F. Luthi, T. Stavenga, O. W. Enzing, A. Bruno, C. Dickel, N. K. Langford, M. A. Rol, T. S. Jespersen, J. Nygård, P. Krogstrup & L. DiCarlo. 'Evolution of Nanowire Transmon Qubits and Their Coherence in a Magnetic Field.' *Physical Review Letters* **120** (10), p. 100502 (2018)

[50] S. M. Albrecht, A. P. Higginbotham, M. Madsen, F. Kuemmeth, T. S. Jespersen, J. Nygård, P. Krogstrup & C. M. Marcus. 'Exponential protection of zero modes in Majorana islands.' *Nature* **531** (7593), pp. 206–209 (2016)

[51] D. Sherman, J. S. Yodh, S. M. Albrecht, J. Nygård, P. Krogstrup & C. M. Marcus. 'Normal, superconducting and topological regimes of hybrid double quantum dots.' *Nature Nanotechnology* **12** (3), pp. 212–217 (2017)

[52] A. Proutski, D. Laroche, B. van 't Hooft, P. Krogstrup, J. Nygård, L. P. Kouwenhoven & A. Geresdi. 'Broadband microwave spectroscopy of semiconductor nanowire-based Cooper-pair transistors.' *Physical Review B* **99** (22), p. 220504 (2019)

[53] N. A. Güsken, T. Rieger, P. Zellekens, B. Bennemann, E. Neumann, M. I. Lepsa, T. Schäpers & D. Grützmacher. 'MBE growth of Al/InAs and Nb/InAs superconducting hybrid nanowire structures.' *Nanoscale* **9** (43), pp. 16735–16741 (2017)

[54] H. Zhang, Ö. Gül, S. Conesa-Boj, M. P. Nowak, M. Wimmer, K. Zuo, V. Mourik, F. K. de Vries, J. van Veen, M. W. A. de Moor, J. D. S. Bommer, D. J. van Woerkom, D. Car, S. R. Plissard, E. P. Bakkers, M. Quintero-Pérez, M. C. Cassidy, S. Koelling, S. Goswami, K. Watanabe, T. Taniguchi & L. P. Kouwenhoven. 'Ballistic superconductivity in semiconductor nanowires.' *Nature Communications* **8** (1), p. 16025 (2017)

[55] Ö. Gül, H. Zhang, J. D. S. Bommer, M. W. A. de Moor, D. Car, S. R. Plissard, E. P. A. M. Bakkers, A. Geresdi, K. Watanabe, T. Taniguchi & L. P. Kouwenhoven. 'Ballistic Majorana nanowire devices.' *Nature Nanotechnology* **13** (3), pp. 192–197 (2018)

[56] H. Zhang, C.-X. Liu, S. Gazibegovic, D. Xu, J. A. Logan, G. Wang, N. van Loo, J. D. S. Bommer, M. W. A. de Moor, D. Car, R. L. M. Op het Veld, P. J. van Veldhoven, S. Koelling, M. A. Verheijen, M. Pendharkar, D. J. Pennachio, B. Shojaei, J. S. Lee, C. J. Palmstrøm, E. P. A. M. Bakkers, S. D. Sarma & L. P. Kouwenhoven. 'Quantized Majorana conductance.' *Nature* **556** (7699), pp. 74–79 (2018)

[57] S. Nadj-Perge, V. S. Pribiag, J. W. G. van den Berg, K. Zuo, S. R. Plissard, E. P. A. M. Bakkers, S. M. Frolov & L. P. Kouwenhoven. 'Spectroscopy of Spin-Orbit Quantum Bits in Indium Antimonide Nanowires.' *Physical Review Letters* **108** (16), p. 166801 (2012)

[58] F. Krizek, T. Kanne, D. Razmadze, E. Johnson, J. Nygård, C. M. Marcus & P. Krogstrup. 'Growth of InAs Wurtzite Nanocrosses from Hexagonal and Cubic Basis.' *Nano Letters* **17** (10), pp. 6090–6096 (2017)

[59] S. Gazibegovic, D. Car, H. Zhang, S. C. Balk, J. A. Logan, M. W. A. de Moor, M. C. Cassidy, R. Schmits, D. Xu, G. Wang, P. Krogstrup, R. L. M. Op het Veld, K. Zuo, Y. Vos, J. Shen, D. Bouman, B. Shojaei, D. Pennachio, J. S. Lee, P. J. van Veldhoven, S. Koelling, M. A. Verheijen, L. P. Kouwenhoven, C. J. Palmstrøm & E. P. A. M. Bakkers. 'Epitaxy of advanced nanowire quantum devices.' *Nature* **548** (7668), pp. 434–438 (2017)

[60] D. B. Williams & C. B. Carter. *Transmission Electron Microscopy*. Springer US, Boston, MA (2009)

[61] J. W. Edington. *Electron Diffraction in the Electron Microscope*. Macmillan Education UK, London (1975)

[62] S. Nishikawa & S. Kikushi. 'Diffraction of Cathode Rays by Mica.' *Nature* **121** (3061), pp. 1019–1020 (1928)

[63] M. G. Norton & C. B. Carter. 'Moire patterns and their application to the study of the growth of YBa2Cu3O7 thin films.' *Journal of Materials Science* **30** (2), pp. 381–389 (1995)

[64] F. Pobell. 'The 3 He – 4 He Dilution Refrigerator.' *Matter and Methods at low Temperature* (2007)

[65] E. J. Lee, X. Jiang, M. Houzet, R. Aguado, C. M. Lieber & S. De Franceschi. 'Spin-resolved Andreev levels and parity crossings in hybrid superconductor-semiconductor nanostructures.' *Nature Nanotechnology* **9** (1), pp. 79–84 (2014)

[66] S. Plugge, A. Rasmussen, R. Egger & K. Flensberg. 'Majorana Box Qubits.' *New Journal of Physics* **19** (1), p. 12001 (2017)

[67] A. P. Higginbotham, S. M. Albrecht, G. Kiršanskas, W. Chang, F. Kuemmeth, P. Krogstrup, T. S. Jespersen, J. Nygård, K. Flensberg & C. M. Marcus. 'Parity Lifetime of Bound States in a Proximitized Semiconductor Nanowire.' *Nature Physics* **11** (12), pp. 1017–1021 (2015)

[68] J. Shen, S. Heedt, F. Borsoi, B. van Heck, S. Gazibegovic, R. L. M. Op het Veld, D. Car, J. A. Logan, M. Pendharkar, S. J. J. Ramakers, G. Wang, D. Xu, D. Bouman, A. Geresdi, C. J. Palmstrøm, E. P. A. M.

Bakkers & L. P. Kouwenhoven. 'Parity transitions in the superconducting ground state of hybrid InSb–Al Coulomb islands.' *Nature Communications* **9** (1), p. 4801 (2018)

[69] R. Rinaldi, P. V. Giugno, R. Cingolani, H. Lipsanen, M. Sopanen, J. Tulkki & J. Ahopelto. 'Zeeman Effect in Parabolic Quantum Dots.' *Physical Review Letters* **77** (2), pp. 342–345 (1996)

[70] C. Reeg, O. Dmytruk, D. Chevallier, D. Loss & J. Klinovaja. 'Zero-energy Andreev bound states from quantum dots in proximitized Rashba nanowires.' *Physical Review B* **98** (24), pp. 1–12 (2018)

[71] S. Vaitiekenas, M.-T. Deng, P. Krogstrup & C. M. Marcus. 'Flux-Induced Majorana Modes in Full-Shell Nanowires.' *arXiv preprint* (1809.05513) (2018)

[72] S. Vaitiekenas, M.-T. Deng, J. Nygård, P. Krogstrup & C. M. Marcus. 'Effective g Factor of Subgap States in Hybrid Nanowires.' *Physical Review Letters* **121** (3), p. 037703 (2018)

[73] M. Bjergfelt, D. J. Carrad, T. Kanne, M. Aagesen, E. M. Fiordaliso, E. Johnson, B. Shojaei, C. J. Palmstrøm, P. Krogstrup, T. S. Jespersen & J. Nygård. 'Superconducting vanadium/indium-arsenide hybrid nanowires.' *Nanotechnology* **30** (29), p. 294005 (2019)

[74] Y. Liu, S. Vaitiekenas, S. Marti-Sanchez, C. Koch, S. Hart, Z. Cui, T. Kanne, S. A. Khan, R. Tanta, S. Upadhyay, M. E. Cachaza, C. M. Marcus, J. Arbiol, K. A. Moler & P. Krogstrup. 'Semiconductor - Ferromagnetic Insulator - Superconductor Nanowires: Stray Field and Exchange Field.' *arXiv preprint* (1910.03364) (2019)

[75] Y. Liu, A. Luchini, S. Martí-Sánchez, C. Koch, S. Schuwalow, S. A. Khan, T. Stankevič, S. Francoua, J. R. L. Mardegan, J. A. Krieger, V. N. Strocov, J. Stahn, C. A. F. Vaz, M. Ramakrishnan, U. Staub, K. Lefmann, G. Aeppli, J. Arbiol & P. Krogstrup. 'Coherent Epitaxial Semiconductor-Ferromagnetic Insulator InAs/EuS Interfaces: Band Alignment and Magnetic Structure.' *arXiv preprint* (1908.07096) (2019)

[76] J. Mastomäki, S. Roddaro, M. Rocci, V. Zannier, D. Ercolani, L. Sorba, I. J. Maasilta, N. Ligato, A. Fornieri, E. Strambini & F. Giazotto. 'InAs nanowire superconducting tunnel junctions: Quasiparticle spectroscopy, thermometry, and nanorefrigeration.' *Nano Research* **10** (10), pp. 3468–3475 (2017)

[77] S. Vaitiekenas, P. Krogstrup & C. M. Marcus. 'Anomalous Metallic Phase in Tunable Destructive Superconductors.' *arXiv preprint* (1909.10654) (2019)

[78] P. Krogstrup, H. I. Jørgensen, E. Johnson, M. H. Madsen, C. B. Sørensen, A. F. i. Morral, M. Aagesen, J. Nygård & F. Glas. 'Advances in the theory of III-V nanowire growth dynamics.' *Journal of Physics D: Applied Physics* **46** (31), p. 313001 (2013)

[79] S. Roddaro, A. Pescaglini, D. Ercolani, L. Sorba & F. Beltram. 'Manipulation of electron orbitals in hard-wall InAs/InP nanowire quantum dots.' *Nano Letters* **11** (4), pp. 1695–1699 (2011)

[80] V. Zannier, F. Rossi, D. Ercolani & L. Sorba. 'Growth dynamics of InAs/InP nanowire heterostructures by Au-assisted chemical beam epitaxy.' *Nanotechnology* **30** (9), p. 094003 (2019)

[81] H. A. Nilsson, P. Caroff, C. Thelander, M. Larsson, J. B. Wagner, L.-E. Wernersson, L. Samuelson & H. Q. Xu. 'Giant, Level-Dependent g Factors in InSb Nanowire Quantum Dots.' *Nano Letters* **9** (9), pp. 3151–3156 (2009)

[82] T. Hoss, C. Strunk & C. Schönenberger. 'Nonorganic Evaporation Mask for Superconducting Nanodevices.' *Microelectronic Engineering* **46** (1), pp. 149–152 (1999)

[83] L. J. Lauhon, M. S. Gudiksen, D. Wang & C. M. Lieber. 'Epitaxial core–shell and core–multishell nanowire heterostructures.' *Nature* **420** (6911), pp. 57–61 (2002)

[84] C. Colombo, D. Spirkoska, M. Frimmer, G. Abstreiter & A. Fontcuberta i Morral. 'Ga-assisted catalyst-free growth mechanism of GaAs nanowires by molecular beam epitaxy.' *Physical Review B* **77** (15), p. 155326 (2008)

[85] E. Calleja, M. A. Sánchez-García, F. J. Sánchez, F. Calle, F. B. Naranjo, E. Muñoz, U. Jahn & K. Ploog. 'Luminescence properties and defects in GaN nanocolumns grown by molecular beam epitaxy.' *Physical Review B* **62** (24), pp. 16826–16834 (2000)

[86] J. L. Webb, J. Knutsson, M. Hjort, S. Gorji Ghalamestani, K. A. Dick, R. Timm & A. Mikkelsen. 'Electrical and Surface Properties of InAs/InSb Nanowires Cleaned by Atomic Hydrogen.' *Nano Letters* **15** (8), pp. 4865–4875 (2015)

[87] M. T. Deng, C. L. Yu, G. Y. Huang, M. Larsson, P. Caroff & H. Q. Xu. 'Anomalous Zero-Bias Conductance Peak in a Nb–InSb Nanowire–Nb Hybrid Device.' *Nano Letters* **12** (12), pp. 6414–6419 (2012)

[88] M. T. Deng, S. Vaitiekenas, E. B. Hansen, J. Danon, M. Leijnse, K. Flensberg, J. Nygård, P. Krogstrup & C. M. Marcus. 'Majorana bound state in a coupled quantum-dot hybrid-nanowire system.' *Science* **354** (6319), pp. 1557–1562 (2016)

[89] F. Nichele, A. C. C. Drachmann, A. M. Whiticar, E. C. T. O'Farrell, H. J. Suominen, A. Fornieri, T. Wang, G. C. Gardner, C. Thomas, A. T. Hatke, P. Krogstrup, M. J. Manfra, K. Flensberg & C. M. Marcus. 'Scaling of Majorana Zero-Bias Conductance Peaks.' *Physical Review Letters* **119** (13), p. 136803 (2017)

[90] D. J. Carrad, M. Bjergfelt, T. Kanne, M. Aagesen, F. Krizek, E. M. Fiordaliso, E. Johnson, J. Nygård & T. S. Jespersen. 'Shadow lithography for in-situ growth of generic semiconductor/superconductor devices.' *arXiv preprint* (1911.00460) (2019)

[91] E. B. Hansen, J. Danon & K. Flensberg. 'Probing electron-hole components of subgap states in Coulomb blockaded Majorana islands.' *Physical Review B* **97** (4), p. 041411 (2018)

[92] D. T. Lennon, H. Moon, L. C. Camenzind, L. Yu, D. M. Zumbühl, G. a. D. Briggs, M. A. Osborne, E. A. Laird & N. Ares. 'Efficiently measuring a quantum device using machine learning.' *npj Quantum Information* **5** (1), p. 79 (2019)

[93] C. S. Barret. *Structure of Metals: Crystallographic Methods, Principles, and Data*. McGraw-Hill Book Company, Jnc, 1st edition (1943)

[94] E. G. Moshopoulou, R. M. Ibberson, J. L. Sarrao, J. D. Thompson & Z. Fisk. 'Structure of Ce 2 RhIn 8 : an example of complementary use of high-resolution neutron powder diffraction and reciprocal-space mapping to study complex materials.' *Acta Crystallographica Section B Structural Science* **62** (2), pp. 173–189 (2006)

[95] K. Soulantica, L. Erades, M. Sauvan, F. Senocq, A. Maisonnat & B. Chaudret. 'Synthesis of indium and indium oxide nanoparticles from indium cyclopentadienyl precursor and their application for gas sensing.' *Advanced Functional Materials* **13** (7), pp. 553–557 (2003)

[96] K. Takemura & H. Fujihisa. 'High-pressure structural phase transition in indium.' *Physical Review B* **47** (14), pp. 8465–8470 (1993)

[97] A. A. Naberezhnov, A. E. Sovestnov & A. V. Fokin. 'Crystal structure of indium and lead under confined geometry conditions.' *Technical Physics* **56** (5), pp. 637–641 (2011)

[98] H. Potts, N. P. Morgan, G. Tütüncüoglu, M. Friedl & A. F. I. Morral. 'Tuning growth direction of catalyst-free InAs(Sb) nanowires with indium droplets.' *Nanotechnology* **28** (5), p. 054001 (2017)

[99] C. Ratsch & J. A. Venables. 'Nucleation theory and the early stages of thin film growth.' *Journal of Vacuum Science & Technology A: Vacuum, Surfaces, and Films* **21** (5), pp. S96–S109 (2003)

[100] Y. Zhu, A. Chen, H. Zhou, W. Zhang, J. Narayan, J. L. Macmanus-Driscoll, Q. Jia & H. Wang. 'Research updates: Epitaxial strain relaxation and associated interfacial reconstructions: The driving force for creating new structures with integrated functionality.' *APL Materials* **1** (5), pp. 0–11 (2013)

[101] L. Jelver, P. M. Larsen, D. Stradi, K. Stokbro & K. W. Jacobsen. 'Determination of low-strain interfaces via geometric matching.' *Physical Review B* **96** (8), p. 085306 (2017)

[102] C. V. Thompson. 'Grain growth in thin films.' *Annual Review of Materials Science* **20** (1), pp. 245–268 (1990)

[103] J. M. Hergenrother, M. T. Tuominen & M. Tinkham. 'Charge transport by Andreev reflection through a mesoscopic superconducting island.' *Physical Review Letters* **72** (11), pp. 1742–1745 (1994)

[104] C. Kittel. 'Introduction to Solid State Physics, 8th edition.' *Wiley & Sons, New York, NY* (2004)

[105] M. T. Tuominen, J. M. Hergenrother, T. S. Tighe & M. Tinkham. 'Experimental Evidence for Parity-Based 2e Periodicity in a Superconducting Single-Electron Tunneling Transistor.' *Physical Review Letters* **69** (13), pp. 1997–2000 (1992)

[106] F. Hassler & D. Schuricht. 'Strongly interacting Majorana modes in an array of Josephson junctions.' *New Journal of Physics* **14** (12), p. 125018 (2012)

[107] T. Mochiku, M. Tachiki, S. Ooi & Y. Matsushita. 'Synthesis of InSn alloy superconductor below room temperature.' *Physica C: Superconductivity and its Applications* **563**, pp. 33–35 (2019)

[108] C. G. Granqvist. 'Superconductivity of amorphous indium with silver impurities.' *Solid State Communications* **16** (5), pp. 581–584 (1975)

[109] W. M. Haynes, D. R. Lide & T. J. Bruno. *CRC Handbook of Chemistry and Physics : a ready-reference book of chemical and physical data.* (2016)

[110] W. S. Corak, B. B. Goodman, C. B. Satterthwaite & A. Wexler. 'Atomic Heats of Normal and Superconducting Vanadium.' *Physical Review* **102** (3), pp. 656–661 (1956)

[111] R. Radebaugh & P. H. Keesom. 'Low-Temperature Thermodynamic Properties of Vanadium. I. Superconducting and Normal States.' *Physical Review* **149** (1), pp. 209–216 (1966)

[112] P. Spathis, S. Biswas, S. Roddaro, L. Sorba, F. Giazotto & F. Beltram. 'Hybrid InAs nanowire–vanadium proximity SQUID.' *Nanotechnology* **22** (10), p. 105201 (2011)

[113] F. Giazotto, P. Spathis, S. Roddaro, S. Biswas, F. Taddei, M. Governale & L. Sorba. 'A Josephson quantum electron pump.' *Nature Physics* **7** (11), pp. 857–861 (2011)

[114] P. Wei, F. Katmis, C.-Z. Chang & J. S. Moodera. 'Induced Superconductivity and Engineered Josephson Tunneling Devices in Epitaxial (111)-Oriented Gold/Vanadium Heterostructures.' *Nano Letters* **16** (4), pp. 2714–2719 (2016)

[115] B. Loitsch, D. Rudolph, S. Morkötter, M. Döblinger, G. Grimaldi, L. Hanschke, S. Matich, E. Parzinger, U. Wurstbauer, G. Abstreiter, J. J. Finley & G. Koblmüller. 'Tunable Quantum Confinement in Ultrathin, Optically Active Semiconductor Nanowires Via Reverse-Reaction Growth.' *Advanced Materials* **27** (13), pp. 2195–2202 (2015)

[116] V. M. Kuz'menko, V. G. Lazarev, V. I. Mel'nikov & A. I. Sudovtsov. 'Superconductivity of amorphous vanadium.' *Zh. Eksp. Teor. Fiz* **67** (2), pp. 801–807 (1974)

[117] R. B. Lewis, P. Corfdir, H. Küpers, T. Flissikowski, O. Brandt & L. Geelhaar. 'Nanowires Bending over Backward from Strain Partitioning in Asymmetric Core-Shell Heterostructures.' *Nano Letters* **18** (4), pp. 2343–2350 (2018)

[118] O. Madelung, U. Rössler & M. Schulz. 'Indium arsenide (InAs), lattice parameter, thermal expansion.' In: *Group IV Elements, IV-IV and III-V Compounds.*, pp. 1–4. Springer Berlin Heidelberg, Berlin, Heidelberg (2002)

[119] V. G. Dubrovskii. *Nucleation Theory and Growth of Nanostructures*. NanoScience and Technology. Springer Berlin Heidelberg, Berlin, Heidelberg (2014)

[120] L. Lugani, D. Ercolani, F. Rossi, G. Salviati, F. Beltram & L. Sorba. 'Faceting of InAs-InSb heterostructured nanowires.' *Crystal Growth and Design* **10** (9), pp. 4038–4042 (2010)

[121] H. L. Luo, E. Vielhaber & E. Corenzwit. 'Occurrence of A-15 Phases.' *Zeitschrift für Physik* **230** (5), pp. 443–448 (1970)

[122] J. F. Smith & K. J. Lee. 'The In-V (Indium-Vanadium) system.' *Bulletin of Alloy Phase Diagrams* **6** (1), pp. 66–68 (1985)

[123] S. Bose & P. Ayyub. 'A review of finite size effects in quasi-zero dimensional superconductors.' *Reports on Progress in Physics* **77** (11), p. 116503 (2014)

[124] S. Sarkar, N. Kulkarni, R. Kulkarni, K. Thekkepat, U. Waghmare & P. Ayyub. 'Is There a Lower Size Limit for Superconductivity?' *Nano Letters* **17** (11), pp. 7027–7032 (2017)

[125] P. W. Anderson. 'Theory of dirty superconductors.' *Journal of Physics and Chemistry of Solids* **11** (1-2), pp. 26–30 (1959)

[126] S. Sekula & R. Kernohan. 'Magnetic properties of superconducting vanadium.' *Physical Review B* **5** (3), pp. 904–911 (1972)

[127] K. Grove-Rasmussen, G. Steffensen, A. Jellinggaard, M. H. Madsen, R. Žitko, J. Paaske & J. Nygård. 'Yu-Shiba-Rusinov screening of spins in double quantum dots.' *Nature Communications* **9** (1), p. 2376 (2018)

[128] H. O. Churchill, V. Fatemi, K. Grove-Rasmussen, M. T. Deng, P. Caroff, H. Q. Xu & C. M. Marcus. 'Superconductor-nanowire devices from tunneling to the multichannel regime: Zero-bias oscillations and magnetoconductance crossover.' *Physical Review B* **87** (24), pp. 1–6 (2013)

[129] J. J. Hauser & H. C. Theurer. 'Superconducting Tantalum Films.' *Reviews of Modern Physics* **36** (1), pp. 80–83 (1964)

[130] M. Zhang, Y. Zhang, P. Rack, M. Miller & T. Nieh. 'Nanocrystalline tetragonal tantalum thin films.' *Scripta Materialia* **57** (11), pp. 1032–1035 (2007)

[131] P. N. Denbigh & R. B. Marcus. 'Structure of Very Thin Tantalum and Molybdenum Films.' *Journal of Applied Physics* **37** (12), pp. 4325–4330 (1966)

[132] M. T. Janish, P. G. Kotula, B. L. Boyce & C. B. Carter. 'Observations of fcc and hcp tantalum.' *Journal of Materials Science* **50** (10), pp. 3706–3715 (2015)

[133] R. B. Marcus & S. Quigley. 'Formation of f.c.c., b.c.c. and β-tantalum films by evaporation.' *Thin Solid Films* **2** (5-6), pp. 467–477 (1968)

[134] Y. Seo, Y. Qin, C. L. Vicente, K. S. Choi & J. Yoon. 'Origin of Nonlinear Transport across the Magnetically Induced Superconductor-Metal-Insulator Transition in Two Dimensions.' *Physical Review Letters* **97** (5), p. 057005 (2006)

[135] K. Gharavi, G. W. Holloway, R. R. LaPierre & J. Baugh. 'Nb/InAs nanowire proximity junctions from Josephson to quantum dot regimes.' *Nanotechnology* **28** (8), p. 085202 (2017)

[136] T. Akazaki, J. Nitta & H. Takayanagi. 'Single-crystal growth of Nb films onto molecular beam epitaxy grown (001)InAs.' *Applied Physics Letters* **59** (16), pp. 2037–2039 (1991)

[137] S. Chuang, Q. Gao, R. Kapadia, A. C. Ford, J. Guo & A. Javey. 'Ballistic InAs Nanowire Transistors.' *Nano Letters* **13** (2), pp. 555–558 (2013)

[138] S. Heedt, N. Traverso Ziani, F. Crépin, W. Prost, S. Trellenkamp, J. Schubert, D. Grützmacher, B. Trauzettel & T. Schäpers. 'Signatures of interaction-induced helical gaps in nanowire quantum point contacts.' *Nature Physics* **13** (6), pp. 563–567 (2017)

[139] S. Heedt, W. Prost, J. Schubert, D. Grützmacher & T. Schäpers. 'Ballistic Transport and Exchange Interaction in InAs Nanowire Quantum Point Contacts.' *Nano Letters* **16** (5), pp. 3116–3123 (2016)

[140] T. Proslier, J. F. Zasadzinski, L. Cooley, C. Antoine, J. Moore, J. Norem, M. Pellin & K. E. Gray. 'Tunneling study of cavity grade Nb: Possible magnetic scattering at the surface.' *Applied Physics Letters* **92** (21), p. 212505 (2008)

[141] J. Halbritter. 'On the Oxidation and on the Superconductivity of Niobium.' *Applied Physics A* **43** (1), pp. 1–28 (1987)

[142] S. Shafranjuk, I. Nevirkovets & J. Ketterson. 'A qubit device based on manipulations of Andreev bound states in double-barrier Josephson junctions.' *Solid State Communications* **121** (9-10), pp. 457–460 (2002)

[143] G. Wendin. 'Scalable solid–state qubits: challenging decoherence and read–out.' *Philosophical Transactions of the Royal Society of London. Series A: Mathematical, Physical and Engineering Sciences* **361** (1808), pp. 1323–1338 (2003)

[144] S. Park & A. L. Yeyati. 'Andreev spin qubits in multichannel Rashba nanowires.' *Physical Review B* **96** (12), p. 125416 (2017)

[145] J. A. del Alamo. 'Nanometre-scale electronics with III–V compound semiconductors.' *Nature* **479** (7373), pp. 317–323 (2011)

[146] H. Riel, L.-E. Wernersson, M. Hong & J. A. del Alamo. 'III–V compound semiconductor transistors—from planar to nanowire structures.' *MRS Bulletin* **39** (8), pp. 668–677 (2014)

Chapter 5

Appendix

5.1 Shadow mask fabrication recipe

1. **Starting points:**

   (a) Epi-ready InAs (111)B 2" wafer - henceforth refered to as "the substrate"

   (b) GDSII file (or other compatible database file) featuring a layer with desired shadow mask pattern and a layer with the positions for the growth catalysts - henceforth referred to as "the pattern file". The shadow mask patten should feature align marks (4 circles of $\varnothing = 2\mu$m suffices.)

2. 150 nm of SiO_x is deposited on the substrate using a plasma enhanced chemical vapour deposition (PECVD) furnace.

3. **Photolithography defining the shadow mask patterns:**

   (a) Spin-coating photoresist:

      i. Load wafer onto spin coater, turn on the vacuum and blow N_2 to make sure the surface is free of dust particles.

      ii. Deposit ~7.5 mL of AZ1505 photoresist (MicroChemicals^{TM}) onto the substrate using a 7.5 mL pipette. The resist needs to fill the substrate to close to edges (without overflow) to ensure a uniform coating.

      iii. Spin at 4000 RPM for 45 seconds.

      iv. Bake on 115°C hotplate for 1 minute.

   (b) Exposure on μPG501 LED writer:

      i. Align the major flat of the substrate parallel to the x-axis of the writers coordinate system. In our system that means that the flat is to the left when loading.

      ii. Use the manual alignment mode to locate two position on the major flat to correct for any rotational off set that occurred during loading. The two postions are also used to correlate positions in the pattern file to positions in the coordiate system of the writer/substrate.

      iii. Expose the substrate. Note: Perform a dose test of the pattern to determine appropriate exposure dose time and defocus setting of the laser.

(c) Develop the resist in MF-321 (Microposit^{TM}) for 45 seconds, rinse in Milli-Q purified water (henceforth referred to as "MQ").

(d) Plasma-ash the exposed resist to clear any remaining resist residue in the exposed substrate regions.

4. **Chemical etching of SiO_x and trenches in InAs:**

   (a) Bake the substate on a 145°C hotplate to harden the photoresist, making it adhere more efficiently to the oxide.

   (b) Etch the SiO_x using buffered hydrofloric acid (BHF) (6% HF in an aqueous solution of ammonium fluoride). 150 nm SiO_x takes $\sim$40 seconds to etch through. Rinse 3 times in (individual) beakers with MQ.

   (c) Etch the InAs using a fresh solution of:

      i. 15g solid citric acid fully dissolved in 40 mL MQ using magnetic stirring.

      ii. Add 20 mL phosphoric acid (80%) and 12 mL H_2O_2 while the magnet is stirring.

   (d) 5 minutes etches about 7 μm.

   (e) Rinse in MQ.

   (f) Remove the photoresist using N-Methyl-2-pyrrolidone (NMP).

   (g) Rinse in acetone, isopropanol (IPA) and MQ

5. **Optional:** Atomic layer deposition of 15 nm AlO_x. 150 cycles of at 180°C

6. **Electron beam lithography for deterministically positioned Au growth catalyst:**

   (a) Spin-coating electron beam resists:

      i. Load wafer onto spin coater, turn on the vacuum and blow N_2 to make sure the surface is free of dust particles.

      ii. Deposit $\sim$7.5 mL of PMMA A4 (MicroChem^{TM}) electron beam resist onto the substrate using a 7.5 mL pipette. The resist needs to fill the substrate to close to edges (without overflow) to ensure a uniform coating.

      iii. Let the resist settle on the substrate for 2 minutes

      iv. Spin at using the following spinning program gradually increasing the spin speed. All steps use an acceleration of 100 RPM/s:

         A. 250 RPM for 20 seconds.

         B. 500 RPM for 20 seconds.

         C. 1500 RPM for 20 seconds.

         D. 3000 RPM for 45 seconds.

         E. Decelerate to 0 RPM in 10 seconds.

   (b) Bake on a 185°C hotplate for 1 minute.

   (c) Repeat 6a using the copolymer MMA EL-13 (MicroChem^{TM}).

   (d) Bake on a 185°C hotplate for 2 minutes.

(e) Electron beam exposure with Elionix 100 kV system:
   i. Load substrate
   ii. Condition beam for beam current $I = 1$ nA using a 40 μm aperture, focus beam and correct for astigmatism.
   iii. Load layer for Au growth catalyst positions in the pattern file.
   iv. Align the pattern to the 4 alignment marks etched into the substrate in the shadow mask pattern.
   v. Expose the pattern.

(f) Develop the electron beam resists for 2 mins using a solution of Methyl isobutyl ketone (MIBK) and IPA. Volume ratio MIBK:IPA = 1:3. Rinse in MQ.

(g) Plasma ash for 1 minute the substrate to remove any residual resist.

(h) **If AlO_x was deposited:**
   i. Etch the AlO_x for 2 minutes in 50°C Al etchant type D (Transene^{TM})
   ii. Rinse in MQ.

(i) Etch the exposed InAs surface using BHF for 10 seconds. Rinse with MQ 3 times.

(j) Hurry to the metal evaporator (AJA) and load the substrate.

(k) Evaporate the desired Au thickness (10 nm - 20 nm in this study) at at rate of $\sim$ 1 Å/s (e-beam current $\sim$ 34 mA).

(l) Lift off the Au deposited on the e-beam resists using acetone ($\sim$ 1 hour).

(m) Rinse in fresh acetone, IPA and MQ.

7. Substrate is ready for hybrid nanowire growth.

5.2 Supplementary structural data: Indium

In Sec. 3.3.2, comparing the acquired data to reported structural data for bulk indium required a variaty of plane angles and interplanar distances of the bulk crystal had to be tabulated. Bulk indium was reported to crystallise in the tetragonal body-centred (TBC) phase (space group $I4/mmm$) with lattice parameters $a = 0.3253$ nm and $c = 0.4947$ nm [94] and so angles and distances in this tetragonal crystal were calculated. Angles ϕ between low-index planes in the tetragonal crystal system $(h_1k_1l_1)$ and $(h_2k_2l_2)$ were tabulated using Eq. 5.1 [61] in Table 5.1. Additionally, the interplanar distances in the tetragonal crystal system, $d_{(hkl)}$, were tabulated using Eq. 5.2 [61] in Table 5.2. Low-index bicrystal mismathes between In and InAs is tabulated in Table 5.3.

$$\cos\phi = \frac{\frac{1}{a^2}(h_1h_2 + k_1k_2) + \frac{1}{c^2}l_1l_2}{\sqrt{\left\{\left[\frac{1}{a^2}(h_1^2 + k_1^2) + \frac{1}{c^2}l_1^2\right\}\left\{\frac{1}{a^2}(h_2^2 + k_2^2) + \frac{1}{c^2}l_2^2\right\}\right]}} \tag{5.1}$$

$$\frac{1}{d_{(hkl)}^2} = \frac{1}{a^2}(h^2 + k^2) + \frac{1}{c^2}l^2 \tag{5.2}$$

TBC plane angles ϕ (°)	{100}	{001}	{101}	{110}	{111}	{112}
{100}/{010}	90.0	90.0	33.3	45.0	50.1	58.8
{001}	90.0	90.0	56.7	90.0	65.1	47.1
{101}/{011}	33.3	56.7	**72.4**	**53.8**	39.9	36.2
{110}	45.0	90.0	**53.8**	90	24.9	42.9/**90**
{111}	50.1	65.1	39.9	24.9	79.8/49.9	18.0
{112}	58.8	47.1	36.2	42.9	18.0	85.8

Table 5.1: **Angles between families of planes in the tetragonal body-centred indium phase**. Calculated using Eq. 5.1 and the lattice parameters found in literature for bulk indium [94]. When calculating angle between planes from the same family different planes within the family were used.

TBC Planes	$d_{\{100\}}$ (Å)	$d_{\{001\}}$ (Å)	$d_{\{101\}}$ (Å)	$d_{\{110\}}$ (Å)	$d_{\{111\}}$ (Å)	$d_{\{112\}}$ (Å)
	3.253	4.947	2.718	2.300	2.085	1.684

Table 5.2: **Interplanar distances the tetragonal body-centred indium phase.** Calculated using Eq. 5.2 and the lattice parameters found in literature for bulk indium [94].

Planes	Axial mm. to InAs (0002) (#In:#InAs)	Transverse mm. to InAs ($2\bar{1}\bar{1}0$) (#In:#InAs)
(100)/(010)	7% (1:1)	-1.2% (2:3)
(001)	5.7% (2:3), 1% (5:7)	7.6% (2:5), 1% (3:7)
(111)	2.7% (1:1)	**2.6% (1:1)**
(110)	1.4% (3:2)	-7.4% (1:1)
(101)/(011)	-3.6% (4:3), 2.9% (5:4)	4.8% (3:4), -1.5% (4:5)
(112)	**3.7% (2:1)**	-4.9% (4:3), -1.7% (5:4)
(211)	0.25% (5:2)	2.3% (3:2)

Table 5.3: **Bi-crystal mismatch (mm.) between indium planes and InAs axial and transverse planes**. The values in the table were based on 14 calculated domain mismatch tables spanning a wide range of domain size. Here, only the smallest mismatches of few plane (#In:#InAs) domains are shown.